GEOFORSCHUNGSZENTRUM POTSDAM

STIFTUNG DES ÖFFENTLICHEN RECHTS

Scientific Technical Report

Modelling and Interpretation of Global Lithospheric Magnetic Anomalies

————————

Dissertation
zur Erlangung des Doktorgrades
im Fachbereich Geowissenschaften
an der Freien Universität Berlin

Kumar Hemant

Berlin, 2003

Contents

iii

Abstract

After a gap of nearly two decades since the Magsat mission in 1980, the dedicated low-orbit potential field mission CHAMP is now in the third of its seven year mission. Already, the new magnetic total intensity and vector data have yielded maps of the global crustal field of unprecedented accuracy and resolution. Here, we assess the value of these maps to infer deep crustal structure of regions overlain by younger cover. A GIS based modelling technique has been developed to model the various geological units of the continents starting from the geological map of the world. Depending upon the known rock types of the region, they are assigned a standard susceptibility value and using the global seismic crustal structure, a vertically integrated susceptibility (VIS) model is computed at each point of the region. Starting with this initial VIS model, the vertical field anomaly is computed at a satellite altitude of 400 km and compared with the corresponding CHAMP vertical field anomaly map. The first comparison is carried out against a model using the lateral extent of a cratonic region as given by published tectonic maps. In the subsequent modelling step, depending upon the extent of the observed anomaly pattern of that region, the surface geology is extended beneath the sediments until the recomputed map fits the observed magnetic anomaly map. Here, we focus on modelling results for the selected few provinces of the world where the initial model does not agree with the observed anomaly map. Similar modelling of CHAMP satellite magnetic anomalies can constrain the subsurface structure hidden by Phanerozoic cover in many parts of the world.

List of figures

List of Tables

List of Abbreviations and Symbols

VIS	Vertically Integrated Susceptibility
3SMAC	Global seismic model by Nataf and Ricard (1996)
CRUST5.1	Global seismic model by Mooney et al. (1998) (Resolution: 5^0 X 5^0)
CRUST2.1	Improved version of global seismic model CRUST5.1 (Resolution: 2^0 X 2^0)
CTD	Depth of the Curie-temperature isotherm
VRM	Viscous Remanent Magnetisation
GFZ	GeoForschungsZentrum

F	magnitude of the geomagnetic main field of the Earth (nT)
V_c	magnetic potential outside the Earth's core (v)
c	'core' of the Earth
I	inclination of the geomagnetic field (deg.)
D	declination of the geomagnetic field (deg.)
M	magnetisation or (dipole moment per unit volume, A/m)
$d\tau'$	elemental volume over the Earth's surface (km^3)
dm'	magnetisation of the elemental volume $d\tau'$ ($A\text{-}m^2$)
$r'(r',\theta',\phi')$	source coordinates of the elemental volume $d\tau'$ (m)
$r(r,\theta,\phi)$	distance from the center of the Earth to the point of observation (m)
$dV(r,r')$	magnetic potential at point r (v)
$\chi(r')$	susceptibility at point r' (dimensionless in SI units)
$\widetilde{\chi}(\theta',\phi')$	vertically integrated susceptibility (m)
$\widetilde{M}(\theta',\phi')$	vertically integrated magnetisation (A)
d	thickness of the crust (m)
ds'	elemental surface area at the source (m^2)
r'	radial distance of the source from the Earth's center (m)
θ'	colatitude at the source (deg.)
ϕ'	longitude at the source (deg.)
r	radial position coordinate at the point of observation (m)
θ	colatitude at the point of observation (deg.)
ϕ	longitude at the point of observation (deg.)
R	$\left|r-r'\right|$ (m)
s_0	area of cell size at the equator (m^2)
μ_0	magnetic permeability of free space [$4\pi \cdot 10^{-7}$ Henry/m]

p_n^m, q_n^m	spherical harmonic coefficients of the VIS
g_n^m, h_n^m	Gauss coefficients of the Geomagnetic main field
G_N^M, H_N^M	Gauss coefficients of the crustal field
n	spherical harmonic degree of the main field
m	spherical harmonic order of the main field
N	degree of spherical harmonic expansion for the crustal field
M	order of spherical harmonic expansion for the crustal field
δ_{MN}	Kronecker delta
P_n^m	Legendre's associated functions
$V(r, \theta, \phi)$	magnetic potential at the point of observation (v)
B_r	component of the crustal magnetic field in radial direction (nT)
B_θ	component of the crustal magnetic field in colatitude direction (nT)
B_ϕ	component of the crustal magnetic field in longitude direction (nT)
B_z	vertical component of the crustal magnetic field (nT), positive downward

Chapter 1

Introduction

Looking into the Earth's interior has always been a challenge because the deepest boreholes penetrate not more than 10 km and that depth has been reached in only few locations e.g. in Germany (Baum et al., 1995; Emmermann and Lauterjung, 1997). All sorts of measuring techniques and methods have been employed to reveal the mystery of deep inside. Geology, structural properties of rocks, surface geophysics, borehole geophysics, petrophysics, laboratory experiments, geochemistry, geochronology, fluid analysis, heat flow measurements have regularly been employed in all possible geometry to infer the rock types at various depths. Deep seismic sounding, gravity interpretation, geophysical well-logging, electrical methods and magnetic methods have contributed to the geophysical interpretation of the rock types lying at shallow and great depths. Not only these geophysical methods have benefited immensely to the exploration geophysicists to locate minerals and oil and gas reserves in the Earth but have also contributed to the understanding of the geophysical, geochemical and geological processes deep inside the Earth.

One of the geophysical methods, which have been regularly used for both exploration and understanding of deep interior of the Earth, is the magnetic method. Magnetic methods have been known now for more than 400 years since William Gilbert published *De Magnete* in 1600. Magnetic methods gained popularity and importance once it was established through the study of geomagnetism that Earth is a great magnet. Geomagnetism deals with the study of Earth's magnetic field. Earth's magnetic field not only changes with the latitude but also with time. To find the sources for these variations in the magnetic field recorded at the Earth's surface, more detailed studies were conducted. It is now known that the magnetic field at any location near the Earth can be attributed to a combination of four sources located respectively in the Earth's core, in the mantle, in the Earth's crust and in the Earth's ionosphere and beyond.

The largest in magnitude is the field from the core, or the 'main field'. Near dipolar in nature, the strength of the main field is approximately 60000 nT (nanotesla) at the poles and approximately 30000 nT at the equator. The variation of the main field with time is called its 'secular variation'. External current systems are time-varying on a scale of seconds to decades, which can cause near-Earth fields to vary in magnitude from fractions of a nT to thousands of nT. The external current systems are located in and on the boundary of a cavity-like region surrounding the Earth, known as the magnetosphere,

and in the Earth's ionosphere. The magnetosphere is a region which protects the earth from bombardment of charged particles from the Sun. Although always present, the strength and location of these currents varies considerably between magnetically quiet and disturbed times. Because they vary with time, the external fields cause induced currents in the Earth resulting in an 'induced field'. The ionosphere is a region above the Earth's surface, where the atmosphere is ionized due to the Sun's ultraviolet radiation. The resulting high conductivity in the ionosphere causes electric currents. These currents cause field variations in the ionosphere, which vary not only with respect to sun lit regions but also with latitude. Fields from the Earth's crust again range from fractions of a nT to thousands of nT. In general, the crustal source dimensions are small compared to the external field sources. Also called 'anomaly fields', crustal sources are associated with variations in the geologic and or geophysical properties of the Earth's crust. A portion of this field is from induced magnetisation and will follow variations of the main field. Another portion is remanent magnetisation, i.e., it is frozen in the rocks and varies on a geologic time scale. The contribution of magnetisation in the uppermost mantle to the geomagnetic field is still debated but is generally considered to be minor because of the high temperature of the rocks of the mantle. The temperature within the Earth increases with depth, and at a certain depth it is above the Curie temperature of the dominant magnetic minerals, where they lose their ferromagnetic properties. Curie temperature for magnetite is 578^0 C, and this isotherm marks the boundary below which magnetisation from the rocks of the upper mantle does not contribute significantly to the anomaly fields measured at the Earth's surface.

1.1 Some pertinent definitions

The magnetic field defined above as the 'main field' is the Earth's magnetic field, which starts from the liquid outer core of the Earth. It has a direction that is usually neither horizontal nor-in-line with the geographic meridian. The magnitude of this field 'F', the inclination (or dip) of the needle from the horizontal, I, and the angle it makes with geographic north (the declination), D, completely define the main magnetic field.

Any magnetizable body placed in an external field (here it is the main field of the earth) becomes magnetized by induction. Magnetisation is due to the reorientation of atoms and uncoupled electron spins. Magnetisation is measured by the magnetic polarization **M**, also called magnetic dipole moment per unit volume. The degree to which a body acquires induced magnetisation is determined by its magnetic susceptibility, k. Susceptibility is a fundamental rock parameter in magnetic exploration. The magnetic response of rocks and minerals is determined by the susceptibility of magnetic materials (mainly magnetite and pyrrhotite) contained in the rocks. They generally persist both over small and large distances; thus magnetic maps generally exhibit both small-scale and large-scale regional features. These features are called the 'crustal field' or the 'anomaly field' as defined earlier. The vertical component of this field is the vertical field anomaly and is positive downward. The total field anomaly or the scalar anomaly is the component of this field in the direction of the main field.

The magnetic field measured at any point near the surface of the earth is the sum of the main field, the field due to crustal magnetisation and the external field. The field from the core and the crust comprises the internal part of the total field. Our effort here is to study only the crustal component of this internal magnetic field. The sources for these crustal anomalies as defined above are primarily due to strong magnetisation exhibited by some specific minerals, which are discussed next.

Magnetism in rocks can be divided on the basis of their behaviour when placed in an external field (Telford, 1990; Blakely, 1996). *Diamagnetism* is an inherent property of all matter. In diamagnetism, an applied magnetic field disturbs the orbital motion of electrons in such a way as to induce a small magnetisation in the opposite sense to the applied field. Consequently, diamagnetic susceptibility is negative. *Paramagnetism* is a property of those solids that have atomic magnetic moments. Application of a magnetic field causes the atomic moments to partially align parallel to the applied field thereby producing a net magnetisation in the direction of the applied field. The susceptibility is positive. Both diamagnetic and paramagnetic materials are insignificant contributors to the geomagnetic field.

Certain materials have atomic moments where neighbouring moments interact strongly with each other. This interaction is a result of quantum mechanical effect called exchange energy. Certain paramagnetic elements, namely iron, cobalt and nickel, have such strong magnetic interaction that the moments align within fairly large regions called domains. This effect is called *ferromagnetism*, and it is ~ 10^6 times the effects of diamagnetism and paramagnetism. Ferromagnetism decreases with increasing temperature and disappear completely at the Curie temperature. The domains in some materials are subdivided into subdomains that align in opposite directions, so that their moments nearly cancel. Such substances are called *antiferromagnetic*. The common example is hematite. In some materials, the magnetic subdomains align in opposition but their net moment is not zero, either because one set of subdomains has a stronger magnetic alignment than the other or because there are more subdomains of one type than of the other. These substances are *ferrimagnetic*. Examples of the first type are magnetite and titanomagnetite, oxides of iron and titanium. Pyrrhotite is a magnetic mineral of the second type. Practically, all relevant magnetic minerals in the Earth's crust are ferrimagnetic.

1.2 Need for the present study

The crust primarily consists of igneous, sedimentary and metamorphic rocks. Sedimentary rocks generally have low magnetisations because of the lack of magnetite whereas the underlying crystalline basement of igneous and metamorphic rocks can be highly magnetic. Exceptions to the sedimentary rocks are the banded iron formations (BIF), which can be highly magnetic due to large amounts of magnetite they contain. The magnetic method has provided a primary tool for mapping the structure of the crystalline rocks of the continental crust. These mapping abilities can be crucial where rocks have limited exposure or no exposure at the surface because they are generally covered by sediments or water. Anomaly maps derived from magnetic data taken with airborne and

3

shipborne instruments are routinely used in the preparation of geologic and geophysical models of the crust. These surveys concentrate on geologic features less than about 50 km in lateral dimension. However, in past decades there has been increasing interest in studying large-scale anomalies, hundreds of kilometers in extent, that appear in regional compilations of data from airborne surveys. These large-scale anomalies are referred to as the long-wavelength anomalies. Spatial variations in these anomalies reflect variations in crust and upper-mantle magnetisation. Crustal magnetic field variations are caused not only by variation in the amount of magnetic minerals but also reflect variations in the crustal thickness, the depth to Curie isotherm, and geochemical nature of the rock source. Shive et al. (1992) claimed that long wavelength anomalies are generally caused by sources that lie deep in the crust and that lower crustal rocks are much more magnetic than the rocks exposed at the surface. Studies of such long wavelength anomalies or 'regional anomalies' have spurred renewed laboratory investigations of rock magnetisation especially for rocks present in the crust (Rochette, 1992).

Mapping global crustal magnetic fields started when the first series of satellites mapping only the scalar field anomaly revealed one of the strongest anomaly at the satellite altitude, the 'Bangui anomaly', centered at Bangui, capital of Central African Republic (Regan et al., 1975). This anomaly is located 6^0 N of the equator. Later satellite missions mapped both scalar and vector components of the magnetic anomalies to locate the sources more accurately. These satellite anomaly maps provide a distinct advantage over the conventional aeromagnetic surveys. Mapping global scale anomalies can be easily accomplished without respect for any political boundary. They are of uniform precision and spatial distribution. The data can be acquired within a short span of time without actually getting interfered by time varying Earth's main field. This possibility also helps in studying the regional anomalies without having to knit together data from surveys taken at different times and reduced under differing models of the core field (Hinze and Zietz, 1985). One of the principal contributions could be to extract a geographical subset from the global distribution of data for further detailed analysis. Here, we define long wavelength anomalies as those which are resolvable by satellite measurements (half-wavelength > 200 km). Having pointed out the advantages that these satellite data have over data acquired by conventional magnetic methods, let us look at the developments in the mapping of crustal field anomalies using satellite data and their impact over the last three decades.

1.3 Lithospheric field models

The POGO (1965-1971) satellite missions, Magsat (1979-1980) and, more recently, Ørsted (February 1999 onward), CHAMP (July 2000 onward) and SAC-C (November 2001 onward) in near-Earth orbits have helped us to understand not only the Earth's internal field but also the external fields with sources in the ionosphere and the magnetosphere. Based on the available satellite data from the last three decades, several lithospheric field anomaly maps have been computed by various workers. The POGO missions resulted in the first consistent map of crustal magnetic fields on a global (Regan et al., 1975) and regional scale (Langel and Thorning, 1982). These maps were primarily

scalar magnetic anomaly maps. The satellites orbited within an altitude range of 400 to 1510 km and, hence, due to poor lateral resolution and limited accuracies of their magnetometers were not suited to map crustal fields accurately. Magsat orbited at altitudes of 550 km down to 300 km from October 1979 to June 1980. Maps produced from Magsat data resolve magnetic features with wavelengths down to about 500 km (Langel et al., 1982a; Yanagisawa and Kono, 1985; Cain et al., 1989a; Cohen and Achache, 1990; Arkani-Hamed et al., 1994; Ravat et al., 1995; Sabaka et al., 2000). However, inaccuracies of the star cameras affected the quality of the vector data. The launch of the Ørsted satellite in February 1999, after a gap of nearly two decades, led to the derivation of highly accurate main field models (Olsen et al., 2000; Olsen, 2002), but resolution of the crustal field was affected by the higher orbital altitude of the satellite (650–865 km). In July-2000, CHAMP (http://op.gfz-potsdam.de/champ/main_CHAMP.shtml) was launched into a low Earth orbit of 450 km. The present altitude of its almost circular orbit is 400 km. Its magnetometers resolve the crustal magnetic anomalies more accurately than any of its predecessors. Maus et al. (2002), using the CHAMP scalar and vector data, derived a first spherical harmonic expansion of the crustal magnetic field. The first revision MF2 (http://www.gfz-potsdam.de/pb2/pb23/SatMag/model.html) of the model of the earlier map prepared by Maus et al. (2002) includes more CHAMP satellite vector and scalar data and, hence, is a more accurate crustal field model than its predecessor. We therefore use the MF2 model for all our subsequent studies.

One way to characterise the improvements of different crustal field models is to compare their power spectra. Magnetic anomalies of the crust cover a broad band of wavelengths (or wavenumbers). A quantitative summary of the importance of different wavelengths at the Earth's surface can be obtained by considering separately the fields for various spherical harmonic degrees n by computing the power spectrum. The strength of the internal part of the field at wavelengths corresponding to n, can be measured by the square of the average over the Earth's surface. The expression of power spectrum used here is shown in Equation (1.3) and is divided by a factor $2n+1$. Figure (1.1) shows the power spectra (Mauersberger, 1956; Lowes, 1966) of the total intensity anomaly at 400 km altitude of several lithospheric field models, together with the spectrum of our CHAMP model (Maus et al., 2002). The comparison of power spectra of different lithospheric field models shows a discrepancy in Figure (1.1) by a factor 10 in magnitude. Figure (1.2) shows the power spectra of field models computed by our group at GFZ using the CHAMP and Ørsted data. Interestingly, all the spectra exhibit similar power, stating that the field models derived using these data are more reliable and accurate than the models derived using Magsat data. This is an exciting result for the larger geomagnetist community because the field models derived using POGO and Magsat satellites were partly erroneous due to the error in their raw data (Ravat et al., 1995) and the new satellite data is now providing increasingly accurate field models. There were obvious discrepancies in interpreting different field models derived using POGO and Magsat satellite data. Therefore, they were not able to make much of an impact to the contribution of solid earth sciences. On the contrary, after a gap of nearly two decades, the lithospheric field models computed using the Ørsted and CHAMP data provided a very good estimate of magnetic anomaly features. These field models are compared in the Figure (1.5) for CHAMP and in Figure (1.6), for Ørsted derived vertical field anomaly

maps. Even the small-scale anomaly features are delineated (half wavelength ~ 250 km) accurately and the patterns match well. This shows that the anomalies observed by these satellites are genuine and real.
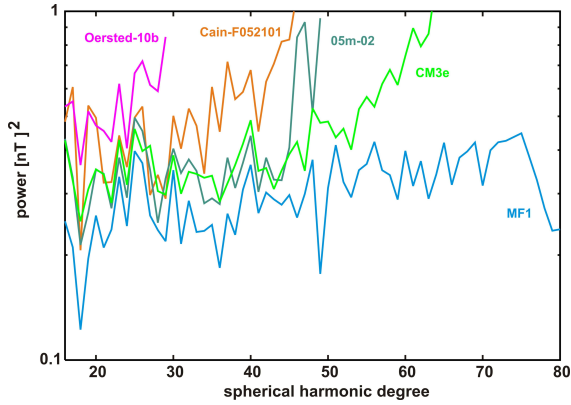
Fig. 1.1. Power Spectra of the total intensity anomaly (Mauersberger-Lowes spectra/2n+1) at 400 km altitude of lithospheric field models derived by various workers from Magsat, POGO, Ørsted and CHAMP data.
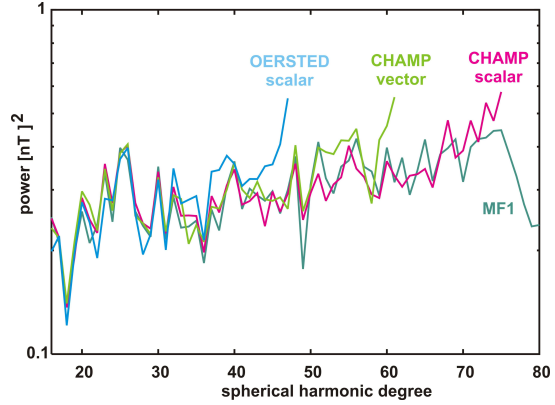
Fig. 1.2. Power Spectra of the total intensity anomaly (Mauersberger-Lowes spectra/2n+1) at 400 km altitude of Ørsted and CHAMP lithospheric field models derived by our group.

1.4 Preparation of field models for interpretation

The vertical field as seen by CHAMP is shown in Figure (1.3). It shows the dominance of magnetic field from the Earth's core (main field) and masking of the magnetic field from the crust and, hence, no meaningful information about the crust can be extracted from this map. In order to study the Earth's magnetic field of the crust it is necessary to remove the field of the core and interpret the residual map. It would seem that to differentiate and eventually separate the field originating from the sources within the crust and that from the core of the Earth would be an easy task. On the contrary, it is not so. From the Figure (1.3), it is evident that the long wavelengths caused by the Earth's core or the main field masks the signals from the crust and hence we cannot see the signals from the crust. To find a solution to the problem, Langel and Estes (1982), worked out an easy way by analyzing the power spectra of the internal field model and subsequently removing the long wavelength features. The procedure is described below.

As the coverage of the satellite survey is in a spherical shell, the most common technique to construct field models from satellite data employs spherical harmonic analysis. Gauss showed as early as 1839 that the magnetic field due to sources internal to the Earth could be represented at any point (r, ϕ, θ) outside the Earth:

$$B = -\nabla V \tag{1.1}$$

6
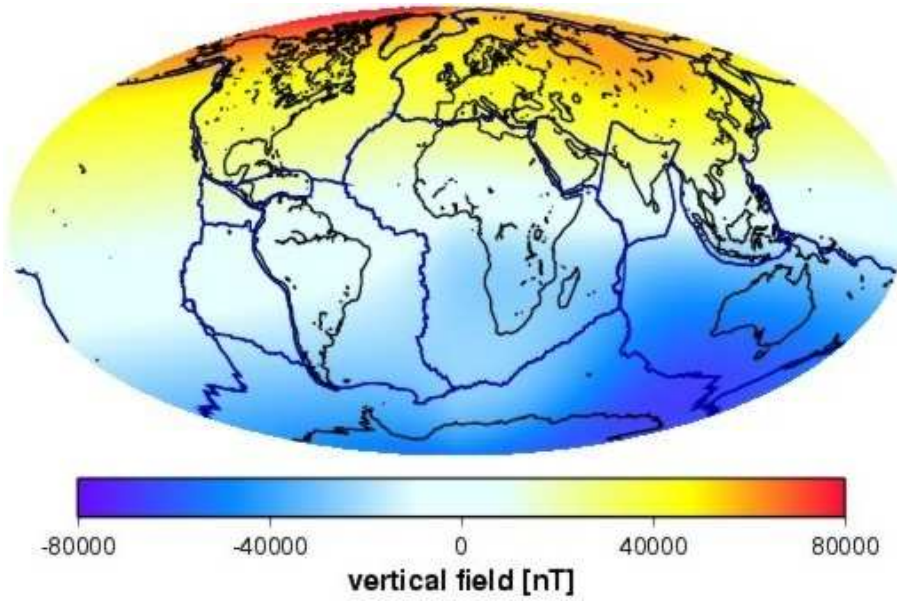
Fig. 1.3. Internal field model for the vertical component at an altitude of 400 km.

where V can be replaced by a spherical harmonic expansion of the form

$$V = a\sum_{n=1}^{N}\sum_{m=0}^{n}\left(\frac{a}{r}\right)^{(n+1)}\left[g_n^m \cos m\phi + h_n^m \sin m\phi\right]P_n^m(\cos\theta) \tag{1.2}$$

where, a is the mean radius of the Earth, and P_n^m are the Schmidt normalized associated Legendre polynomials. The terms g_n^m and h_n^m are called the Gauss coefficients and are identified by their degree n and order m.

Langel and Estes (1982) used these spherical harmonic coefficients to estimate the Mauersberger-Lowes power spectra (Mauersberger, 1956; Lowes, 1966) of the global magnetic field model given by:

$$\text{Power} = R_n = (n+1)\sum_{m=0}^{N}\left[\left(g_n^m\right)^2 + \left(h_n^m\right)^2\right] \tag{1.3}$$

They plotted the power spectrum for their global magnetic field model. Langel and Estes (1982), interpreted the steep part of the spectrum (n<14) to be caused by the sources in the Earth's core i.e., dominated by the main field or the core field and the flatter part of the spectrum to be dominated by the crustal sources. They removed the degrees less than 14 to obtain the crustal magnetic anomaly map by attributing the higher degrees (n>14) to be mainly from the crust. The transitional degrees 13-15 were attributed to signals from both the core and the crustal sources.

7

Fig. 1.4. Mauersberger-Lowes power spectra (Mauersberger, 1956; Lowes, 1966) of an internal field model from CHAMP and Ørsted data.
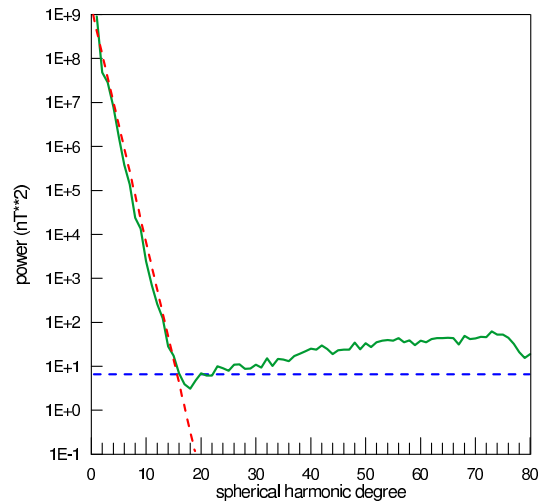
Following a similar approach, using the internal field model derived using Ørsted and CHAMP data, the power spectrum is computed for all the degrees 1-80 and is plotted in Figure (1.4). MF2 model is calculated up to a maximum spherical harmonic degree of 80 (http://www.gfz-potsdam.de/pb2/pb23/SatMag/model.html). The figure shows a change in the slope of the curve between spherical harmonic degrees 13-15. This means the degrees 1-13 are dominated by the long wavelengths of the main field. The degrees 14-15 are transitional as both the wavelengths from the main field and crustal field are present. However, the higher degrees from 16-80 are now dominantly crustal in origin (Fig. 1.4). The present work retains this distinction based on the power spectrum studies and spherical harmonic degrees 1-15 are removed from the internal magnetic field model to produce crustal field anomaly map for degrees 16-80. In the process, some part of long wavelength features of the crust is also removed and is evident from the Figure (1.4). Arkani-Hamed and Strangway (1985) and Harrison et al. (1986) based on a similar study independently concluded that the crustal portion of the magnetic field is limited to degrees 19 and greater. However, removing degrees 1-18 would further reduce the long wavelength component from the crust and, hence, it is not appropriate to interpret only degrees 19 and beyond.

The crustal field model at an altitude of 400 km computed using CHAMP data for degrees 16-80 for the vertical component is shown in Figure (1.5). The anomaly patterns now reveal features having sources in the crust. This map can now be used to find the sources causing the anomalies. Just to confirm the consistency and genuine existence of these anomaly patterns the degrees 16-80 using only Ørsted data is also shown in downward continued map at the same altitude (Fig. 1.6). A comparison of the two maps clearly points that the anomaly patterns match well. Even the comparable power spectra of the two maps already discussed in section (1.3) (Fig. 1.2), show that the anomaly patterns are real and genuinely of crustal in origin. It is hoped that interpretation of such maps should reveal new information and also confirm previous results about the magnetic sources within the crust. It should be quoted that even though Ørsted satellite is in higher orbit the data is utilized to produce such good lithospheric map and it matches extremely well with the one produced by much lower orbital altitude of CHAMP. We now discuss

8

the usefulness of these maps and the modelling techniques used till now to retrieve information from them.
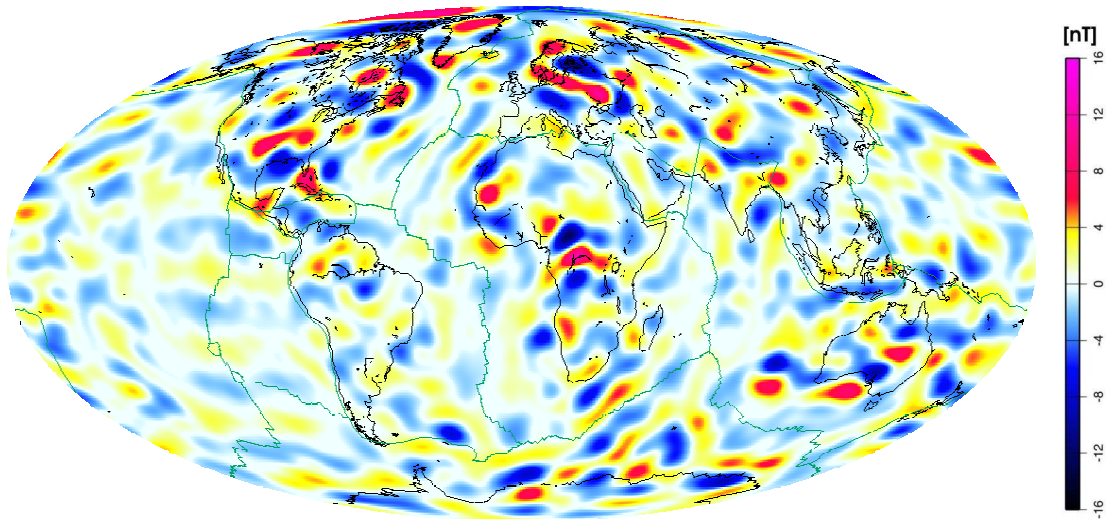
Fig. 1.5. Lithospheric field model for vertical component derived from CHAMP scalar data at 400 km for degrees 16-80.
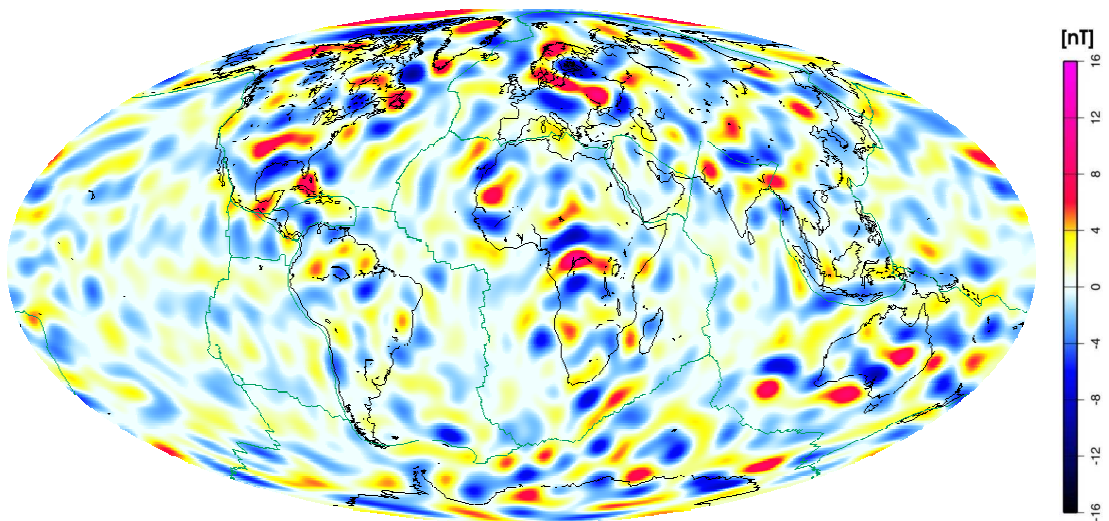
Fig. 1.6. Lithospheric field model for vertical component derived from Ørsted scalar data at 400 km for degrees 16-80.

1.5 The objective of deriving the lithospheric field models

One objective of deriving these crustal field maps is to characterize the sources causing these anomalies and to interpret these maps in terms of known geology. The interpretation methods commonly employed often consist of visual comparison of an anomaly map with geologic or tectonic maps. Many of the earliest interpretive studies of satellite anomaly maps were of this type. Hastings (1982) compared the features of scalar

Magsat anomaly map with that of the tectonic map of Africa. Induced magnetisation was assumed as the source for the anomalies in their work. Frey (1982a) using Magsat data compared the crustal scalar magnetic anomaly map with the global geological map and showed that large-scale features such as shields, cratons and subduction zones are associated with positive anomalies and basins and abyssal plains with negative anomalies. Similar studies for Asia were illustrated by Frey (1982b), for South America by Hinze et al. (1982), and for India by Achache et al. (1987). They attributed the negative anomalies to crustal thinning associated with elevated Curie isotherm in the region and vice-versa for the positive anomalies. These interpretations are oversimplified. In the above context, the Figures (1.7a), (1.7b) and (1.7c) illustrate the response for the total field intensity and the vertical field of a magnetizable body placed in an inducing main field of the earth. The positive and negative anomalies mentioned above are the total intensity (scalar) anomaly measured at various latitudes, as shown in Figures (1.7a), (1.7b) and (1.7c). Thus, a magnetizable body placed in the inducing main field of the Earth can be replaced by a dipole of comparable magnitude and direction. The large geological regions mentioned above were modelled by those authors accordingly, to find the direction and magnitude of magnetisation.
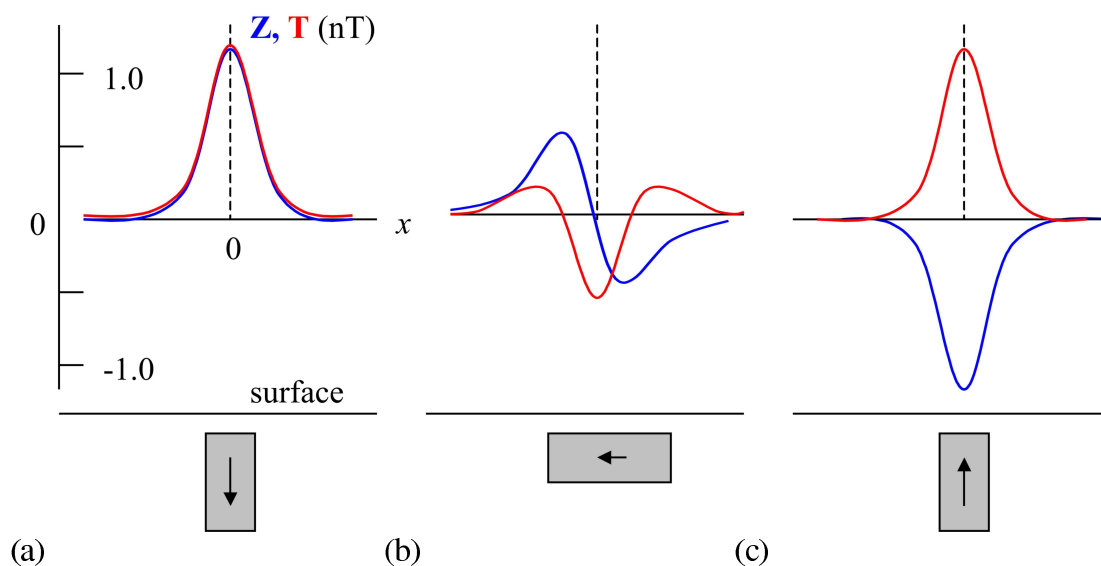
Fig. 1.7. Profiles for (a) vertical dipole located at north pole, (b) horizontal dipole located at equator, and, (c) vertical dipole located at south pole. Lines in red are the total field anomaly and in blue the vertical field anomaly for a dipole (marked in arrows) induced and directed along the main field of the earth.

More quantitative interpretations involve direct comparisons between geophysical quantities such as gravity, heat flow and depth to the Moho. The ultimate aim, however, is to extract geological and tectonic information from the crustal anomaly maps and to explain the inferred geology in terms of tectonic and geologic processes. The distribution of magnetisation is not uniquely determined by the magnetic field and, hence, is often estimated using constraints from other geoscience data (e.g., surface geology, gravity, and heat flow). Mayhew (1979), von Frese, Hinze and Braile (1981) and Whaler and

Langel (1996) followed such methods to find the susceptibility and magnetisation distributions.

Forward modelling methods based on initial model information are those given by Meyer et al. (1983) and Hahn et al. (1984). These are global models of the crust composed of two- or three-layers. The crustal model defined by Meyer and Hahn was global grid representing the various geological regions. Assuming only induced magnetisation, each block-layer was represented by a dipole directed along the main field, with susceptibility assigned based on a classification into one of 16 crustal types. The classification was based on surface geology and seismic investigation. Layers classifications, with magnetisation in amperes per meter in a 50,000nT field in brackets, were as follows: sea water (0), sediments (0), upper oceanic layer (1.0), upper continental layer (1.0-2.0), lower crustal layer (0.5), intermediate crustal layer (1.2), and sub-Moho (0). Comparison of the modelled magnetic field showed some local agreement with measured anomaly maps, but in general, their models did not reproduce the observed anomaly features. This initial model proved to be too general and hence the results were largely in disagreement with the Magsat derived magnetic anomaly map.

Purucker et al. (1998) derived a simple *a priori* model magnetisation distribution for both continents and oceans, termed "Standard Earth Magnetisation Model", or SEMM-0. The continent-ocean margin was placed at the 1-km bathymetric contour. Values of susceptibility were assigned to continental crust (0.025 SI units) of thickness 40 km, and oceanic crust (0.04 SI) of thickness 7 km, and remanent magnetisation (0.1 SI) to Cretaceous Quiet Zones (KQZ) within the oceanic crust. The model takes the form of 11,562 equivalent point dipoles, each representing a region equal to a 1.89^0 X 1.89^0 area at the equator. Except in the KQZs, the magnetisation direction was assumed to be along the direction of the ambient main field. Using a random search inverse method, an equivalent source magnetisation model (SEMM), was derived by modifying the initial *a priori* model SEMM-0 until the resulting anomaly pattern matched a Magsat-derived magnetic anomaly map in a least-squares sense. SEMM models were presented in terms of the product of susceptibility times thickness. The inherent drawback of the SEMM-0 model is the simplification of magnetic properties of the crust, particularly for the continents where lateral variations in susceptibility are large. Recently, Purucker et al. (2002) modified the continental crustal thickness of their *a priori* model based on heat flow provinces of the world. Cratons are older crust and hence were considered to be associated with low heat flow. Basins are made of younger crust and comparatively have a higher heat flow (Taylor and McLennan, 1985). Based on the heat flow value in the cratons and in the younger crust the thicknesses of the cratons was estimated to be 81 km while in the basins it was only 20 km. The basic methodology to arrive at the final model remained the same. This model also lacked lateral variation in magnetic properties of the crust, though the incorporation of heat flow measurements improved the results marginally.

In addition to the drawbacks of the above models, the interpretation of magnetic anomalies is further complicated by certain uncertainties, which are discussed next.

1.6 Ambiguities in interpretation

The interpretation of anomaly maps is not straightforward but is complicated by ambiguities inherent in the interpretation of magnetic anomaly maps. One of the first ambiguities is that it is not possible to distinguish whether the anomaly pattern is due to remanence or induced magnetisation. This means all the anomaly patterns observed can be explained just by induced magnetisation (Maus and Haak, 2003). Making the interpretation more complex is the lack of vertical resolution. Satellite and airborne magnetic data can only infer height integrated magnetisation, i.e., thickness multiplied by susceptibility. So, it is immaterial to place the source body at the surface of a region or deep inside, as the satellite data cannot distinguish its location in the vertical column. However, *a priori* information like stratigraphy can partially alleviate the problem. One of the inherent problems is the unability to remove the short wavelength component of the main field completely from the lithospheric anomaly maps. Removal of the long wavelength part of the main field also removes the long wavelength component of crustal sources. A further ambiguity is caused by the presence of magnetic field annihilators. Some susceptibility distributions across the magnetic equator in the presence of a dominantly dipolar inducing field produces no observable magnetic field outside the earth (Maus and Haak, 2003). Another annihilator derived by Runcorn (1975), states that a homogeneous spherical shell magnetized from the inside does not produce a magnetic field outside of the Earth. The presence of anomalies due to remaining external fields aggravates the problem, especially in the polar and equatorial regions where the external sources show most affect. In order to reduce the affects of these ambiguities, a forward modelling technique to interpret the anomalies is followed. The modelling method employs some simplifying assumptions, which are described in the following paragraph.

1.7 The present work

The work presented here is a Geographical Information System (GIS) based forward modelling technique developed to model the various geological units of the continents and oceans using a standard geological map (CGMW, 2000). Unlike the global models of Hahn et al. (1984) and Purucker et al. (1998), which assumed a single susceptibility value for all the continents in their initial model, the initial global model derived here is highly variable and each geological region of the world has a unique susceptibility value. The derivation of this susceptibility value depends upon the known rock types exposed in a geological region, and a standard susceptibility value is derived by mathematically averaging the susceptibility values for all the identified rock types. Multiplying the average susceptibility value for the geological region of the upper crust by a constant factor derives the susceptibility value for the lower crust. This factor is based on the work by Taylor and McLennan (1985) who proposed an average composition of the upper and lower continental crust. Using the global seismic crustal structure, a vertically integrated susceptibility (VIS) model is computed for a geological region by integrating the contribution of average susceptibility times thickness of the upper crust and susceptibility times thickness of the lower crust below that region. A global VIS model is derived by knitting the VIS value for all the geological units of the world. Starting with this initial

global VIS model, the vertical field anomaly is computed at an altitude of 400 km and compared with the CHAMP vertical field anomaly map. The model derived first is the *initial model*. In the next iteration, some specific regions are selected for detailed analysis where the *initial model* is in disagreement with the observed magnetic anomaly map. The parameters, which are to be defined later in chapter 2, are changed based on the information from other published results, to improve the fit between the predicted and observed magnetic anomaly map. This refined model, called the *first iteration* model, is then used to draw inferences about the tectonic and geologic features underlying the younger crust and the nature of the less-understood lower crust.

Assumptions in the present work:

The present work incorporates some simplifying assumptions because of the inherent ambiguity of the magnetic inverse problems.

1. Moho is considered a magnetic boundary. This is supported by the work of Wasilewski and Mayhew (1992), who find the Moho to be the lower boundary of the magnetic crust above a non-magnetic upper mantle below. This implies that the region above the Moho discontinuity is the sole source for the crustal anomaly. The assertion of Haggerty (1978) that the serpentinisation of upper mantle may produce magnetites is still debated, as the work of Wasilewski et al. (1979) and Wasilewski and Mayhew (1982) provided no evidence of magnetites in the xenoliths from the upper mantle. A apart from the evidence from mantle xenoliths, the assumption of the Moho as a magnetic boundary greatly simplifies the modelling because the depth to the Moho is readily available from seismic crustal model.

2. The present work assumes the upper and the lower crust not to contain remanence. The inability of magnetic anomaly maps derived using satellite and airborne data to distinguish the anomalies due to induced or remanent magnetisation allowed us to assume the induced magnetisation as the only source for the anomaly.

It is further added that the present geothermal models (Artemieva and Mooney, 2001) are not accurate enough with the present resolution being 10^0 X 10^0, in addition to large gaps in the data especially in Africa and South America. Hence, they have not been included in the present work.

Our basic assumption that Moho is a magnetic boundary is likely to be a gross simplification in many regions of the world (Chapman and Furlong, 1992). Our efforts through the present work are to detect such anomalous regions, which would be helpful in understanding the composition of lower crust in those regions and possibly modify our *initial model*.

Aim:

The present work concentrates on the interpretation of anomalies observed over the continents. Our efforts here are not only to understand these anomalies but, in particular, to infer geological information from these maps.

Chapter 2

Global Crustal Magnetisation Model

2.1 Introduction

The varying pattern of Earth's regional magnetic anomalies is caused by a complex superposition of geological features in the lithosphere, covering a broad spectrum of wavelengths. These anomalies are caused by lateral variations of the bulk susceptibility contrasts of the crust. Their sources are ferrimagnetic minerals, predominantly magnetite. They occur in varying quantities in the igneous and metamorphic rocks and to some extent in some sedimentary rock types like banded iron formations (BIF) of all geological ages. Most of these rocks are hidden by overlying younger, generally nonmagnetic, sediments and sedimentary strata, both on the continents and in the oceans.

This chapter provides a review of the crustal tectonic units which are the sources of the magnetic anomalies within the continental lithosphere. Although considerable effort has been put into investigating the magnetic properties of minerals, such studies have focused largely on minerals of direct or indirect importance in magnetic surveys, exploration for natural resources, and for paleomagnetic studies. Much less is known about the nature of geological processes and the resulting magnetic properties of rocks. Even more important is our lack of knowledge of the magnetic character of the lower crust and the upper mantle. Also, the present knowledge of the deeper portions of the lithosphere is rather rudimentary, largely because of the limited access to xenolith samples from those depths. As found by Hall (1974), some long wavelength anomalies correlate with exposed upper crustal sources. This means that upper crustal magnetisation may be an important contributor to long-wavelength anomalies and lower crustal composition may be reflected in surface geology. Blakely and Griscom (1988) continued the aeromagnetic map of North America to a higher altitude and found excellent correlations with Precambrian and Paleozoic provinces. In another study of granitoids of various regions, Chappell et al. (1988) demonstrated that the composition of granitoids largely reflects the composition of their source regions. The distribution of granitoids suites can be used to define terranes, within each of which the lower crust has distinctive geochemical characteristics. Thus, following the geophysical and geochemical investigation as mentioned above, it was desired to adopt a modelling procedure where, based on the surface geology, the geology of the lower crust was assumed to be having the same geochemical characteristics. Hence, we started compiling the rock types exposed at the surface of all the Precambrian regions of the world.

2.2 Geology of the continents

The sources of the continental magnetic anomalies primarily consist of the rock types formed early in the geological history of the earth. The complete stratigraphy of the rock units is categorized in two broad units, the older unit called Precambrian(>570 Ma), and the younger Phanerozoic. The Precambrian unit is further subdivided into an older rock section called Archean(>2500 Ma) and the younger Proterozoic. According to Taylor and McLennan (1985), 75% of the earth's crust had already formed at the end of the Archean. A glance at the anomaly map (Fig 1.5) clearly points to the fact that most of the anomalies lie over the geological regions occupied by Precambrian rocks, either exposed or hidden by younger Phanerozoic cover. However, the exposed Precambrian rocks constitute only 29% of the total Precambrian crust (Goodwin, 1991). This means that a significant portion of the oldest crust on Earth is overlain by Phanerozoic cover. Hence, our aim is to look for the possible extensions of the Precambrian units obscured by younger cover and possibly add to the existing knowledge of geological boundaries of the Precambrian units. For this it is necessary to consider the known geology of the region and its boundary at the surface. This is mentioned in the following subsections. However, for the detailed geology the reader is referred to the references mentioned therein.

The bulk of Earth's Precambrian crust is located in nine Precambrian cratons, which center the main continental masses, Asia, Europe, Greenland, North America, South America, Africa, India, Australia and Antarctica. The Precambrian cratons comprise both the exposed shields, generally termed as cratons, and the buried, i.e. sub-Phanerozoic called Precambrian basement. Additional Precambrian crust lies within median massifs, called inliers, within cratons enclosing Phanerozoic mobile belts and isolated continental fragments scattered in the oceans.

2.2.1. Cathaysian craton

The Cathaysian craton shown in Figure (2.1) comprises three cratons- Sino-Korean (north China), Tarim and Yangtze (southwest China). The Sino-Korean craton includes most of north China and the southern part of northeast China and part of North Korea. Archean rocks are concentrated in the central eastern parts of the craton, where they form the Ordos and Ji-Lu nuclei. The rocks are exposed especially in Shanxi plateau and Jiaoding-Liaodong region in the north and in Henan province along the southern margin. The Tarim craton is situated between Tianshan mountains in the north and the Kunlun-Arjin mountains in the south. Precambrian basement, locally exposed at the periphery, comprises Archean gneiss and early to mid Proterozoic rocks. It is overlain by Paleozoic marine clastics and Mesozoic-Cenozoic sediments. The Yangtze craton covers the territory of the lower-central Yangtze River drainage and the southern part of the Yellow Sea. Early Proterozoic rocks are confined to the periphery of the craton. The central part has extensive mid-late Proterozoic cover, which underlies Phanerozoic cover. The detailed geology can be found in the works by Zhang et al. (1984) and Yang et al. (1986). Their work has been summarised in the book by Goodwin (1991, 1996).
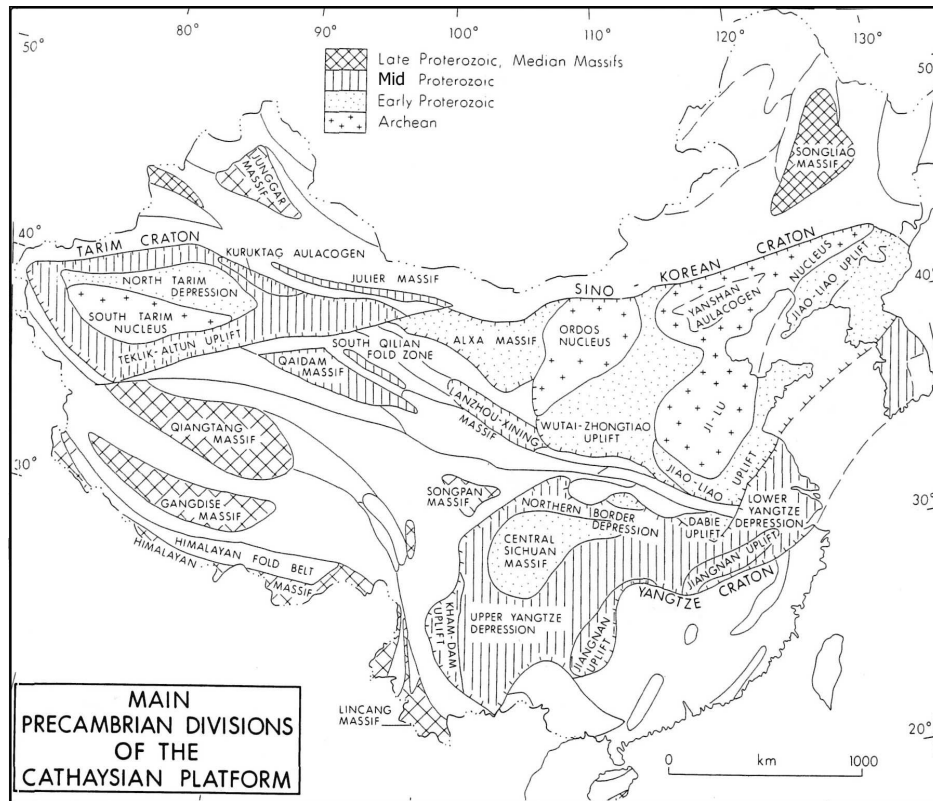
Fig. 2.1. Tectonic map of Cathaysian craton (Goodwin, 1991).

2.2.2 Siberian craton

The Siberian craton includes two main Archean to early Proterozoic shields: Aldan in the southeast and Anabar in the north (Fig. 2.2). The small Olenek uplift east of the Anabar shield lies close to the northeast boundary of the craton. In addition, Precambrian rocks are exposed in six peripheral fold belts, clockwise from the southeast: Stanovoy, Baikal, East Sayan, Yenisei, Turkhansk- the last four accreted to the craton during the end-Proterozoic Baikalian Orogeny – and, to the north, the Taymyr fold belt, which is separated from the craton by the deep intervening Khatanga trough of Phanerozoic age. Precambrian median massifs, of varying size, are present in adjoining Phanerozoic fold belts, notably Okhotsk, Taigonos, Kolyma-Omolon and Anyuy-Chukota in the northeastern Siberia, to the east. Shatzki and Bogdanoff (1959), Salop (1977, 1983), Khain (1985) and Khain(1994) studied the geology of Siberian craton in detail.

The basement of the Siberian craton is formed mainly of Archean rocks partly reworked in early Proterozoic time, with some Proterozoic filled troughs. The basement is submerged to varying depths, forming a number of large depressions filled with sedimentary cover. The main depressions are the huge Triassic trap-filled Tunguska syneclise in the northwest and the Mesozoic Vilyui syneclise in the east, the latter a northeastern extension of the Chara-Lena trough. Syneclises are regions characterised by thick sedimentary cover over the basement, while anteclise are the regions where the

17

basement is raised with respect to the surrounding, and consequently overlying sediments are thin.
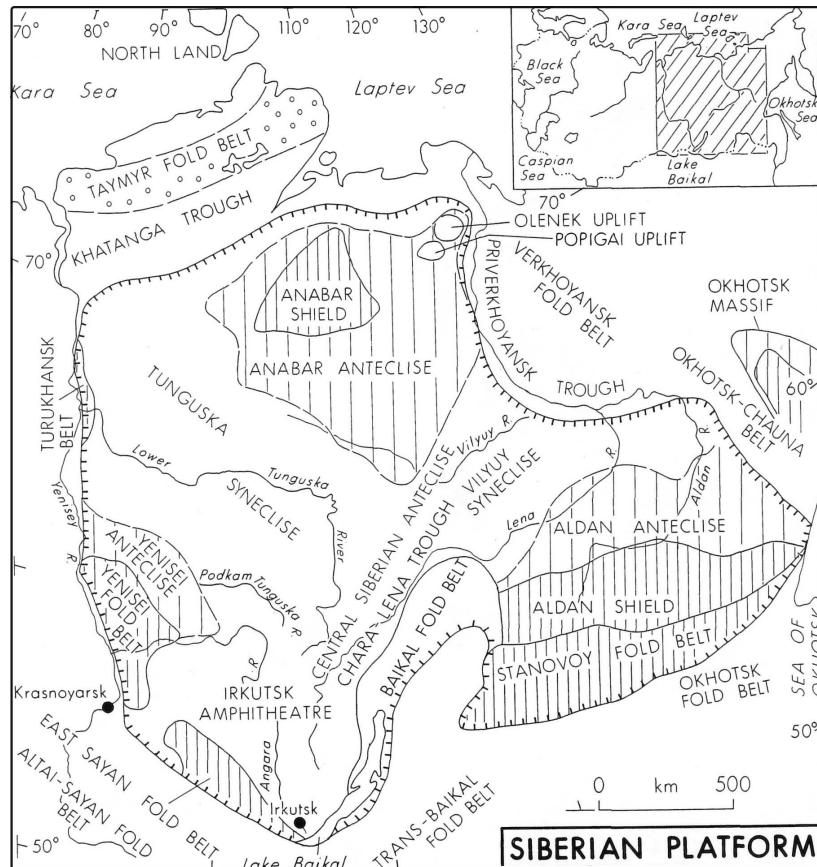
Fig. 2.2. Tectonic map of Siberian craton (from Goodwin, 1991; after Shatzki and Bogdanoff, 1959; Salop, 1977).

2.2.3 East European Craton

The craton shown in Figure (2.3) includes two prominent shields: the larger, rectangular, partly submerged Baltic shield in the northwest and the smaller, curvilinear Ukrainian shield in the southwest. Positive elements include the slightly buried Voronezh anteclise (uplift) and Volga-Urals anteclise to the east and Belorussian anteclise to the northwest. The Riphean-Vendian-Phanerozoic cover is 2-4 km thick but increases in thickness in the main depressions, notably the Moscow-Baltic syneclise in the north and the North Caspian syneclise in the south, the latter attaining the remarkable maximum thickness of 23 km. Goodwin (1991) and Khain (1985) have compiled the detailed Precambrian geology of these regions. The references mentioned therein can also be referred to.

The Baltic shield is divided by deep faults or other tectonic zones into five major provinces, namely, the Kola peninsula in the northeast, the adjoining Belomorian province to the west, the nearby Lapland granulite belt, the succeeding Karelian province to the west extends southward from the Caledonide front to the Lake Onega. The large

18

Svecofennian province occupies the central part of the Baltic shield and in the southwest the Sveconorwegian province dominates in southern Norway and Sweden.
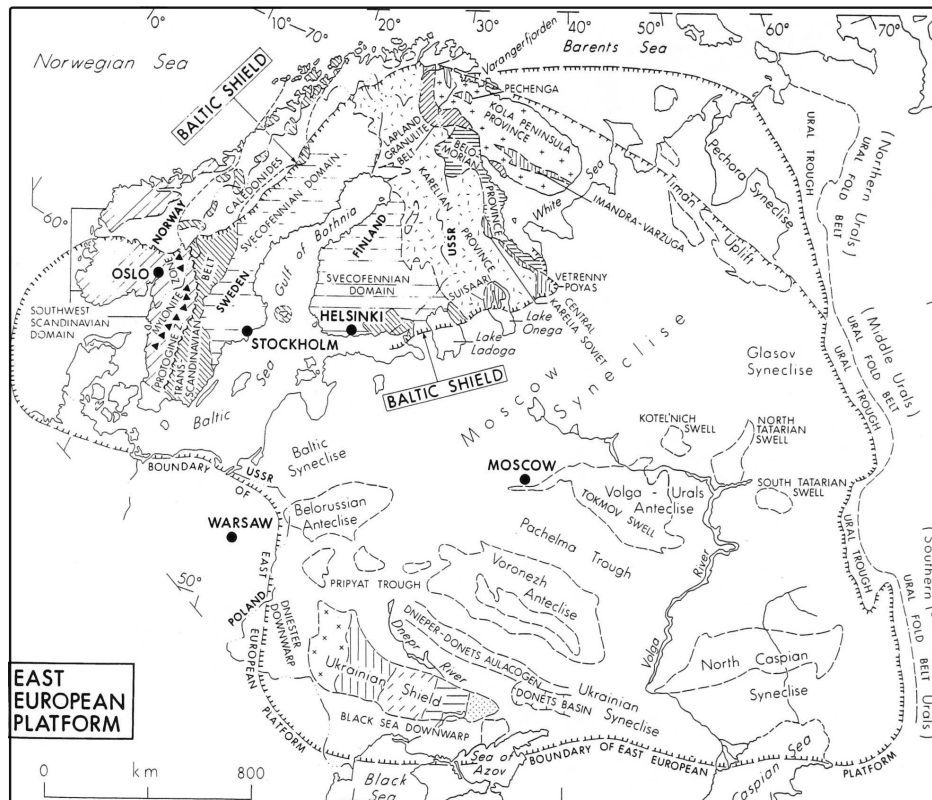
Fig. 2.3. Tectonic map of East European craton (from Goodwin, 1991; after Khain, 1985; Shatzki and Bogdanoff, 1959).

The Ukranian shield consist of five Principal Archean Blocks: Volyn, Bug-Podolian, Kirovograd, Middle Dnieper and Azov. The Archean blocks are separated by narrow meridional Banded Iron Formation (BIF)-bearing early Proterozoic blocks. Among these, Krivoy Rog extends for more than 220 km, as traced by drilling and a total distance of 1000 km, by magnetic anomalies, reaching the Kursk magnetic anomaly of the Voronezh massif located 300 km to the northeast.

The buried basement of the East European Craton comprises 23 relatively small, isometrically-elongated Archean blocks (massifs) with intervening early Proterozoic fold belts. The basement was later buried during the Riphean-Vendian time, with Late-Proterozoic-Phanerozoic cover of varying thickness. The Timan-Pechora occupies the extreme northeastern part of the Russian plain and is separated from the East European Craton by the NW-trending Timan ridge. A long string of Precambrian Massifs lies along the Uralian Fold Belt, which is situated to the east of East European Craton. It comprises large uplifts, notably, Bashkir Uraltau, in the western Uralian zone. Precambrian crystalline rocks are also present in Variscan inliers, mainly, Armorican, Central, Bohemian and Iberian Massifs. The British Isles are largely covered with Caledonide massifs.

19

2.2.4 Greenland

Inland ice covers 80% of Greenland and, hence, exposures are seen only at the periphery of the continent. Four major structural provinces are recognized in the Precambrian craton of Greenland shield as shown in Figure (2.4). An old Archean block is present in the south of the plateau which is flanked by the Nagssugtoqidian belt to the north and the Ketilidian belt to the south, early Proterozoic in age. To the north of Nagssugtoqidian belt occurs a very broad early Proterozoic Rinkian belt. Some of the older rocks in the Isua region of the central west Greenland have provided one of the oldest preserved rocks on Earth, which date back to 3820 Ma. The east of Greenland is dominated by the Caledonides. Spitsbergen Archipelago, to the northeast, includes patches of Late Proterozoic metsupracrustal rocks. Notable contributions are from Moorbath et al. (1973), Bridgwater et al. (1976), Myers (1984) and Goodwin (1991).
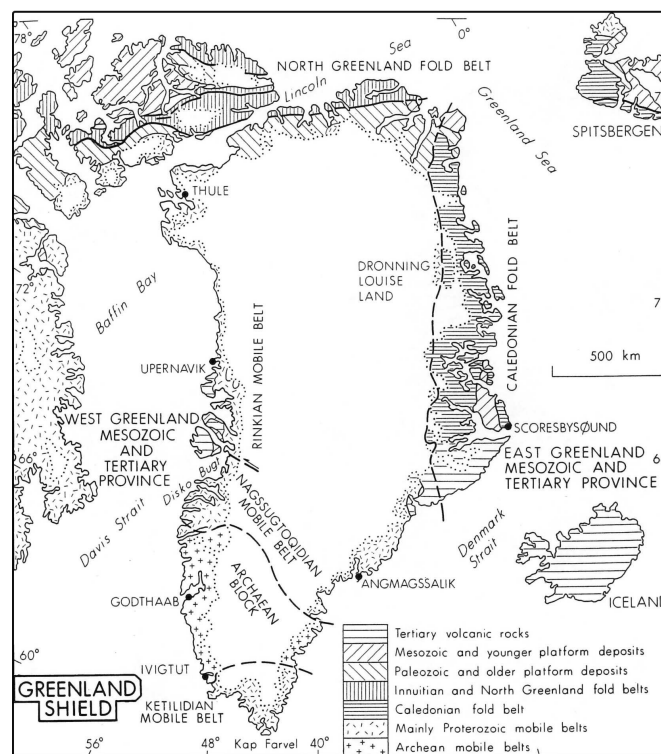
Fig. 2.4. Tectonic map of Greenland shield (from Goodwin, 1991; after Escher and Watt, 1976).

2.2.5 South American craton

The South American craton, as shown in Figure (2.6), comprises three exposed shields – Guiana, central Brazil and Atlantic and buried precambrain basement beneath three large basins, Amazon, Parnaiba and Parana. Guiana Shield contains (1) three comparatively small Archean nuclei – (a) the tectonically overthrust Imataca complex in the north, (b) the poorly defined Pakairama craton in the center-west and (c) the Xingu craton (northern

20

segment) in the southeast; (2) greenstone bearing early Proterozoic Maroni-Itacaiunas Mobile Belt; (3) in the west, NW-trending mid-Proterozoic RioNegro-Juruena Belt.

The Central Brazil shield predominantly consist of (1) Guapore craton, in the western sector (Gibbs and Barron, 1983), represents the southern extension of the Guiana shield south of the Amazon basin. The subordinate eastern sector of the central Brazil shield constitutes the Tocantins province (Almeida et al., 1981).

The Atlantic shield comprises three structural provinces: São Francisco, Barborema and Mantiquiera. Small adjoining basement fragments include São Luis craton in the north and Rio de la Plata craton in the south.

The mid-Proterozoic San Ignacio belt of the Bolivian shield area, is covered by Cenozoic sediments. The adjoining (to the southwest) Sunsas-Aguapei (Rondonian) Belt lines up with basement inliers in Bolivia, Peru, Ecuador and Columbia. The key reference is Litherland et al. (1985).
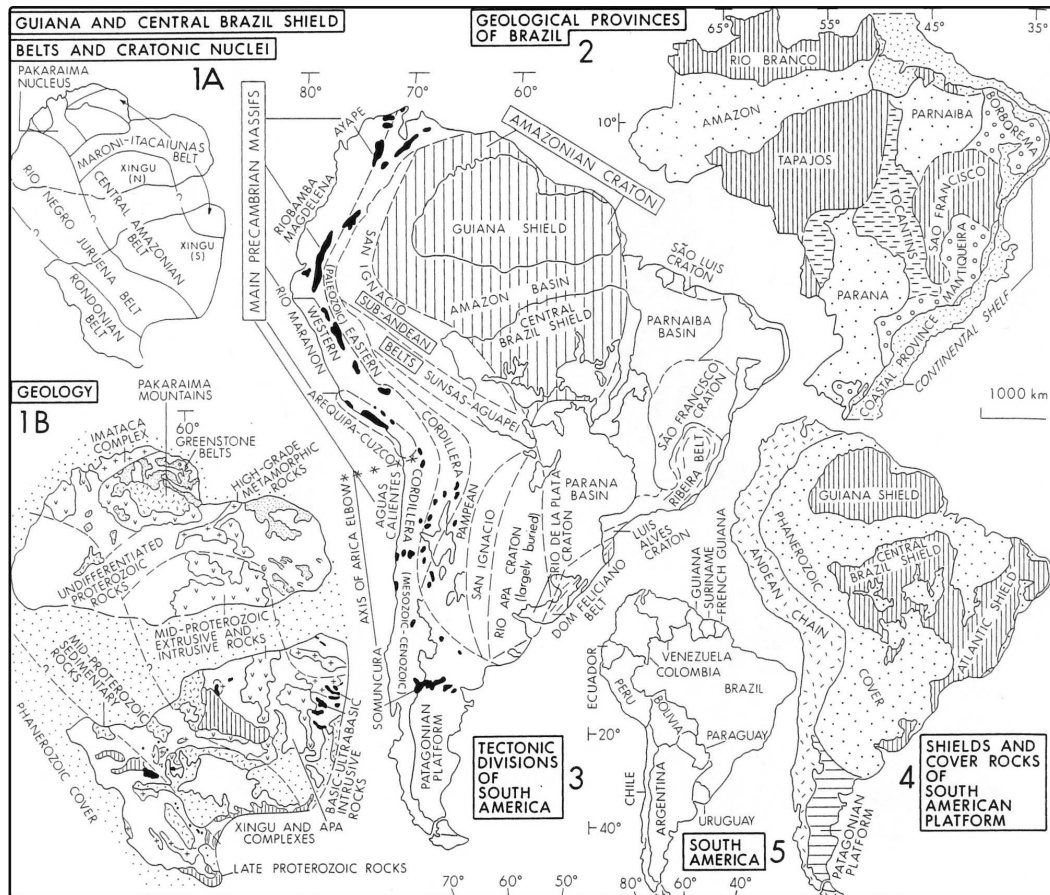
Fig. 2.5. Tectonic map of the South American craton (from Goodwin, 1991; after Almeida et al., 1981; Litherland et al., 1985).

21

2.2.6 North American craton

The North American craton forms a large ovoid craton and is encircled by Phanerozoic fold belts (Fig. 2.5). About one-third of the complete craton is exposed, dominated by the uniquely large Canadian Shield and a small circular Wyoming uplift in the southwest (Goodwin, 1991).
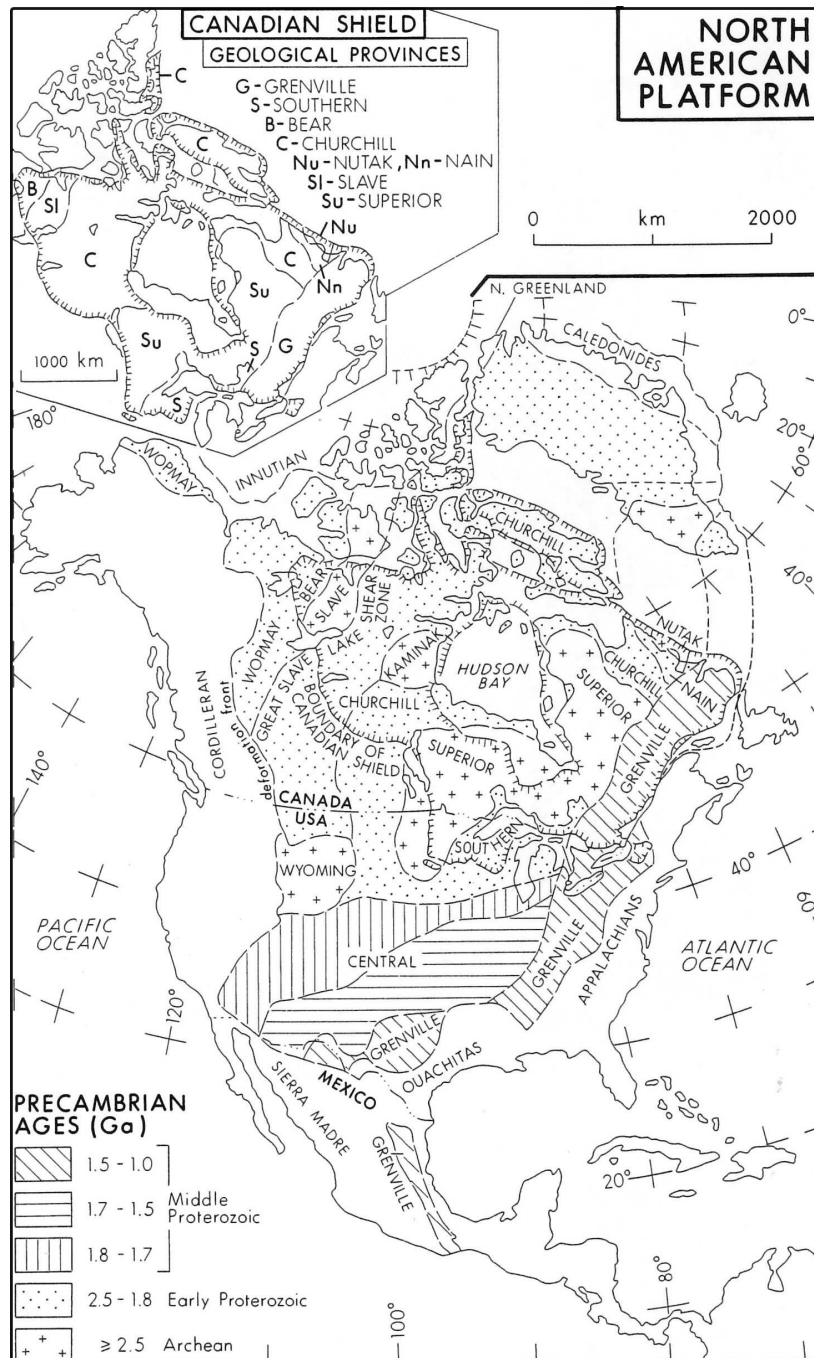
Fig. 2.6. Tectonic map of the North American craton (from Goodwin, 1991; after Hoffman, 1989).

22

The Canadian shield is a large craton, and at its center lies the Phanerozoic-filled Hudson bay. The Shield is divided into seven tectonic provinces. Of these, two (Superior and Slave) are Archean in age, three (Churchill, Bear and Southern) mainly early Proterozoic, one (Nain) Early mid-Proterozoic and one (Grenville) late mid-Proterozoic. Late Proterozoic rocks are confined to the continental margins.

Buried extensions of Superior province lies to the north in James bay and Hudson bay, of Slave province to the north in Arctic craton, of Churchill province to the north also in Arctic craton and southwest in Interior craton and Cordilleran belt, of Bear province to the north in Arctic craton and west in Interior craton and Cordilleran belt, and of Grenville Province to the south and southwest as far as Mexico in Interior craton and Appalachian belt. Central Province (belt) is a large structural province, which underlies the south-central USA. The rocks of these provinces are exposed only at a few places in Colorado and California. Large anorogenic magmatic activity is dominant along the entire stretch of this province.

Numerous Precambrian inliers are distributed in the adjoining Cordilleran, Appalachian and Innutian fold belts. Allochthonous slices are distributed in the Phanerozoic fold belts of the Innutian (eastern and Western Arctic Regions), Cordilleran (Yukon, Alaska, British Columbia, Alberta and western USA), Ouachitan and Appalachian (Canadian and US sectors) orogens.

2.2.7 African craton

North to south and east to west trending Pan-African belt system divides the craton into five cratons: southern (Kalahari), central (Congo), northwestern (West African), north-central (Saharan) and northeastern (Arabian-Nubian shield) (Fig. 2.7). The main intervening Pan-African belts, respectively (1) E-trending and (2) N-trending, are (1) from south to north, Damara-Katangan-Zambezi and Central African; and (2) from west to east, Rokelides (Mauritanides), Pharusian-Dahomeyan, West-Congo-Kaoko-Gariep and Mozambique. Notable contributions on the African geology are from Saggerson (1978), Black (1980), Cahen et al. (1984), Kröner et al. (1987) and Cooper (1990).

The Kalahari craton comprises three main parts: (1) in the east, the Archean Kaapvaal and Zimbabwe cratons, with intervening Limpopo belt; (2) in the west and south, the early Proterozoic Magondi and Kheis belts, mid-Proterozoic Namaqua-Natal belt with Koras-Sinclair-Ghanzi rift system; and (3) at the western margin, the small Nama basin.

Central Africa comprises a ring of ancient cratons surrounding the Congo basin. In clockwise succession from the south: the very large Kasai-Angolan composite, Chaillu, Gabon, Bouca, Bomu-Kibalian, Tanzania and Zambian. Proterozoic fold belts adjoining Tanzania craton in the east are Ubendian belt on the southwest, Usagaran belt on the south and Ruwenzori belt on the north. On the west side of Congo basin, lies West Congo

belt. On the east side of the basin, Kibaran and Irumide belts lie respectively between and south of the Kasai and Tanzania-Zambia massifs.

Northwest Africa comprises (1) the West African craton with large central Taoudeni basin and smaller Volta basin to the east; (2) the smaller Tuareg and Benin Nigeria shields; both enclosed in (3) Pharusian-dahomeyan mobile belt. The West African craton contains Man shield in the south and Reguibat shield in the north.

The basement rock of Northeast Africa and Arabia is exposed in (1) the easternmost Arabain-Nubian (Egypt-Sudan) shield; (2) farther west , as isolated inliers – Uweinat, Tibesti, Tchad, Kordofan and Nuba mountains and (3) further south they merge with basement rocks of Central Africa.
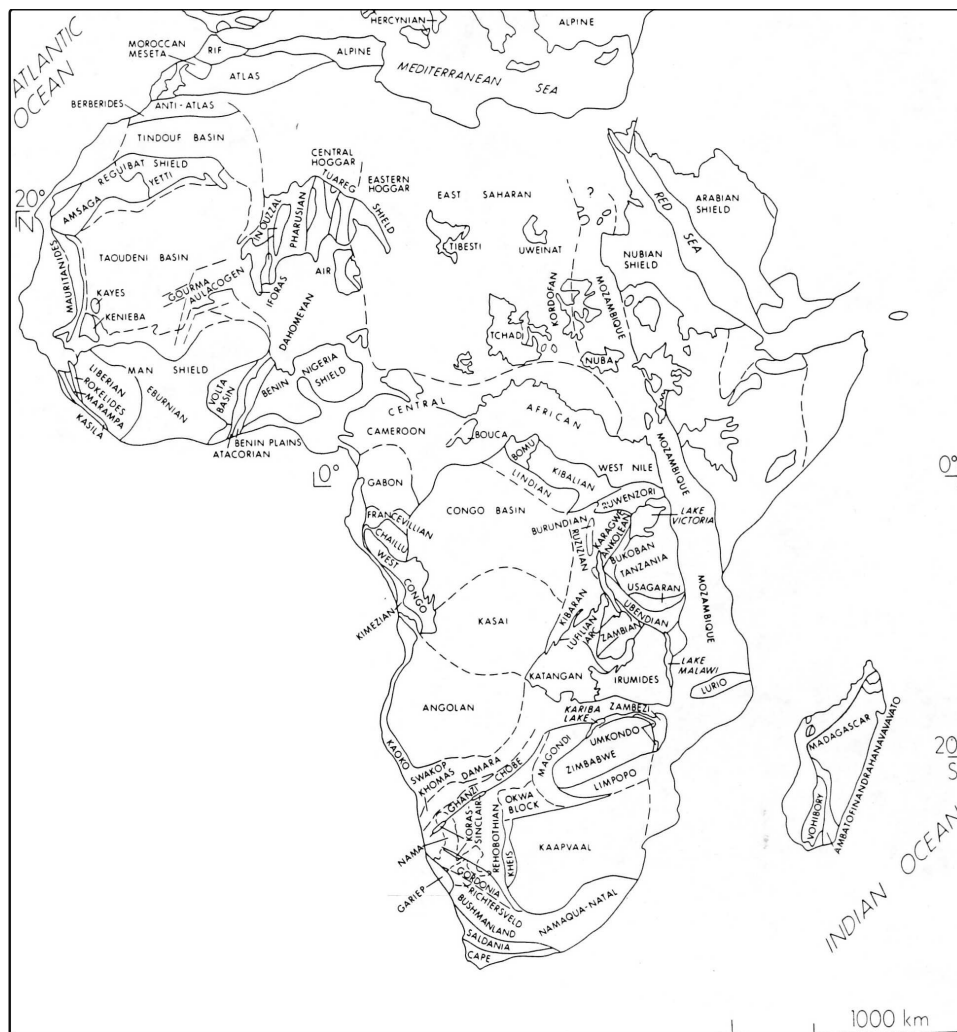
Fig. 2.7. Tectonic map of African craton (from Goodwin, 1991; after Saggerson, 1978).

2.2.8 Indian craton

Seven major tectonic regions, as shown in Figure (2.8) form the Indian craton. The Western Dharwar domain, the Eastern Dharwar domain, and Granulite domain dominate the south Indian regions. The major cratons are Bhandara craton, Chotanagpur-Singhbhum craton and Aravalli domain. The Eastern Ghats belt lies along the eastern coast of Indian peninsula. Numerous sedimentary basins include the Cuddapah in the southeast, small Chattisgarh in the northeast and very large Vindhyan in the north-centre. The island of Sri Lanka to the south is considered to represent an extension of southern India. Key references are Radhakrishna (1983), Taylor et al. (1984), Naqvi and Rogers (1987) and Moorbath and Taylor (1988).
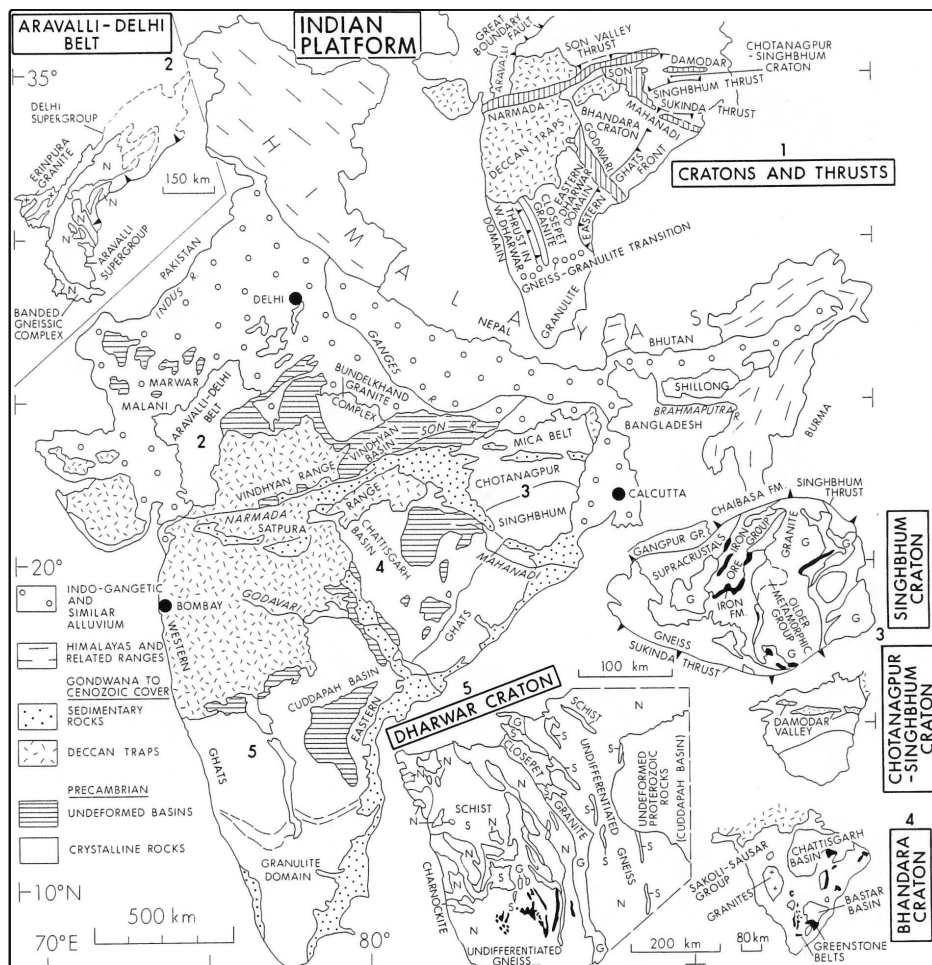
Fig. 2.8. Tectonic map of Indian craton (from Goodwin, 1991; after Naqvi and Rogers, 1987).

2.2.9 Australian craton

Precambrian rocks are divided into basement subprovinces and craton cover. Rutland (1981) recognizes three major basement subprovinces (Fig. 2.9): (1) Archean, mainly in

the west, incorporating the Pilbara, Yilgarn and Kimberley provinces; (2) older Proterozoic, mainly in the central parts, incorporating the North Australian, Gascoyne and Gawler (-Nullarbor) provinces; (3) younger Proterozoic, in the south-central part incorporating the Musgrave-Fraser province which in part lies in the Amadeus transverse zone of the central Australian mobile belt.
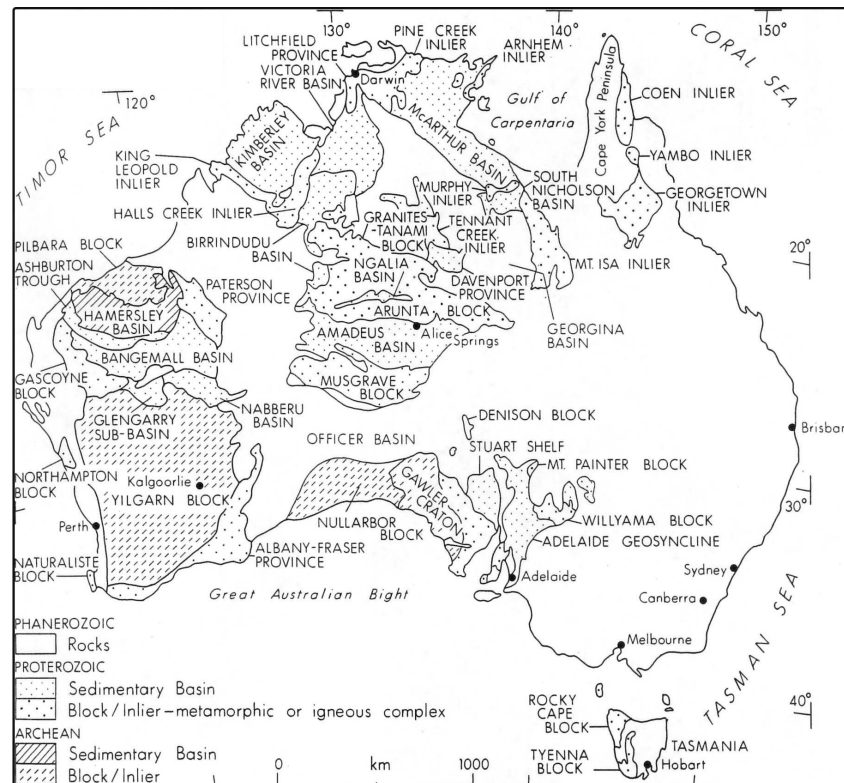
Fig. 2.9. Tectonic map of Australian craton (from Goodwin, 1991; after Wyborn, 1988).

2.2.10. Antarctic craton

Archean outcrops are present in Enderby Land and western Kemp land, the Prince Charles Mountains and Dronning Maud Land as shown in Figure (2.10). Detailed studies are available from Windmill Islands, Bunger hills, Vestfold Hills and in some specific location including Napier Complex and Rayner Complex in Enderby Land and Lutzow – Holm Bay (James and Tingey, 1983).

2.3 Oceanic crust

The oceanic crust is generally divided into three layers (Keary and Vine, 1990). Layer 1, 0-1 km thick, is sediment. Layer 2, the basement layer, is between 0.7 and 2.0 km thick and is made up of basalts. Layer 2 is subdivided into an upper portion of extruded basalt, layer 2A, and a lower portion of basalt, massively intruded by dikes, layer 2B. Layer 3 is gabbroic, with an average thickness of about 5 km. White et al. (1992) provided an

26

accurate estimate of thickness of layer 2, $(2.11 \pm 0.55 \text{ km})$ and $(4.97 \pm 0.90 \text{ km})$ for layer 3. In the present work, the above simple 3-layered model by White et al. (1992) is used for modelling oceanic crust, of which the top sedimentary layer is considered non-magnetic.
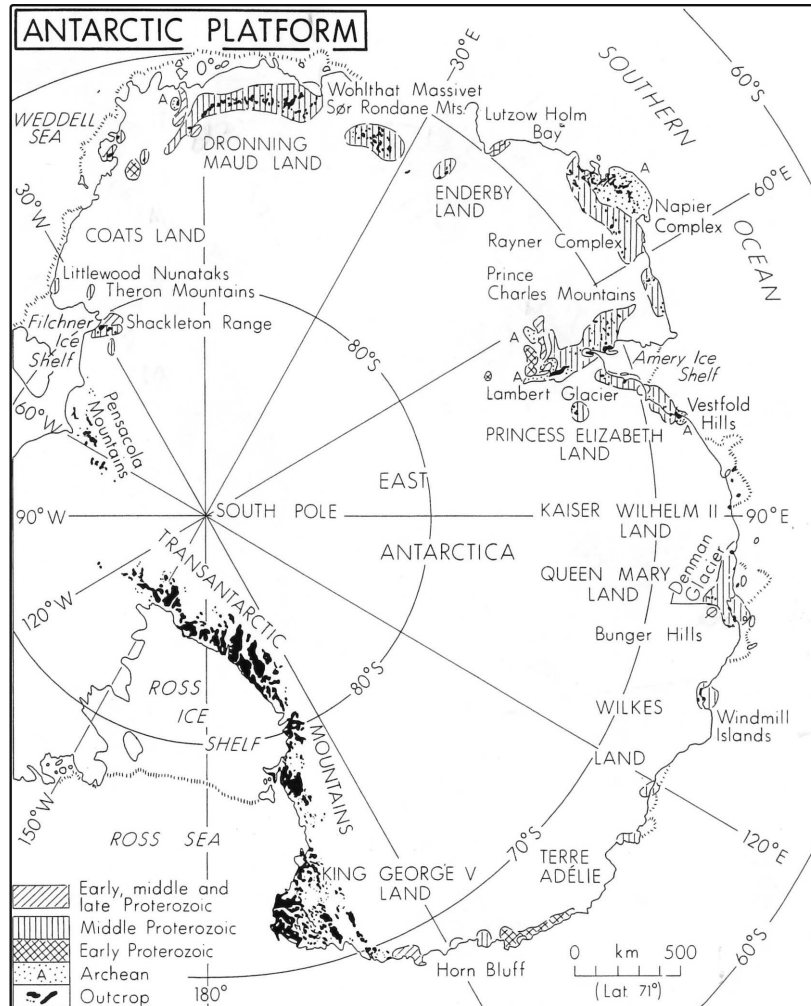
Fig. 2.10. Tectonic map of Antarctica craton (from Goodwin, 1991; after James and Tingey, 1983).

2.3.1 Oceanic plateaus

There are obviously anomalous features, showing up as strong oceanic magnetic anomalies which are caused by oceanic plateaus. Oceanic plateaus are the most puzzling of all the anomalies on the globe. The geology of the plateaus is poorly known and often there is a controversy about the origin of these plateaus, which cover almost 10% of the oceanic floor. Combining the information available from the Oceanic Deep Drilling Program (ODP), seismic constraints, and further literature (Carlson et al., 1980; Nur and Ben-Avraham, 1982), these anomalous features are represented in our model by 3 layers. layer (1)-basalts and dikes; layer (2)- gabbro; and layer (3) is largely inferred to be either

27

ophiolites or serpentinised ultramafic (peridotites) or olivine rich gabbro. The plateaus, especially in the southern hemisphere, are significant as they can reveal the dynamics of Gondwana dispersion (Antoine and Moyes, 1992; Reeves and de Wit, 2000). It is therefore important for us to model these features accurately, based on their structure. Again, induced magnetisation is considered as the only source causing the magnetic anomalies over the oceanic plateaus. This turns out to be sufficient even though most workers have included remanence in modelling oceanic plateaus.

2.4 Continental and Island arcs

Arc systems occur above active subduction zones and are subdivided into island-arcs and continental-margin arcs. Island-arcs are chains of volcanic islands formed on oceanic crust such as Mariana, Kermadec and Lesser Antilles arcs. Continental-margin arcs are produced above subduction zones that extend beneath continental margins, such as the Japan and Andean arcs. Some arcs, like the Aleutian Islands, continue from continental margins into oceanic crust. These regions are marked in dark blue colour in the world geological map (CGMW, 2000) in Figure (5.1a). However, there are other regions also marked in blue in the world map, which are the continuations of continents into the oceans and are called continental margin. These margins should have the same geology as on the continental area of the same region. They have, however, not been delineated from the arcs due to the immensity of work that this would require. For our model, the entire region marked in dark blue has therefore been assumed to have the same structure. Arcs are composed dominantly of young volcanic and plutonic rocks and derivative sediments. The upper crustal layer consists of granite and granodiorites while the lower crustal layer is dominantly of quartz diorite (Condie, 1989). This is largely inferred from seismic investigations. Maximum susceptibility values of (0.056 SI units) for the upper crust and (0.0127 SI) for the lower crust (following Hahn et al.,1984) are used in the present modelling.

2.5 Phanerozoic cover

The Mesozoic-Cenozoic orogenic belts are similar in size and geologic character to Paleozoic orogenic belts. However, the former are tectonically less stable than the latter. They are composed of a variety of rock types (Condie, 1989). The surface rock types are typical continental types consisting of sedimentary rocks, volcanic and plutonic rocks. In most of the regions of the earth, this younger crust overlies the Precambrian basement. The Precambrian basement can be either Archean or Proterozoic in age. In our modelling, the Phanerozoic units are assigned a susceptibility value of 0.01 SI, which is the average of typical young continental rock types. For the lower crust below this young cover an average susceptibility value (0.016 SI) for all the lower Proterozoic units is found to be adequate. However, the assumption of basement being lower Proterozoic in age below the Phanerozoic cover is changed in some regions of the world where the basement is known to be of older age.

2.6 Modelling

Our first interest is to generate an *initial model* based on the information of the rock types exposed, their magnetic susceptibility value and the known stratigraphy for that region. The input data required for modelling is discussed subsequently.

- World geological map by CGMW (2000).
- Tectonic map of the continents (Goodwin, 1991 and others)
- The global seismic model (3SMAC, CRUST2.1).
- Volume susceptibility value for all the known rock types (compiled from standard tables).

The World geological map shows the distribution of geology based on their ages. However, it does not provide any detail about the rock types known in a particular geological region. This gap is filled in with the information of rock types from the compilation of various tectonic maps. Tectonic maps restricted to Precambrian geology also inform about the geology of the basement overlain by the younger sediments based on the information of rock types exposed locally. The detailed Precambrian geology is discussed by Goodwin (1991, 1996) and is outlined briefly in Section 2.1. Combining the geological and tectonic maps helps us to formulate a first order *initial model*. The global seismic model is incorporated to use the estimated thickness of the crust for a region. Two popular global seismic models are 3SMAC (Nataf and Ricard, 1996) and CRUST2.1 which is a refined version of the earlier model CRUST5.1 by Mooney et al. (1998). Both models are used initially to ascertain their consistency as a good crustal model for all the regions of the world. For this it is essential to compute the crustal anomalies with each of the models and compare it with the corresponding observed one and select the best seismic model for a particular region and reject the other. This analysis is done and is explained in Chapter 4. The last of the input is the standard volume susceptibility chart taken from standard sources (Clark and Emmerson, 1991; Hunt et al., 1995). Each of these inputs is combined to formulate an *initial model*, which is discussed in the following subsections.

2.6.1 Vertically Integrated Susceptibility model

The crustal layer is thin in comparison to the altitude of satellites. Hence satellite magnetic maps are incapable of resolving the parameters viz., depth and susceptibility distribution individually, the two parameters responsible for the crustal anomalies. Hence only bulk susceptibilities, susceptibility multiplied by the thickness, at each point of the globe, can be inferred, irrespective of the position of the magnetic body in that vertical column. The sources to the magnetic anomalies would be the variation of these integrated susceptibilities across the globe which is termed 'Vertically Integrated Susceptibility' or (VIS).

The steps involved in deriving the initial VIS model are as follows:

1. Consider all the known rock types for a particular geological region as reported in the literature and perform a mathematical average using their maximum volume susceptibility value from the standard charts (Appendix I). The actual susceptibility of all the rock types is assumed to be some percentage of this maximum value, which is considered to be a constant for all the geological provinces of the world.

2. The next step is to generate the vertically integrated susceptibility (VIS) model. This requires the thickness information for each geological stratum within a vertical column and is generally known from the stratigraphy of that region as shown in Fig (2.11). The thickness is multiplied with the bulk susceptibility of that stratum. Integrating the susceptibility times thickness information for various layers in a vertical column, provides the VIS value for that region. Generally the stratigraphy information is not available for the lower crust, except for some regions that are exposed (Fountain and Salisbury, 1981). In regions devoid of any stratigraphical information, the bulk susceptibility is multiplied with the crustal thickness of the upper crust of the global seismic model.

3. An important parameter in the *initial model* is to consider the susceptibility value for the lower crust to be a factor multiplied with the bulk susceptibility of the upper crust. This factor is assumed following the difference in the iron oxide content in the average composition of the upper and the lower crust (Taylor and McLennan, 1985). The average composition of iron oxide in upper and lower crust of the earth is shown in Appendix II. This gives a factor of 1.2 for the Archeans and 1.6 for the post Archeans units.

4. Each such geological province is modelled following the steps 1 to 3 and each such VIS value is knit together to generate the global VIS model, which serves as an initial VIS model. Modelling is done on the GIS ArcInfo 8.1 craton.

The computation of the maximum susceptibility value for the Gabon craton is shown here as an example. The rock types exposed at different regions within this Archean craton, central Africa (Goodwin, 1991) along with the basement rock types are reproduced below and their maximum susceptibility value from the standard chart (Appendix I) is shown in brackets.

Rock types: granodiorite(0.062), migmatite gneiss(0.025), granitoids(0.05)

Bandas Belt: basalt(0.18), gneiss rhyolite(0.038), quartzite(0.0044), banded iron formations(0.25), granitoid gneiss(0.025), granodiorite(0.062)

Dekoa region: mafic volcanic rock(0.12), banded iron formations(0.25), granitoid gneiss (0.025)

Average susceptibility value = (0.062 + 0.025 + 0.05 + 0.18 + 0.038 + 0.0044 + 0.25 +
of Gabon craton   0.025 + 0.062 + 0.12 + 0.25 + 0.025) / 12
                                        = 0.0896

This susceptibility value is the average maximum susceptibility value for the Gabon craton. The value is assigned to the polygon representing Gabon craton on the world geological map. Such computations were done for all the Precambrian region of the

world and are compiled to derive the *initial model*. The parameters involved in generating the *initial model* are shown in the Appendix (III-XII). Table (2.1) describes the parameters common to all the continents.

2.6.2 Geographical Information System method

A Geographical Information System (GIS) is particularly convenient whenever more than one set of information for a particular region is to be combined. The utility of GIS method lies in its ability to perform various visual and statistical analyses between the different layers or stacks to compute new maps as desired. The present work exploits these capabilities of a GIS package to compute the global VIS model. The basic methodology is as follows:

The global seismic model is available as 2^0 X 2^0 grid and is taken as a layer in the GIS database. This grid map is considered as a raster image on the GIS craton. The bulk susceptibility value assigned to a geological region, as computed above in steps (1) in section (2.2.1), is a polygon on the geological world map (Fig. 2.11). This polygonal map is called a coverage map. All the polygons are assigned a susceptibility value similarly, and the world coverage map is converted to a grid map of 2^0 X 2^0. Based on the availability of geological stratigraphy of a region, susceptibility from the gridded world map is multiplied with the thickness from the seismic grid. The transformation from coverage to the grid format and the computation of VIS model is done using an algorithm developed for the purpose. The result is a global VIS model of resolution 2^0 X 2^0 as shown in Figure (2.12). This VIS grid map is then converted to an ascii formatted file on the GIS craton. This ascii formatted VIS model is fed as input in the modelling methods described in chapter (3), to compute the magnetic potential at the satellite altitude. Vertical component of the magnetic field is computed from spherical harmonic degrees 16-80 of the potential and compared with the corresponding vertical component of degrees 16-80 of the observed crustal field.
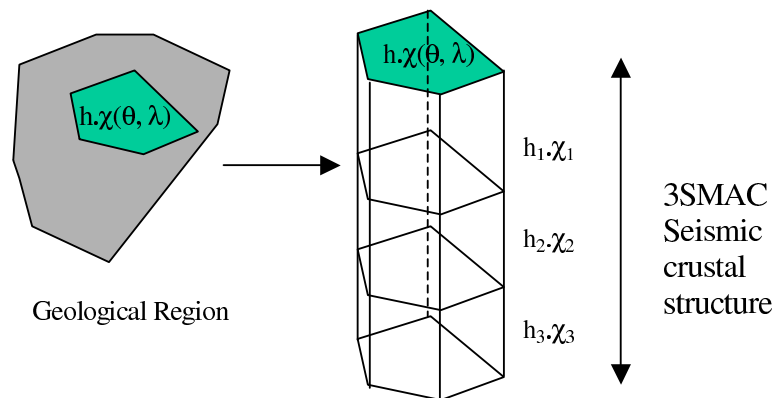
Fig. 2.11. Diagram shows a geological cross-section of a region, for which a VIS value is computed.

The parameters used in GIS based VIS modelling are shown in Table (2.1). The parameters used to represent a geological region are shown in Appendix (III-XI), one for each craton and Appendix (XII) for the oceans.

31

.ag : 0.55	: Percent of Maximum susceptibility value for Archean rocks
.wg : 0.55	: Percent of Maximum susceptibility value for post-Archean rocks
.cg : 0.55	: Percent of Maximum susceptibility value for Continental and Island arcs
.xa : 1.2	: The lower crust value is *xa* times the upper crust, if rock type is Archean
.xe : 1.6	: The lower crust value is *xe* times the upper crust, if rock type is Early Proterozoic.
.xm : 1.6	: The lower crust value is *xm* times the upper crust, if rock type is Mid Proterozoic.
.xl : 1.6	: The lower crust value is *xl* times the upper crust, if rock type is Lower Proterozoic.

Table 2.1. The parameters used for VIS modelling.
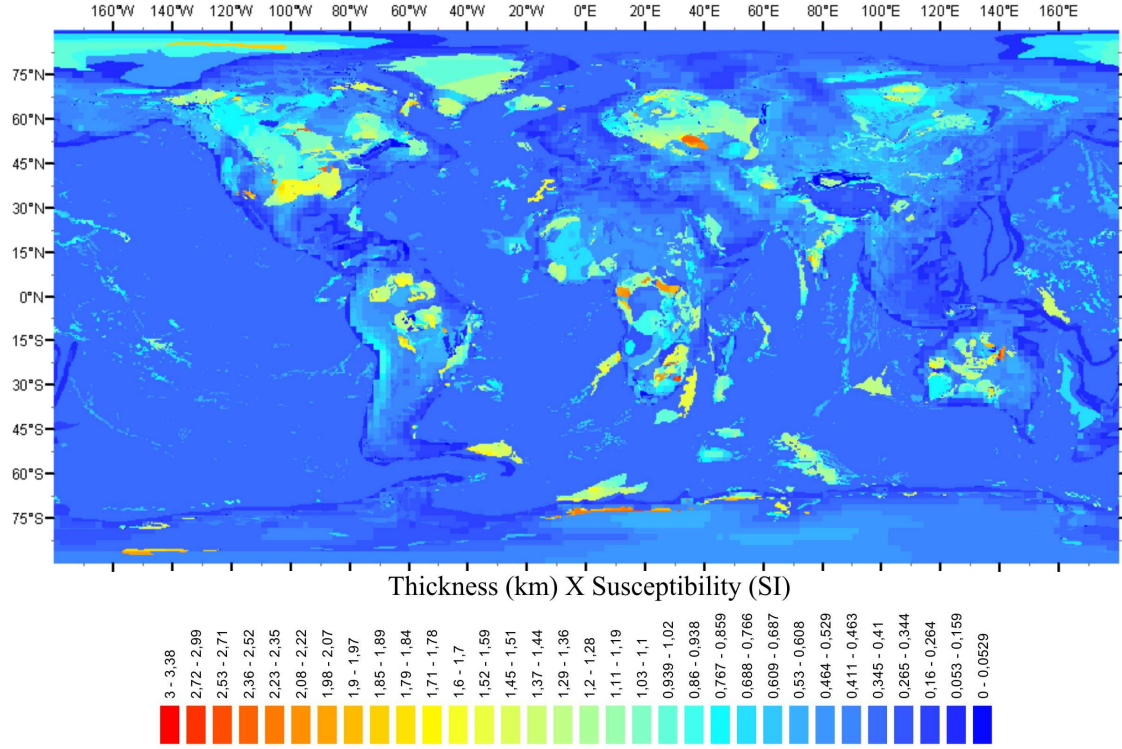
Fig. 2.12. *Initial model* Vertically Integrated Susceptibility (VIS) map of the world.

In our modelling procedure, it was desired to find a factor, which relates the maximum susceptibility to the actual susceptibility. This factor was to be assumed constant for all the geological regions and hence there was a need for a factor, which should be derived statistically. This factor is called *.ag*, *.wg* and *.cg* in Table 2.1.

To find the optimum factor, Gauss coefficients of *initial model* were computed for various factors: 0.0, 0.2, 0.3, 0.4, 0.5, 0.6, 0.7, 0.8, 1.0, times maximum susceptibility. These predicted Gauss coefficients are compared with the actual coefficients of the observed magnetic potential to compute the misfit. Misfit is computed using the following definition:

$$\text{Misfit} = \sum_{l=16}^{30} \frac{(l+1)}{(2l+1)l} \sum_{-l}^{+l} \left(g^m_{l\ observed} - g^m_{l\ predicted} \right)^2 \qquad (2.1)$$

Where, g_l^m are Gauss coefficients of the magnetic potential for the observed and the predicted magnetic potential. Misfit is computed using only degrees 16-30 which are particularly well predicted by the crustal model. The misfit curve is shown in Figure (2.13). The curve shows a pronounced minimum. The shaded region indicates the range of abscissa values for which the curve is almost flat. This range gives the admissible values that can be used in our modelling keeping the misfit minimal. We decided to take the value 0.55 for the parameters *.ag*, *.wg* and *.cg* in all the derivation of VIS models. This value is found to be the optimum value when modelling individual anomalies.

Fig. 2.13. The curve shows the admissible values for the factor of maximum susceptibility for a minimum misfit.
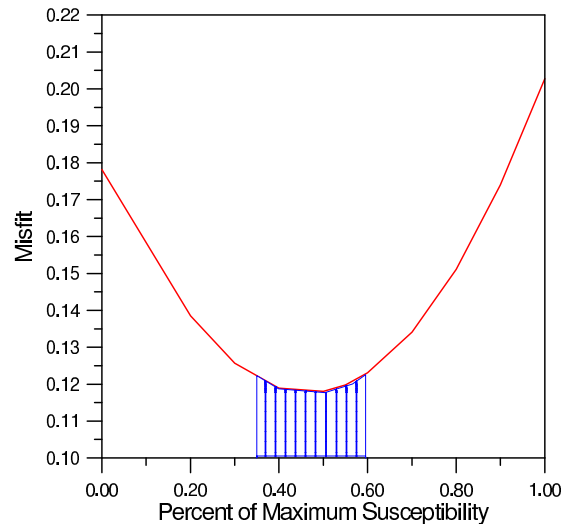
.xa, *.xe*, *.xm*, *.xl* parameters are values assumed based on the study of the percentage of iron oxides in the upper and the lower crust (Taylor and McLennan, 1985, Appendix II) of the Archean and post-Archean (Proterozoic and Phanerozoic) rocks, respectively.

2.7 Flowchart showing the present work

The entire sequence of methodology starting from the derivation of VIS model to the computation of anomaly maps is shown in Figure (2.14) in the form of a flow chart. The flow diagram shows that the modelling procedure starts with the non-satellite information viz., geology, crustal thickness, susceptibility values, and computation of the vertically integrated susceptibility. Following the modelling methods to be described in chapter 3, the *initial model* vertical field magnetic anomaly map for degrees 16-80 is computed. This predicted map is then compared with the CHAMP observed vertical field magnetic anomaly map. The mismatch of the anomalies in the two maps is again studied and the geology of the region is modified and the VIS value is recomputed. *First iteration* map is computed using this new VIS model following the same modelling steps. At present we have only modified the VIS model once for a *first iteration* model, but subsequent work in future would invoke further modifications of the model.

Known geology → modify → Improved geology

Vertically Integrated
Susceptibility (VIS)
model

Forward modelling

First Iteration
Vertically Integrated
Susceptibility model

Forward modelling

Observed CHAMP
magnetic anomaly map
deg 16-80

Initial model
magnetic anomaly map
deg 16-80

compare

First Iteration magnetic
anomaly map
deg 16-80
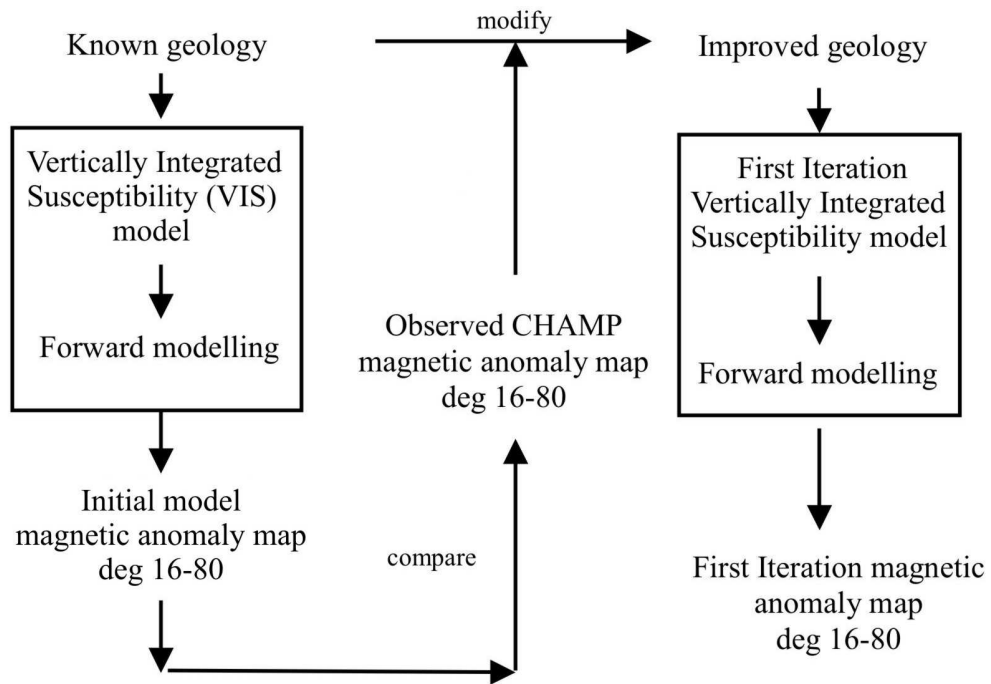
Fig. 2.14. Flowchart showing the modelling steps involved in the present work.

Chapter 3

Methodology

3.1 Introduction

The aim in the present work is to interpret the maps derived from satellite data and to infer geological information from these maps. The approach followed here is not that of direct inversion of satellite data sets which may be erroneous mainly because of the non-uniqueness of the inverse problem and the field models still retaining the uncorrected ionospheric and magnetospheric signals and also some part of main field. I start with an initial VIS model about the susceptibility and depth distribution on the Earth's surface based on present geology and crustal structures constrained by other geophysical data and perform the forward computation using spherical harmonic transforms to compute the initial magnetic anomaly field. The next step is to locate specific regions on the map where the anomaly patterns or amplitude of the initial and the observed map are in disagreement. The next iteration would require modification in parameters value for the lower crust or even the shape of a geological unit to arrive at the *first iteration* model. This iteration is used to infer geological information for the region studied in detail.

The entire set of modelling steps described above requires first computing the magnetic potential at the satellite altitude for a given global initial VIS model and subsequently Gauss coefficients for this potential are derived using spherical harmonic expansion of the potential. The next step involves predicting the vertical component of the crustal field anomaly for degrees 16-80 using the Gauss coefficients derived above. For modelling, two distinct approaches have been followed. The first approach assumes a distribution of equivalent dipoles for grid cells on the Earth's surface and is called the 'Equivalent Dipole Method' (Langel & Hinze, 1998). The second approach follow the methodology to arrive at the potential derived by Nolte & Siebert (1987) and is referred to in the following as Nolte-Siebert method. Both the approaches yield the Gauss coefficients of the crustal field potential. The details of the above mentioned steps and the approaches are explained below.

3.2 Equivalent dipole method

The equivalent dipole method computes the crustal magnetic field of the earth from the crustal and geomagnetic main field data. The assumptions followed for the derivation of the necessary equations are as follows:

- Earth topography is neglected, while Earth ellipticity is taken into account.
- Induced magnetisation is considered as the only source for the anomalies.

The crust here is characterized by an vertically integrated susceptibility that depends upon the angular coordinates of the spherical surface, defined on a local geographic coordinate which coincide with the spherical coordinate system, by radius r, colatitude θ and longitude ϕ.

Considering a volume element $d\tau'$ of magnetizable material located at point $\vec{r}' = (r', \theta', \phi')$ within the earth's crust. The material attains an induced magnetisation due to the geomagnetic main field $\vec{B}$. The potential due to this magnetised volume element $d\tau'$ at a fixed external point $\vec{r} = (r, \theta, \phi)$ is defined as dipole potential dV and is written as

$$dV(\vec{r}, \vec{r}') = \frac{\mu_0}{4\pi} d\vec{m}(\vec{r}') \cdot \nabla' \frac{1}{R} \tag{3.1}$$

where μ_0 is the permeability of the vacuum, $R = |\vec{r} - \vec{r}'|$ and the prime with the Nabla operator denotes differentiation with respect to source coordinates. $d\vec{m}(\vec{r}')$ is the dipole moment and is the product of $d\tau'$ with the magnetisation $\vec{M}$. The situation is shown in Figure (3.1).
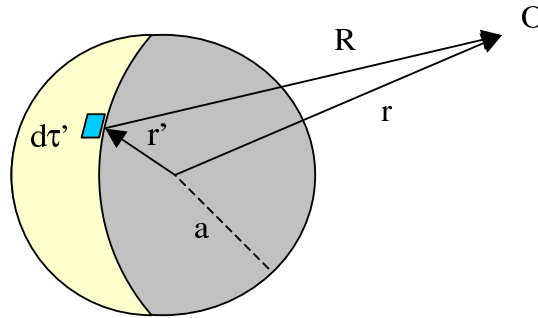
Fig. 3.1. Schematic diagram showing an elemental dipole moment producing a potential at point O.

As the crustal thickness d is assumed negligible, the integrated susceptibility of the crust can be defined as

$$\tilde{\chi}(\theta', \phi') = \lim_{\substack{d \to 0 \\ \chi \to \infty}} \int_{a-d}^{a} \chi(r') dr' \tag{3.2}$$

where $\tilde{\chi}(\theta',\phi')$ is the magnetic susceptibility assumed to be a scalar quantity and a is the Earth's radius. The susceptibility is further assumed to be nonzero only in the region between Curie isotherm and the Earth's surface. Since the thickness of the magnetised layer is small compared with the altitude, the three-dimensional (3D) susceptibility distribution can be represented by the vertically integrated susceptibility of the thin shell. Thus we can compute vertically integrated magnetisation or susceptibility defined as the thickness of the magnetised crust multiplied with the average value of the susceptibility, at every point on the Earth's surface.
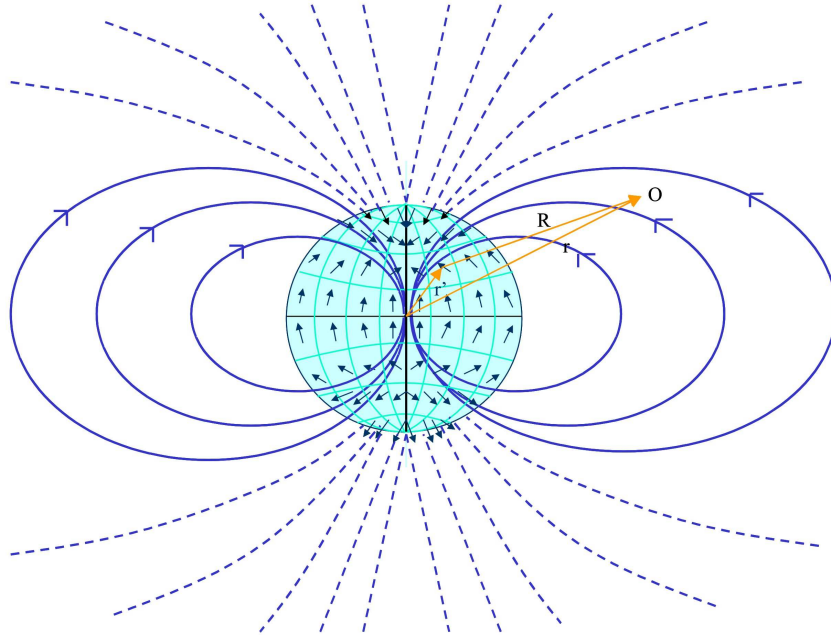
Fig. 3.2. The distribution of induced dipoles on the surface of Earth in an inducing dipole field. Each dipole is aligned with the direction of the inducing field.

Considering a global crustal model it is desirable to work in spherical coordinates. Dividing the spherical earth into 15' × 15' grid cells, integrated susceptibility, $\tilde{\chi}(\theta',\phi')$ can be computed in every cell by assuming a magnetic depth multiplied with the average susceptibility in that column. The situation is shown in Figure (3.2). Each cell is represented by a single dipole whose contribution to the magnetic potential can be written in spherical coordinates as

$$dV(\vec{r},\vec{r}') = \frac{\mu_0}{4\pi} \frac{d\vec{m}(\theta',\phi') \cdot \vec{R}}{|R|^3} \qquad (3.3)$$

where $d\vec{m}(\theta',\phi') = \tilde{M}(\theta',\phi')ds' = \frac{1}{\mu_0}\tilde{\chi}(\theta',\phi')\vec{B}(\vec{r}')ds'.$

37

$$dV(\vec{r},\vec{r}\,') = \frac{1}{4\pi}\,\widetilde{\chi}(\theta',\phi')\frac{\vec{B}(\vec{r}\,')\cdot\vec{R}}{|R|^3}\,ds' \tag{3.4}$$

where $ds' = \sin\theta'\, s_0$ and (θ',ϕ') are colatitude and longitude of the source dipole. Each pair of points (θ',ϕ') is defined at the centre of the grid cell. The area of the grid cell varies according to $\sin\theta'\, s_0$, where s_0 is the area of the cell at the equator and it decreases down to zero at the poles. Each dipole represents an area of ds', on the Earth's surface. Each $d\vec{m}(\theta',\phi')$ is assumed to have the direction of the present-day ambient field. The assumption that $d\vec{m}(\theta',\phi')$ is oriented along the ambient field ignores the possibility of remanent magnetisation in any other direction. Potential field is calculated at every point on a spherical grid at an altitude of 400 km from the surface of the Earth, by summing the contribution of each dipole. This potential is then expanded into a spherical harmonics to degree 80 to get the Gauss coefficients of the potential. The program performing the above steps is defined in the following.

A program in C language is developed to compute the potential and expand it into spherical harmonics to find Gauss coefficients of the potential for degree 1-80. The program takes the vertically integrated susceptibility for the entire Earth's surface as the input as a $15' \times 15'$ grid. This input is generated with the help of GIS package Arc/Info 8.1. Each cell represents a single dipole and the direction of the dipole is aligned with the direction of the inducing main field. It is to be noted that the grid structure described above makes the data structure sparse at the equator and very closely spaced at the poles. Thus, it would be appropriate to redesign the grid structure so as to use grid cells having same effective area on the Earth's surface. This in turn reduces the number of grid cells at the poles. Each cell represents an equivalent dipole, representing an area of $2^0 \times 2^0$ called internal grid cells. The program uses an algorithm to compute spherical harmonic transformation of the potential field value at only Gauss-Legendre (G-L) positions. G-L positions are unequally spaced points on the latitude of the spherical shell where the field value is to be calculated. This means that the G-L positions at a particular latitude have more number of points at the equator than at the poles. Potential is computed for each dipole on the internal grid cells at every point on the G-L position at an altitude of 400 km. Total potential is calculated at every point of the G-L spherical shell as a summation of potential contribution from all the dipoles. This total potential is then expanded using spherical harmonic transform to get the Gauss coefficients for degrees 1-80. Subsequently, the vertical component of the crustal anomaly field is computed from these Gauss coefficients.

3.3 Nolte-Siebert method

The work of Nolte and Siebert (1987) introduced for the first time an analytical relation between the spherical harmonic coefficients of susceptibility and the potential of the inducing field. Unlike the equivalent dipole method, which works in space domain, Nolte-Siebert method works in wavenumber domain. The pertinent relations to solve the

38

forward problem of the crustal field were originally derived by one of the authors, Siebert, and was further extended and applied to a crustal model field by his co-worker Nolte (1985). The method developed by Nolte and Siebert (1987) computes the Gauss coefficients of the potential of the crustal field of the Earth. The assumptions followed for the derivation of the necessary equations have been already defined in the previous section.

The integrated susceptibility of the crust is defined by the Equation (3.2). If the inducing field is replaced by the gradient of the scalar potential V outside the Earth's core, then the dipole moment becomes

$$d\vec{m}(\vec{r}') = \vec{M}(\vec{r}')d\tau' = -\frac{1}{\mu_0}\chi(\vec{r}')\nabla'V(\vec{r}')d\tau' \qquad (3.5)$$

The VIS can be expanded into spherical surface harmonics to degree n as

$$\tilde{\chi}(\theta',\phi') = \sum_{n=1}^{\infty}\sum_{m=0}^{n}\left(p_n^m\cos m\phi' + q_n^m\sin m\phi'\right)P_n^m(\cos\theta') \qquad (3.6)$$

The term for degree n=0 has not been taken into account as it represents a constant distribution of the integrated susceptibility over the entire surface of the Earth, which would not contribute to any measurable magnetic field outside the spherical Earth (Runcorn, 1975).

The potential of the geomagnetic main field is expanded into a series of spherical harmonics with reference radius a

$$V_c(\vec{r}') = a\sum_{n=1}^{\infty}\left(\frac{a}{r'}\right)^{n+1}Y_n(\theta',\phi') \qquad (3.7)$$

where c stands for the core, and Y_n represents sum over one or more elementary surface harmonics of the same degree n but with orders varying between $m=0$ and $m=n$.

$$Y_n = \sum_{m=0}^{n}\left(g_n^m\cos m\phi' + h_n^m\sin m\phi'\right)P_n^m(\theta') \qquad (3.8)$$

Quasi-normalization according to Schmidt is used throughout for Legendre's associated functions P_n^m. Gauss coefficients g_n^m and h_n^m are given by a main field model. For the dipole inducing geomagnetic field ($n=1$), the terms in equation (3.8) can be written as

$$Y_1(\theta',\phi') = g_1^0 P_1(\theta') + \left(g_1^1\cos\phi' + h_1^1\sin\phi'\right)P_1^1(\theta') \qquad (3.9)$$

39

The potential can be derived by allowing full expansions of the main field and the susceptibility and by combining all the equations [4-27] (Nolte and Siebert, 1987) to arrive at Eqn. [29] (Nolte and Siebert, 1987) for the expression of potential $V(\vec{r})$. If further G_N^M and H_N^M are the spherical harmonic expansion coefficients of the crustal potential $V(\vec{r})$, it can be written as

$$V(\vec{r}) = a \sum_{N=1}^{\infty} \sum_{M=0}^{N} \left(\frac{a}{r}\right)^{N+1} \left(G_N^M \cos M\phi + H_N^M \sin M\phi\right) P_N^M(\theta) \tag{3.10}$$

and can be compared with coefficients of eqn [38] (Nolte and Siebert, 1987) to get the following relation for the coefficients for crustal potential G_N^M and H_N^M for the axial and non-axial dipolar inducing field, respectively shown in eqn (3.11) and (3.12),

$$\begin{Bmatrix} \left(G_N^M\right)_{10} \\ \left(H_N^M\right)_{10} \end{Bmatrix} = \frac{1}{2a(2N+1)} \left[\frac{N-1}{2N-1} \left[g_{10}\sqrt{(N-M)(N+M)}\, p_{N-1,M}\right] + \frac{3N}{2N+3}\left[g_{10}\sqrt{(N-M+1)(N+M+1)}\, p_{N+1,M}\right] \right]$$

$$\tag{3.11}$$

$$\begin{Bmatrix} \left(G_N^M\right)_{11} \\ \left(H_N^M\right)_{11} \end{Bmatrix} = \frac{\sqrt{g_{11}^2 + h_{11}^2}}{2a(2N+1)} \left[\frac{N-1}{2N-1} \left\{ \sqrt{\frac{2-\delta_{M1}}{2}}\sqrt{(N+M-1)(N+M)}\begin{Bmatrix} p_{N-1,M-1}\cos\varepsilon_{11} - q_{N-1,M-1}\sin\varepsilon_{11} \\ q_{N-1,M-1}\cos\varepsilon_{11} + p_{N-1,M-1}\sin\varepsilon_{11} \end{Bmatrix} \right. \right.$$

$$\left. - \sqrt{\frac{2}{2-\delta_{M0}}}\sqrt{(N-M-1)(N-M)}\begin{Bmatrix} p_{N-1,M+1}\cos\varepsilon_{11} + q_{N-1,M+1}\sin\varepsilon_{11} \\ q_{N-1,M+1}\cos\varepsilon_{11} - p_{N-1,M+1}\sin\varepsilon_{11} \end{Bmatrix} \right\}$$

$$- \frac{3N}{2N+3} \left\{ \sqrt{\frac{2-\delta_{M1}}{2}}\sqrt{(N-M-1)(N-M+2)}\begin{Bmatrix} p_{N+1,M-1}\cos\varepsilon_{11} - q_{N+1,M-1}\sin\varepsilon_{11} \\ q_{N+1,M-1}\cos\varepsilon_{11} + p_{N+1,M-1}\sin\varepsilon_{11} \end{Bmatrix} \right.$$

$$\left. \left. - \sqrt{\frac{2}{2-\delta_{M0}}}\sqrt{(N+M-1)(N+M+2)}\begin{Bmatrix} p_{N+1,M+1}\cos\varepsilon_{11} + q_{N+1,M+1}\sin\varepsilon_{11} \\ q_{N+1,M+1}\cos\varepsilon_{11} - p_{N+1,M+1}\sin\varepsilon_{11} \end{Bmatrix} \right\} \right]$$

$$\tag{3.12}$$

where $p_{N+1,M-1} = 0$ when M=0 and $p_{N-1,M+1} = 0$ when M≥N-1 and the symbol δ_{MN} is the Kronecker delta. Nolte (1985) derived more complicated analytical expressions for coefficients of the crustal potential for the inducing quadrupole and octupole terms of the geomagnetic main field. We have used all the expressions derived for terms n=1,2,3 of geomagnetic main field, to compute the coefficient of potential on an external spherical grid for an integrated susceptibility distribution on the Earth's surface. Interested readers should refer to the work by Nolte, (1985) for a complete set of expressions used in the present analysis. The pertinent equations are used to compute the Gauss coefficients of the lithospheric field potential.

A program based on the equations derived by Nolte and Siebert (1987) is developed to compute the spherical harmonic coefficients (VIS) of the potential. The program takes the vertically integrated susceptibility global model as the input. Spherical harmonic expansion of the VIS is performed to obtain the coefficients p_n^m and q_n^m. Next, main field is considered starting with the dipole terms first, followed by the terms for quadrupole

and octupole terms as the only inducing fields. Each of these terms is taken separately and then together to study the effects of induction to the magnetised layer. Gauss coefficients of the potential are computed using all the terms of inducing main field. The vertical component of the crustal anomaly field is computed from the Gauss coefficients in the same way as for the equivalent dipole method.

3.4 Comparison of the two methods

In the above two sections two forward modelling methods were described. The methods followed two different approaches to arrive at the Gauss coefficients of the potential. After implementing these two approaches in the form of computer programs, these programs were tested for their accuracy and speed.

In the process of testing, a simple VIS model was considered as input because the initial crustal model was built only at a later stage. This VIS model was derived by multiplying the ETOPO map with the 3SMAC seismic model. ETOPO map is an elevation map produced by NGDC (http://www.ngdc.noaa.gov/mgg/global/seltopo.html). This elevation map was separated in two parts as continents and oceans. Continents were denoted with fixed susceptibility value of 0.4 and oceans with 0.2. These values were then multiplied with 3SMAC seismic crustal thickness to derive the VIS model. This VIS model was now fed as input, which was in the form of $2^0 \, X \, 2^0$ grid, in the two programs developed above. The Gauss coefficients for the potential were derived using the above two methods. Producing the vertical field anomaly maps and comparing the Gauss coefficients derived by the two programs did not reveal all the details and hence a correlation analysis was done using these coefficients. The correlation analysis was done following the definition by (Arkani-Hamed et al., 1994)

$$K(n) = \frac{\sum_{m=0}^{n}\left(G_n^m G_n^m{}' + H_n^m H_n^m{}'\right)}{\left[\sum_{m=0}^{n}\left(G_n^m G_n^m + H_n^m H_n^m\right)\sum_{m=0}^{n}\left(G_n^m{}' G_n^m{}' + H_n^m{}' H_n^m{}'\right)\right]^{1/2}} \qquad (3.13)$$

The coefficients G_n^m and H_n^m are the Gauss coefficients for the potential derived after Nolte-Siebert method and $G_n^m{}'$ and $H_n^m{}'$ for the equivalent dipole method. The correlation coefficient curve is shown in Figure (3.3). The figure showed a very good correlation between the two sets of coefficients. This statistical analysis verified that nearly the same coefficients were produced by these methods. It is to be noted that the Nolte-Siebert method uses only degree 1-3 of the inducing main field while the equivalent dipole method uses all the degrees of the main field and hence, arguably the equivalent dipole method is more accurate than the Nolte-Siebert method. Later, the speed of the algorithms was also analysed. To produce the Gauss coefficients using the above programs, the equivalent dipole method took 8 hours while the Nolte-Siebert method took only 1 minute on a Dell Workstation (2.6 GHz Pentium 4) machine. On comparing

41

the global magnetic anomaly maps produced by both the methods, a difference of $1.5 - 2$ nT is observed. Over the poles, the amplitude of the anomaly computed using dipole method is less than computed using Nolte-Siebert method while it is greater over the equator. As the average magnetic crustal anomaly is approximately $2 - 4$ nT, the difference in the two maps as mentioned above may be significant. Thus, even though all the initial computations were done using the Nolte-Siebert method, the final maps were prepared using the more accurate equivalent dipole method.

Fig. 3.3. Correlation coefficients between the Gauss coefficients derived using Nolte-Siebert and equivalent dipole method.
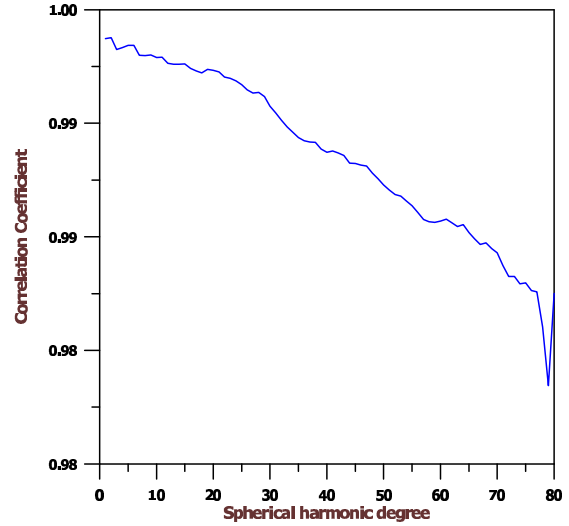
3.5 Computing vertical field anomaly

The spherical harmonic expansion of the magnetic crustal potential computed in the above sections can be written as

$$V(r,\theta,\phi) = a \sum_{n=1}^{n} \sum_{m=-n}^{n} \left(\frac{a}{r}\right)^{n+1} g_n^m Y_n^m(\theta,\phi) \tag{3.14}$$

where a is the mean earth radius (6371.2 km), and

$$Y_n^m(\theta,\phi) = \cos(m\phi) P_n^m(\cos\theta) \tag{3.15a}$$

$$Y_n^{-m}(\theta,\phi) = \sin(m\phi) P_n^m(\cos\theta) \tag{3.15b}$$

and g_n^m are the Gauss coefficients which are known from the above two methods, n is the degree and m is the order of the spherical harmonic expansion of the potential. The crustal magnetic field $\vec{B}$ is related to the potential by the expression

$$\vec{B}(r,\theta,\phi) = -\vec{\nabla} V(r,\theta,\phi) \tag{3.16}$$

42

then taking the gradients with respect to r, θ and ϕ, we get the three components of the magnetic field as

$$B_r(r,\theta,\phi) = -\frac{\partial V}{\partial r} = \sum_{n=1}^{n} \sum_{m=-n}^{n} (n+1)\left(\frac{a}{r}\right)^{n+2} g_n^m Y_n^m(\theta,\phi)$$ (3.17)

$$B_\theta(r,\theta,\phi) = -\frac{1}{r}\frac{\partial V}{\partial \theta} = -\sum_{n=1}^{n} \sum_{m=-n}^{n} \left(\frac{a}{r}\right)^{n+2} g_n^m \cos(m\phi)\frac{\partial P_n^m(\cos\theta)}{\partial \theta}$$ (3.18)

$$B_\phi(r,\theta,\phi) = -\frac{1}{r\sin\theta}\frac{\partial V}{\partial \phi} = \frac{1}{\sin\theta}\sum_{n=1}^{n} \sum_{m=-n}^{n} m\left(\frac{a}{r}\right)^{n+2} g_n^m Y_n^{-m}(\theta,\phi)$$ (3.19)

The z component of the crustal magnetic field is further related to the radial component of the crustal magnetic field as

$$B_z(r,\theta,\phi) = -B_r(r,\theta,\phi) = \frac{\partial V}{\partial r} = -\sum_{n=1}^{n} \sum_{m=-n}^{n} (n+1)\left(\frac{a}{r}\right)^{n+2} g_n^m Y_n^m(\theta,\phi)$$ (3.20)

Using the above equation and taking the Gauss coefficients derived above for the potential, we can get the z-component of the crustal magnetic anomaly field. The scalar anomaly field can be computed by taking the component of the residual field in the unit vector direction of the inducing main field.

Both the scalar anomaly and vertical field anomaly map is computed using the above methodology and is compared with the observed CHAMP magnetic field anomaly map. We have chosen to compare only the vertical component map for predicted and observed anomaly map. Unlike the scalar anomaly map, the vertical component on a spherical shell completely determines the magnetic potential of the field.

An algorithm is developed to compute the z component of the crustal anomaly field. The program takes the Gauss coefficients as the input and following the equations derived above in this section computes the vertical component (B_z). To compute the vertical field anomaly of the VIS model, the magnetic potential is computed and spherical harmonic degrees 1-15 are set to zero because this long wavelength crustal field is masked by the main field and is not observable. Finally, only spherical harmonic degrees 16-80 of the model field are compared with the corresponding degrees 16-80 of the observed crustal field.

Chapter 4

Vertical Field Anomaly Map

4.1 Comparison of observed and *initial model* vertical field anomaly map

The global Vertically Integrated Susceptibility (VIS) model derived in chapter 2 is used to compute the vertical field anomaly map or the z-component map following the modelling procedure described in chapter 3. The spherical harmonic degrees 1-15 of the vertical field anomaly map are set to zero because this long wavelength crustal field is masked by the main field and is not observable. Hence, only spherical harmonic degrees 16-80 of the model field are computed and are compared with the corresponding degrees 16-80 of the observed crustal field. The results are discussed for all the major anomalies observed over the continents and oceanic regions in the following subsections.

In Chapter 2, when the two global seismic crustal models were introduced it was mentioned that only one of them would be selected for our modelling work. To start with, both 3SMAC and CRUST2.1 crustal model were considered for deriving VIS model. The vertical field anomaly map produced using the VIS models derived using both the crustal models did not vary much over the oceans but over the continents there was some mismatch. Significant disagreement of the magnetic anomaly patterns was seen over Africa, Greenland, northern Siberia, eastern Tibetan plateau, South America and most of eastern region of North American craton. Except over the North American craton, where the magnetic anomaly map produced using the CRUST2.1 matched more closely with the observed anomaly map, for rest of the regions mentioned above, 3SMAC model produced a better fit with the observed. Thus, CRUST2.1 model is used for modelling the North American craton and 3SMAC model for the rest of the world including the oceans. There are obvious gaps in the seismic models of both 3SMAC and CRUST2.1 in the African region, Greenland and South America. So, the new seismic results for Greenland (Dahl-Jensen et.al, 2003) and for Guyana shield, South America (Schmitz et al., 2002) is used in the derivation of initial VIS model, instead of 3SMAC or CRUST2.1 model for these regions. For Africa, however, 3SMAC seismic model is retained. This is because 3SAMC model is derived using both seismological and nonseismological constraints such as chemical composition, heat flow, hotspot distribution, from which estimates of seismic velocities and the density in each layer is made. While the CRUST2.1 model is only a minor improvement over its predecessor CRUST5.1, and includes only the compilation of seismic data across the globe and the gaps were filled by applying a statistical average for various geological settings such as Precambrian shields, extended

continental crust and passive margins. Thus, the better constrain of 3SMAC model using nonseismic data and due to a better fit of the predicted vertical field anomaly map with the observed map, 3SMAC seismic model is used for modelling most part of the world, except North America, Greenland and Guyana shield of South America, where seismic models as stated above has been used.

The CHAMP observed vertical field anomaly map is shown in Figure (4.1) and the corresponding global vertical field anomaly map predicted using the initial VIS model is shown in Figure (4.2). The two maps are compared visually. On comparison it is apparent that there are anomalies over the regions where the *initial model* and observed maps match well while there are anomaly patterns that do not match. Over some regions the predicted anomalies display higher amplitude than the observations. The effect of continent-ocean boundary is also not apparent in the computed map and needs further discussion. There are East-West trending anomaly patterns over the oceanic region in the observed map, which are absent in the predicted map, especially over the Pacific Ocean. The anomaly patterns related to oceanic rises and plateaus agree well, especially those located south east of African continent, while only partially in the regions south west of it. This suggests that the seismic thickness of most of these plateaus needs to be redefined. A comparison of observed and *initial model* maps is now being described for all the continents and oceanic regions.

4.2 Examples of predicted anomalies in agreement and in disagreement with observed anomaly map

4.2.1 Cathaysian craton

The Cathaysian craton has been studied by others using the crustal field observed by Magsat data. Total field anomaly maps were derived and the sources of anomalies were associated with the corresponding geological units (Achache et al., 1987; Arkani-Hamed et al., 1988). Similar results have been reported for the Tibetan plateau for vertical field anomaly maps by Arkani-Hamed et al. (1988), Rajaram and Langel (1992), Hamoudi et al. (1995) and very recently by Alsdorf and Nelson (1999). The Indian craton has also been studied extensively using the vertical field (Mishra, 1984; Agarwal et al., 1986; Rajaram and Langel, 1992) and total field anomaly maps (Negi et al., 1986; Singh and Rajaram, 1990) using Magsat data.

The Cathaysian craton exhibits diverse geological units including the Himalayan fold belt and is modeled here using the susceptibility distribution for each of these units (Appendix III) following the modelling procedure described in Chapter 2. The tectonic map for the Cathaysian craton is shown in Figure (2.1) and for the Indian craton in Figure (2.8). The *initial model* vertical field anomaly map is computed at the satellite altitude of 400 km and is compared with the corresponding observed vertical field anomaly map.
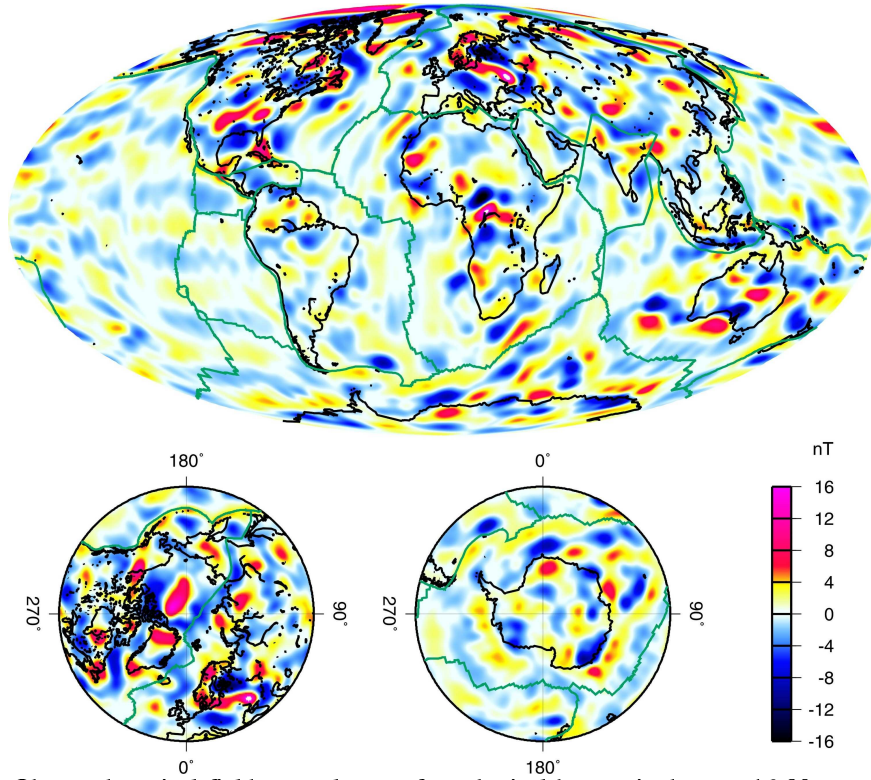
Fig. 4.1. Observed vertical field anomaly map for spherical harmonic degrees 16-80 at an altitude of 400 km.
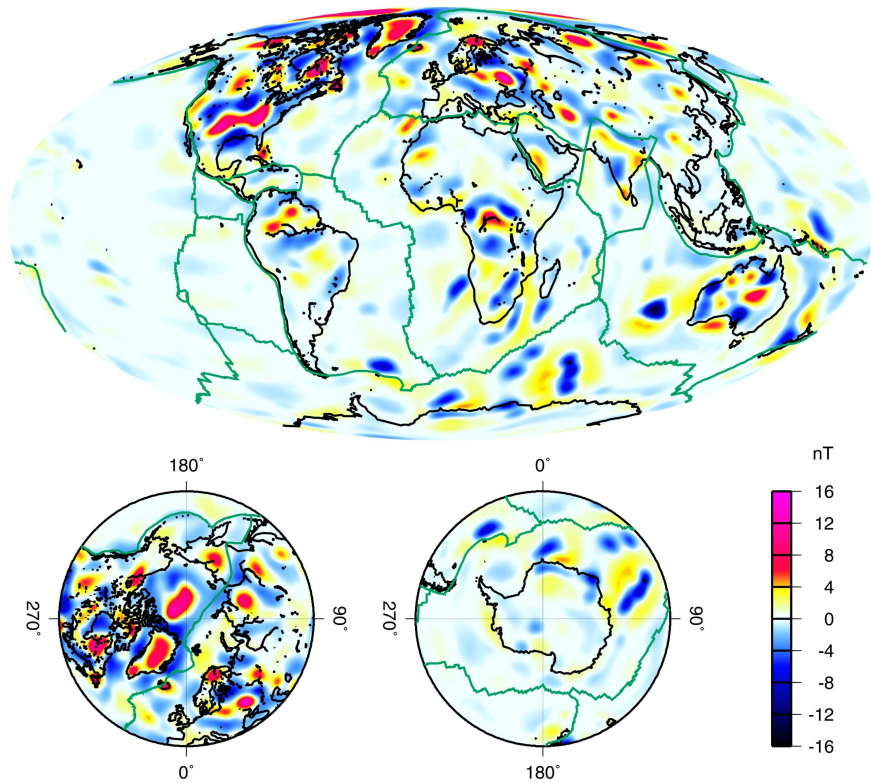
Fig. 4.2. Predicted vertical field anomaly map (*initial model*) for spherical harmonic degrees 16-80 at an altitude of 400 km.

The observed vertical field anomaly map for the Cathaysian craton is shown in Figure (4.3a). A large positive anomaly is observed over Tarim basin, (1), that not only is observed over the Archean rocks exposed at the core of the basin but also extends over the surrounding Proterozoic rocks overlain by Mesozoic-Cenozoic cover. Further towards east, over the Yangtze craton, lies a positive anomaly of moderate amplitude attributed to the Sichuan massif, (2). A large positive anomaly can also be seen over the largely buried Songliao microcontinent, (3), north of the Korean peninsula. The most interesting of all the anomalies is the strong negative observed over the entire stretch of the Himalayan fold belt and the Tibetan plateau, (4), suggesting a non-magnetic character of the lower crust in the region. Further, located southeast of the Caspian sea is a circular shaped anomaly overlying the Turkmenistan shield, (5).
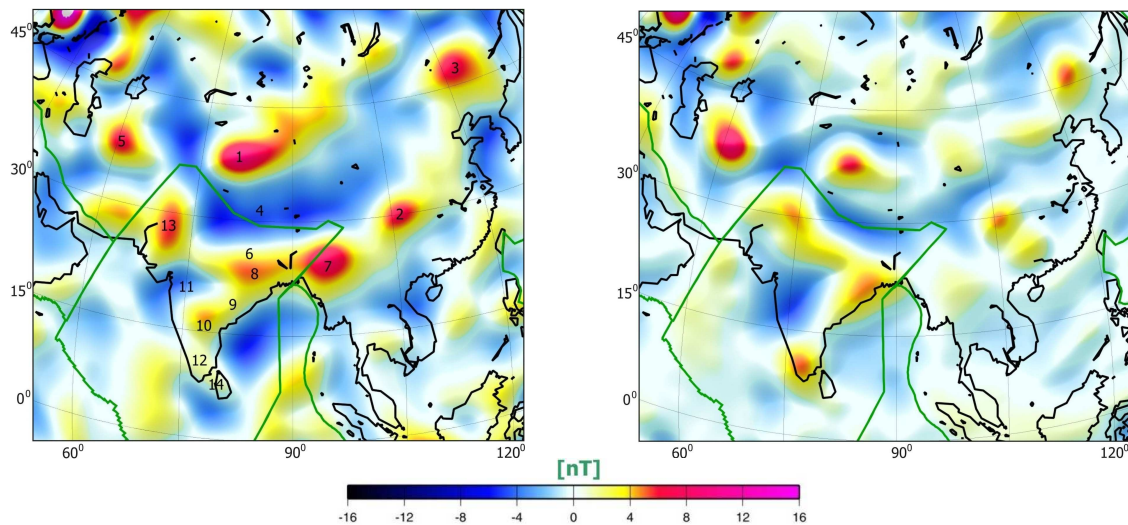
Fig. 4.3a. Observed vertical field anomaly map for spherical harmonic degrees 16-80 at an altitude of 400 km for the Cathaysian craton and Indian subcontinent.

Fig. 4.3b. *Initial model* vertical field anomaly map for spherical harmonic degrees 16-80 at an altitude of 400 km for the Cathaysian craton and Indian subcontinent.

South of the Cathaysian craton lies the Indian subcontinent. A positive anomaly of moderate intensity is observed all along the Indo-Gangetic basin, (6), south of Himalayan fold belt. These anomaly patterns terminate at the North Eastern border of India, in Myanmar, (7), where a large circular anomaly is seen. A positive anomaly is also observed over the Singhbhum craton, (8), east of Bangladesh. Further south, within the subcontinent, a stretched out positive anomaly of moderate intensity follows the eastern border of Peninsular India, (9) which terminates over the Eastern Dharwar craton, (10). In the west, a negative anomaly over the Narmada-Son basin, (11), is observed. Southern India peninsular gneiss (12), exhibits a weak negative anomaly at satellite altitude. An anomaly aligned north-south is also observed extending from the western border of Gujarat, India to central Pakistan, (13). A very weak positive anomaly is also seen over the Proterozoic provinces of SriLanka, (14).

The *initial model* vertical component anomaly map for Cathaysian-Indian region is shown in Figure (4.3b). The large anomaly over the Tarim basin agrees well only over the central region where the Archean rocks are exposed while the rest of the basin,

assumed as essentially non-magnetic, does not agree with the observations. It is important to note that Archean rocks, exposed only at the core of the basin, fail to explain an anomaly of such large amplitude and shape. Rather, it appears that the basement Archean rocks extend further below the Proterozoic province of the Tarim microcontinent and the observed anomaly shape indicates the bulk effect of such a mafic basement structure. This needs further investigation to find the source of the missing anomaly and is discussed in Chapter 5. A positive anomaly seen over largely buried Songliao microcontinent, is reproduced only partially in the *initial model*. The westward extension of the predicted anomaly is completely missing. This suggests the presence of a still larger buried microcontinent. A moderate positive anomaly predicted for the Sichuan massif of the Yangtze craton relates well with the observed one; however, a part of the amplitude of the anomaly is yet unaccounted for. Over the Turkmenistan shield, located southeast of the Caspian sea, the predicted and observed anomaly maps are in complete agreement.

The predicted strong negative anomaly region over the Himalayan fold belt and the Tibetan plateau agrees well with the extension of the measured anomaly. However, a part of the anomaly is not reproduced. It is to be noted that the susceptibility value for the rock types exposed in the Himalayan fold belts (Appendix III) is already very low yet the observed anomaly warrants still lower susceptibility value for the region. Another possible reason for such low magnetisation could be a high heat flow in the region and the lower crust could be almost non-magnetic. As the heat flow models have not been a part of our modelling, the possibility of a shallow Curie-temperature isotherm is not investigated here. Alsdorf and Nelson (1999) investigated the magnetic anomaly map derived using Magsat data and concluded that high heat flow in the Tibetan plateau could be a cause for the intense low anomaly pattern.

On the Indian subcontinent, the *initial model* magnetic anomaly map computed at satellite altitude fails to reproduce most of the large-scale observed anomalies, except over the regions of Indo-Gangetic plains lying south of the Himalayan fold belts, and some shield regions of India. The anomalies over the Myanmar region, east of the Indian shield, and in Pakistan to the west, are not reproduced in the predicted anomaly map. Lack of information on geological features overlain by Phanerozoic cover in south-central Pakistan is partially responsible. In the east, the complex interaction of the Indian plate with the Cathaysian plate has deformed them, and an active subduction in the region (Satyabala, 1998) can be a possible source for the observed anomaly pattern over Myanmar. This subducting plate has not been modeled in the present modelling method. The anomalies over eastern peninsular India agree well with the observations, though the circular feature over the Eastern Dharwar region in the observed map is completely absent in the predicted map. The negative anomaly over the Narmada-Son basin appears to extend in the south direction over the Deccan plateau. It is apparent from the results for the entire subcontinent that the nature of its lower crust and also its interaction with Cathaysian plate need to be understood properly.

4.2.2 Siberian craton

Satellite derived magnetic anomaly maps have rarely been used to study this craton and the work is restricted to map the Kursk anomaly, Russia. Taylor and Frawley (1987) derived scalar and vector maps to study the Kursk anomaly while Ravat et al. (1993) used only scalar maps to model the anomalies.

The observed vertical field magnetic anomaly map for the Siberian craton, shown in Figure (4.4a), shows the major anomalies associated with the shield region. In the north, a positive anomaly is associated with the Anabar shield, (1), however the anomaly extends further northwest over the Phanerozoic Khatanga trough, (2). An anomaly of moderate intensity is associated with the Vilyuy syneclise, (3), located southeast of the Anabar shield. Further southeast of this syneclise lies a positive anomaly over the Aldan shield, (4), and partly over the Aldan anteclise, (5). At the southern tip of the Siberian craton lies an anomaly trending parallel to the eastern flank of Baikal lake, (6). This anomaly overlies the southern half region of Baikal fold belt. A strong negative anomaly is observed north of Aldan shield, which follow the meandering east-northeast boundary of Siberian craton and is associated with the basin region of the Verkhoyansk fold belt, (7), in the north and Okhotsk-Chauna fold belt, (8), in the south. Further east of Verkhoyansk fold belt a positive anomaly can be observed that lies all along the eastern flank of Cherskiy suture zone, terminating north of Kamchatka peninsula. This anomaly is attributed to the partly buried Kolyma block, (9), that got accreted along with Omolon massif, to the northeast Siberia (Fujita, 1978).
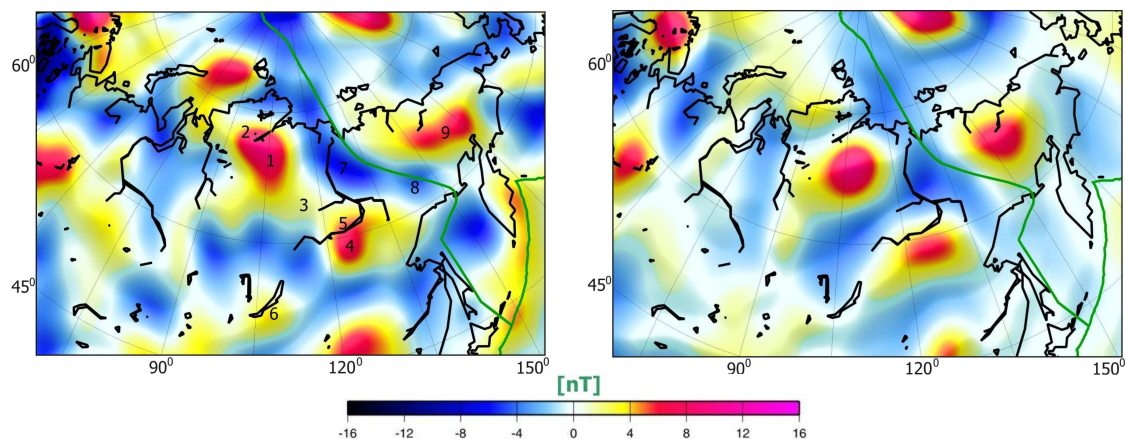
Fig. 4.4a. Observed vertical field anomaly map for spherical harmonic degrees 16-80 at an altitude of 400 km for the Siberian craton.

Fig 4.4b. *Initial model* vertical field anomaly map for spherical harmonic degrees 16-80 at an altitude of 400 km for the Siberian craton.

The *initial model* map for the Siberian craton (Fig. 4.4b) is calculated using the susceptibility distribution for geological units as mentioned in Appendix (IV). The tectonic map for the Siberian craton is shown in Figure (2.2). Over the Anabar shield in the north, a large positive anomaly can be compared with that of the anomaly of the observed map, however, the northwestward extension of the observed anomaly over the Khatanga trough is completely missing from the predicted map. This result points to our limited knowledge of the subsurface extension of Anabar shield, especially in the

northwest direction. An anomaly over the Aldan shield in the southwest Siberian craton agrees well with the observed anomaly, although a part of the anomaly is yet unaccounted for. A negative anomaly observed over the Verkhoyansk fold belt, extending all along to the Okhotsk sea, is in good agreement with the observations. A positive anomaly appears over the northern and southern region of Baikal fold belt. This differs from the observed map where the anomaly is observed only at the center of the fold belt.

Kolyma block is modelled based on the study of Sweeney (1981), and *initial model* vertical field anomaly map is computed over the region. Considering the subsurface extension of the block as envisaged by Sweeney (1981), the predicted anomaly does not match the observed anomaly pattern, although the amplitude agrees very well. This anomaly is reinvestigated in detail in Chapter 5 to redefine the boundary of this block.

4.2.3 East European craton

The East European craton has been most extensively studied using the satellite data. Since it hosts some of the largest magnetic anomalies at satellite altitude, it has drawn lots of attention to interpret them. Maps derived using only Magsat data include the work of Arkani-Hamed and Strangway (1986b), DeSantis et al. (1989), Cain et al. (1989b), Nolte and Hahn (1992), Ravat et al. (1993) and Taylor and Ravat (1995).

The East European craton includes diverse geological features. The CHAMP observed magnetic anomaly map shown in Figure (4.5a) reveals the anomaly features corresponding to some of these geological bodies. In the north, within the Baltic shield, an intense positive anomaly is observed over the Kiruna mines, (1), in north Sweden. A strong negative anomaly is observed south of it over the Svecofennian domain, (2), and the southern Karelian province, (3), in the north and over Moscow syneclise, (4), in the centre of the East European craton. Further south, east of the Ukranian shield, is situated one of the largest positive anomalies on the global magnetic anomaly map. This anomaly, called 'Kursk Anomaly' is associated with the iron formations of Voronezh anteclise, (5), Russia. An anomaly corresponding to the Ukranian shield, (6), is almost non-existent at satellite altitude. A positive anomaly follows the western border of the craton marked by the TTZ (Tornquist-Teisseyre Zone), (7), extends into the Baltic sea, (8), and terminates in the southwest Scandinavian, (9), region. Apart from the Belorussian uplift, (10), located north of the Ukranian shield, there is no other geological affinity to the anomaly pattern observed. Another interesting anomaly feature is observed over the southern Ural mountains, (11), with its westward extension further inside the craton, partly overlying the Volga-Urals anteclise and Tatarian swells, (12).

The vertical field magnetic anomaly map computed at a satellite altitude of 400 km using the susceptibility distribution described for various geological units in Appendix (V), is shown in Figure (4.5b). The tectonic map for the East European craton is shown in Figure (2.3). A positive anomaly observed over the Kiruna mines is associated with iron formations in the region and is reproduced well in the *initial model* map. A negative anomaly observed over the Moscow syneclise and regions of the southern Baltic shield is

due to the removal of long-wavelength anomaly associated with a basement of craton. This may partly be due to thick Phanerozoic cover over the Moscow syneclise, however, some part of the anomaly is yet unaccounted for. The anomaly computed over the Voronezh anteclise is in agreement with the Kursk magnetic anomaly observed over this region. This anomaly is associated with early Proterozoic iron formations in the region, which extends for more than 1000 km (Goodwin, 1991). The extended anomaly pattern computed along the TTZ shows a similar trend as has been observed. However, the anomaly is not reproduced in the north, especially over the Baltic sea and in the southwest Scandinavian domain. The modelling results indicate that the anomaly along the TTZ is produced due to the bulk susceptibility contrast of the thick crust in the west and thinner on the east and is not due to any geological body of high susceptibility lying along the zone except for the Belorussian anteclise. The anomalies over the central Urals and Volga-Urals anteclise also agree well with the observed map.

Fig. 4.5a. Observed vertical field anomaly map for spherical harmonic degrees 16-80 at an altitude of 400 km for the European craton.

Fig. 4.5b. *Initial model* vertical field anomaly map for spherical harmonic degrees 16-80 at an altitude of 400 km for the European craton.

An unresolved question about the East European craton basement is its extent. Deep drilling results for the basement of craton provide 23 known Archean units filled in by early Proterozoic rocks (Goodwin, 1991). However, the extension of these units is largely open to speculation. In the derivation of initial VIS model the basement is assumed below the craton at all the regions except south of Voronezh anteclise. There is consistent variation of sediment thickness from north to south of the craton. It is 0-2 km in the north and 4-6 km over the Moscow syneclise in the center and more than 23 km thick (Khain, 1985) over the north Caspian sea syneclise in the south. In spite of such a craton structure a strong positive anomaly was expected over the center of craton. On the contrary a negative anomaly is noticed over the Moscow syneclise and southern Baltic shield and a strong positive anomaly along the TTZ. The *initial model* matches well with the observed pattern over the center of craton. This means the basement behave as a single large unit and long wavelength associated with the craton is removed with the removal of spherical harmonic degrees 1-15. This may produce the negative over the center of craton and positive over the western region along TTZ followed by a negative anomaly over the west of craton.

51

4.2.4 North American craton

The North American craton consists of a wide range of geologic bodies and has been studied extensively by both surveys of surface geology and geophysical investigations of the lithosphere. The satellite anomaly maps have been derived to fill the gaps in these studies, especially in the geophysical surveys. This is helpful for developing an hypothesis for the origin of magnetic signatures in less well-known or exposed regions of the Earth. Some of the earlier studies in this regard have been carried out for the United States by Mayhew (1982a) and Langel (1990) using Magsat and POGO satellite data. For the mid continent region, Carmichael and Black (1986) and for lower crustal thickness variation by Schnetzler (1985). Whaler and Langel (1996) prepared a magnetisation map of the United States from Magsat data while and Purucker et al. (2002) used both Magsat and Ørsted data. The northern part of the large continent, the Canadian shield region, has also been studied by Langel et al. (1980) and Arkani-Hamed et al. (1984). The observed vertical field magnetic anomaly map of the North American craton is shown in Figure (4.6a) and the *initial model* magnetic anomaly map in Figure (4.6b).
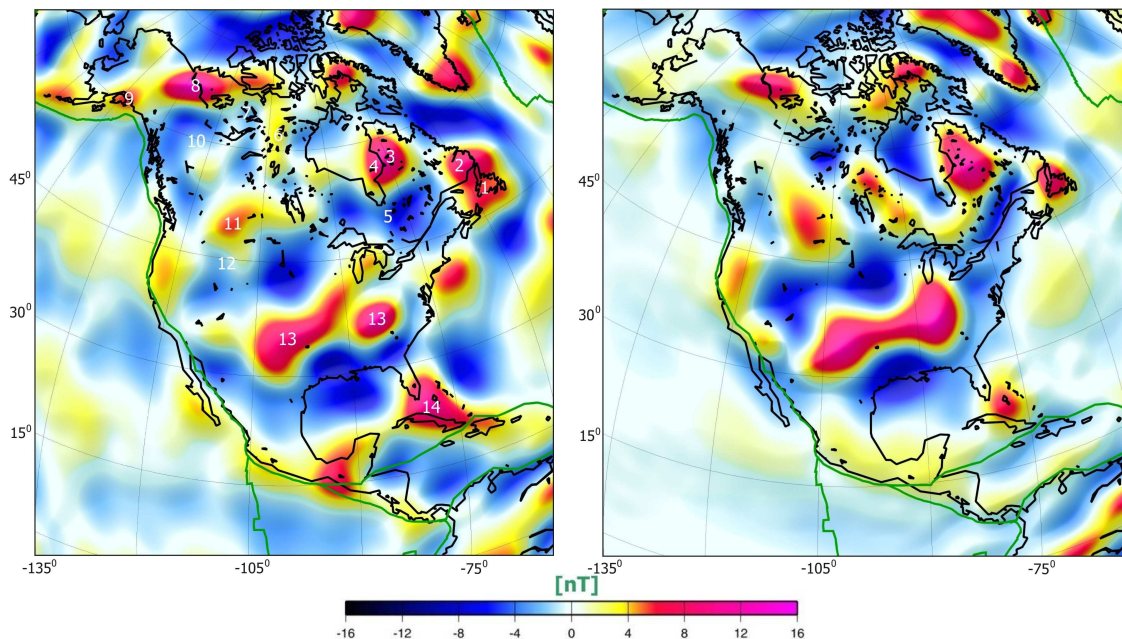
Fig. 4.6a. Observed vertical field anomaly map for spherical harmonic degrees 16-80 at an altitude of 400 km for the North American craton.

Fig. 4.6b. *Initial model* vertical field anomaly map for spherical harmonic degrees 16-80 at an altitude of 400 km for the North American craton.

The observed anomaly map shows scattered anomaly patterns all over the craton, mostly lying over the Precambrian units. In the northeastern region, a flattened bell- shaped positive anomaly is observed over Newfoundland, (1), that extends further north over the eastern region of Grenville province, (2). Northwest to this anomaly, within the Superior province, a large oval-shaped anomaly lies over the Ungava craton, (3), and part of Belcher iron formations, (4), in Hudson Bay. Regions south and southeast of Hudson bay, (5), are characterised by a negative anomaly of moderate intensity. The regions west of Hudson Bay, over the Churchill province, (6), show a weak positive anomaly which

stretches in a north-south direction. Interestingly, the Archean Slave province, (7), appears almost non-magnetic at satellite altitude. Located in the northwest region of the craton, there is a large elongated positive anomaly, (8), extending from Slave craton to the Yukon province of Canada. This large stretch of anomalies lies over the Wopmay orogenic units, primarily exposed only in the northwestern region of the Slave craton and partially buried further west of it. Small positive anomaly features, (9), extend to the Bering Sea along the Aleutian arc and are attributed, within the continents, to the exotic terrains accreted to the Cordilleran units of the North American craton (Sweeney, 1981). A weak anomaly pattern southeast of Wopmay orogen is observed over the Mackenzie-Wernecke mountains, (10), of Proterozoic age. An intense positive anomaly, (11), also appears north of Wyoming province, (12), whose source regions are yet to be determined, because of the thick Phanerozoic cover that masks the underlying structure. Further to the south of this large craton, over southwest USA, (13), lies one of the largest stretches of satellite-altitude anomalies on Earth. These anomalies lie over the mid-Proterozoic provinces, dominated by anorogenic granite intrusions in the crust. Lastly, a positive anomaly, (14), can be observed extending from the banks of Florida to the Bahamas Island. The origin of these anomalies is yet unresolved, as it is generally attributed to the underlying oceanic crust, and few believe that it is due to continental crust.

Global seismic crustal model CRUST2.1, a higher resolution model of its predecessor CRUST5.1 (Mooney et al., 1998), is known to be much more accurate in the North American craton, especially in the western region of the craton, than estimated by 3SMAC seismic model. Thus, CRUST2.1 model is preferred over the 3SMAC model for the VIS computation for North American craton. Using the susceptibility distribution for various units of the North American craton as shown in Appendix (VI), *initial model* vertical field anomaly map is computed at an altitude of 400 km. The tectonic map for the North American craton is shown in Figure (2.5). A comparison is done with the observed anomaly map for the corresponding regions. The region of Newfoundland is known for ophiolite accretion during the Taconic orogeny, mid Ordovician (Colman-Sadd, 1980). Bay of Island and its surrounding region occupy more than a 100 km stretch of ophiolites (Colmann-Sadd, 1980). The anomalies predicted over this region show a positive only over the Newfoundland region in agreement with the observations. The part of anomaly over the Grenville province northwest of Newfoundland, however, is not reproduced.

The predicted anomaly over the Ungava province of the Archean Superior province and its extension over the Belcher iron formations in the Hudson Bay show a good correspondence with the observed map. An extended positive anomaly pattern of moderate intensity over the southwest region of Superior province is in disagreement with observations, which show a corresponding negative anomaly. A similar positive anomaly of moderate intensity, stretching in the north-south direction, located west of Hudson Bay over the Churchill province, is not reproduced in the *initial model* magnetic anomaly map. An intense positive anomaly predicted over the Wopmay orogen, overlain by Phanerozoic cover in the Yukon state, shows a good resemblance with the observed magnetic map. Further south in Mackenzie state, the anomaly over the Mackenzie mountains also shows a good correlation with the observations. However, the east-west trending positive anomaly south of it and north of Wyoming uplift is reproduced only

partially. The moderate positive observed over the western coast of the USA, attributed to the accreted Arc terrain during Permian-Triassic era (Dickinson, 1981), matches the observed anomaly pattern over the same region.

In the southeast USA, the large stretch of anomaly over the Kentucky-Tennessee region characterized by the mid-Proterozoic anorogenic granite province is reproduced reasonably well; however, the predicted anomaly pattern does not follow the boundary of the observed anomaly. Apparently, this region needs to be investigated in detail to redefine the boundary of this mid-Proterozoic province, as it is largely buried under Phanerozoic cover. The results of investigation are shown in chapter (5).

The positive anomaly over the region of the Bahamas Islands is reproduced well. However, its extension to the bank of Florida is not evident in the *initial model* anomaly map. This indicates a more extended oceanic crust beyond the political boundary of Florida and the Bahamas. The modelling results indicate that this anomaly is due to oceanic crust, as the crust of continental origin is unable to reproduce such intense anomaly patterns.

4.2.5 South American craton

Shield regions dominate the northern part of the South American craton and the Precambrian Sao Francisco and Ribeira belts occupy the central-eastern region of the craton. This craton has generally been a target of study to find the continuation of rock types from its eastern region to the western region of mid-Africa prior to the Gondwana break-up. Some of the work in this respect and in general to map the sources for magnetic anomalies over South America has been carried out by Hinze et al. (1982), Ridgway and Hinze (1986), von Frese et al. (1989) and Ravat et al. (1991). They prepared scalar anomaly maps using Magsat satellite data.

The entire continent appears non-magnetic except for the shield regions as shown in the Figure (4.7a). Over the Guyana Shield in the north, the observed vertical field anomaly map shows a moderate positive anomaly both in the northern, (1), and southern flanks, (2). A negative anomaly, (3), is observed over the northern part of the Brazilian shield. This anomaly extends further northwest, (4), over the basin of Amazon river. At the mouth of the Amazon river, (5), a positive anomaly over the sedimentary basin is observed that overlie partly the San Ignacio mobile belt. Further southeast, an anomaly of moderate intensity lies over the Sao Francisco belt, (6), and Ribeira belt, (7), that extends partly into the South Atlantic Ocean.

The vertical field anomaly map for the South American continent is computed using the susceptibility distribution given in Appendix (VII) and is shown in Figure (4.7b). The tectonic map for the South American craton is shown in Figure (2.6). For Guyana shield regions, in South America, the new seismic crustal model of Schmitz et al. (2002) was included in place of 3SMAC model.
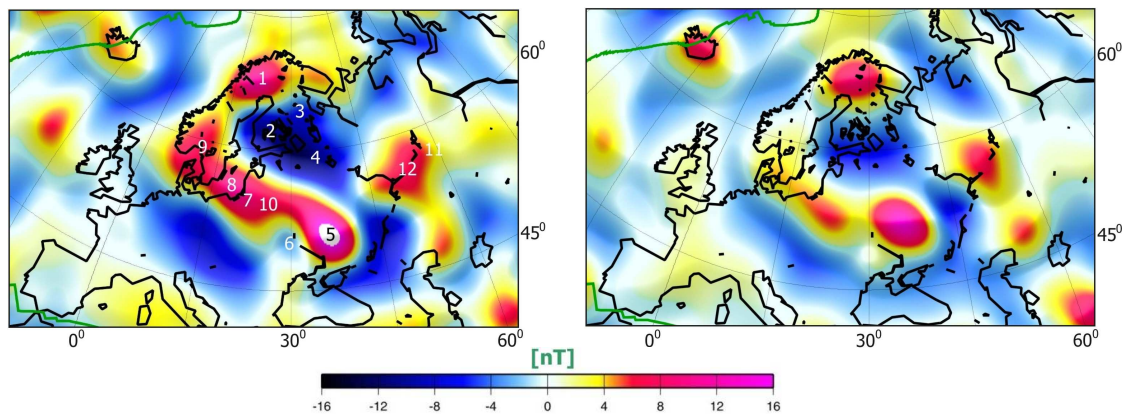
Fig. 4.7a. Observed vertical field anomaly map for spherical harmonic degrees 16-80 at an altitude of 400 km for the South American craton.

Fig. 4.7b. *Initial model* vertical field anomaly map for spherical harmonic degrees 16-80 at an altitude of 400 km for the South American craton.

A comparison of the *initial model* anomaly map with the observed anomaly map (Fig. 4.7a) suggests a good agreement of the anomaly pattern. The positive anomalies predicted over the shield regions is in agreement with the observations, suggesting their sources to lie within the Precambrian units of the shield regions, though they are stronger in amplitude than the observed anomalies. The anomaly observed over the north Guyana shield is located further north over the southern bank of Orinoco river, suggesting the greenstone belts units of Guyana shield, producing these anomalies, extend further north below the Phanerozoic cover. A positive anomaly over the sedimentary basin of the Amazon river, overlying the San Ignacio mobile belt, is also reproduced reasonably well though the predicted anomaly appears still larger and stronger. A single hump-shaped negative anomaly observed at the center of the Amazon river however, is not exactly reproduced in the predicted map. The negative anomaly over the north Brazilian shield is also not reproduced. Further southeast, the positive anomaly observed over the San Francisco craton and Ribeira belt appears shifted north in the *initial model* map. The extension of the cratonic region into the ocean is not modelled in the present work due to lack of such data. However, based on the observed anomaly pattern over the oceanic region, a possible eastward extension of San Francisco belt in the Continental arc region cannot be ruled out.

The southern region of the South American craton is covered by Phanerozoic including the Andes. As the Phanerozoic cover is associated with a constant susceptibility value, the difference in VIS values can only arise due to variation in crustal thicknesses. The

55

predicted anomaly pattern from the *initial model* suggests no interesting anomalies over the southern South American craton, which is in disagreement with the observations. The observed anomaly map does show some magnetic anomaly features over the central Andes. This result indicates that variation of magnetic properties in the younger crust may be important in modelling crustal anomalies.

4.2.6 African craton

Not much is known of this large continent due to the scarcity of extensive ground geophysical surveys, especially in the interior of the craton. However, using satellite data there has been some effort to extract more information about the nature of the crust underlying the cratons and mobile belts. One of the most enigmatic magnetic anomalies lies in Central Africa, at Bangui. The source of the anomaly is considered to be geological by Regan and Marsh (1982) while Girdler et al. (1992) modeled the anomaly using an iron meteorite. The West African craton received similar attention by Ravat (1989) and Toft et al. (1992).

Using the geological and tectonic information of Africa (Goodwin, 1991) and their average susceptibilities as listed in Appendix VIII, the vertical field anomaly map is computed (Fig. 4.8a) and compared with the corresponding observed magnetic anomaly map (Fig. 4.8b). The tectonic map for the African craton is shown in Figure (2.7).

Over the West African Craton, the observed vertical field anomaly map shows a band of negative amplitude that extends over the Man shield, (1), and is strongest over the central region of Taudeni basin, (2). A negative anomaly is also observed over the Tindouf basin, (3), north of the Reguibat shield. A strong positive anomaly is observed over the Amsaga belt, (4), of the Reguibat shield, that partly overlies the northwestern region of Taudeni basin. A positive anomaly is also observed over the Archean Liberian shield, (5). This anomaly extends further southwards into the South Atlantic ocean. The entire Hoggar shield, (6), appears to be very weakly magnetic. Over the Benin-Nigeria shield in the southeast of West African craton, a positive anomaly is seen over Nigeria shield, (7), while the Benin shield, (8), appears non-magnetic. The *initial model* anomaly map does reproduce the negative anomaly over the Taudeni basin flanked by positive anomaly on either side, in agreement with satellite observations, but most of the amplitude is yet unaccounted for. The entire Hoggar shield appears non-magnetic, which agree partially with the observed anomaly map. Over the Benin-Nigeria shield a disagreement in the anomaly patterns between the predicted and observed map is evident over the Nigeria shield and agreement over the Benin shield.

In northeast Africa, the observed map shows no interesting anomaly features except over the Nubian-Arabian shield. The mid-Proterozoic Nubian shield, (9), is almost non-magnetic whereas the Arabian shield, (10), generates a positive. The computed map agrees well with the observed map, although the positive observed over the Arabian shield appears further south in the Arabian peninsula.

56

In the central African region, one of the largest anomalies, the Bangui anomaly, is observed over the center of Africa, at Bangui, (11). The Bangui anomaly characterised by intense negative amplitude, lies along the central Pan-African belts, just north of the Congo craton. The southern flanking positive anomaly, (12), is situated over the thick sedimentary basin of the northern region of Congo basin, (13). The southeast extension of this anomaly is observed over the Kibalian block, (14). The anomaly pattern over the Tanzanian craton, (15), southeast of Congo craton, show a moderate negative. A moderately negative anomaly is observed over the Kasai craton, (16). Further south, a strong positive anomaly is seen over the western region of Angolan craton, (17), while only of moderate intensity over the eastern region. The *initial model* magnetic anomaly map shows a similar trend of the anomalies over the Central Pan-African belt and Congo Basin. However, a large part of the amplitude is yet unaccounted for. This anomaly is studied in detail in chapter (5) where a possible source for the anomaly is investigated. The anomaly pattern over the Tanzanian craton, southeast of Congo craton, is in good agreement with the observations. Most of the Kasai-Angolan craton, located south of the Congo craton, has rock types of low susceptibility and hence a weak negative anomaly is predicted over the region, in agreement with observations. A stretch of positive anomaly observed over the western region of Angolan craton is not reproduced in the *initial model* map. This observed positive anomaly lies over the exposed Archean rocks and the adjoining volcanic rocks in the Kunene region, located in southern region of Angolan craton.

Fig. 4.8a. Observed vertical field anomaly map for spherical harmonic degrees 16-80 at an altitude of 400 km for the African craton.

Fig. 4.8b. *Initial model* vertical field anomaly map for spherical harmonic degrees 16-80 at an altitude of 400 km for the African craton.

In south Africa, the southern portion of the Namaqua-Natal belt, extending up to the Cape fold belt shows a prominent positive, (18), and can be seen both in the observed and predicted map. A long stretch of negative anomaly is observed all along the Kaapvaal craton, (19). This anomaly trend turns eastward where it terminates over the Limpopo mobile belt, (20). The region north of this belt is marked by a weak positive anomaly and it overlies Zimbabawe craton, (21). The region of Damara fold belts, (22), trending NE-SW, located east of Kaapvaal craton, and mostly overlain by the Kalahari sands, appear weakly magnetic over its eastward extension but moderately magnetic over its western region. However, a weak positive anomaly is observed over the western boundary, immediately south of Angolan craton. The predicted vertical field magnetic anomaly map for South Africa is in good agreement with the observations. A positive anomaly over the Namaqua-Natal belt matches well with the observed while the long extended anomaly over the Kaapvaal craton is in good agreement as well. However, this anomaly extends further north over the Zimbabwe craton and the anomaly over the Limpopo belt is only partly reproduced. The anomaly pattern over the Damara fold belts agrees well with the observed, though a part of the positive anomaly in the western region is yet unaccounted for.

4.2.7 Australian craton

This thoroughly studied continent both by ground and airborne geophysical surveys, consists of diverse geological units. Most prominent among them are Pilbara and Yilgarn cratons in the east, with many Proterozoic belts in the center of the continent. Mayhew and Johnson (1987), using Magsat data, provided a magnetisation map using an equivalent source model. Later Mayhew et al. (1991) estimated values for the total vertical integral of magnetisation across the Yilgarn block.
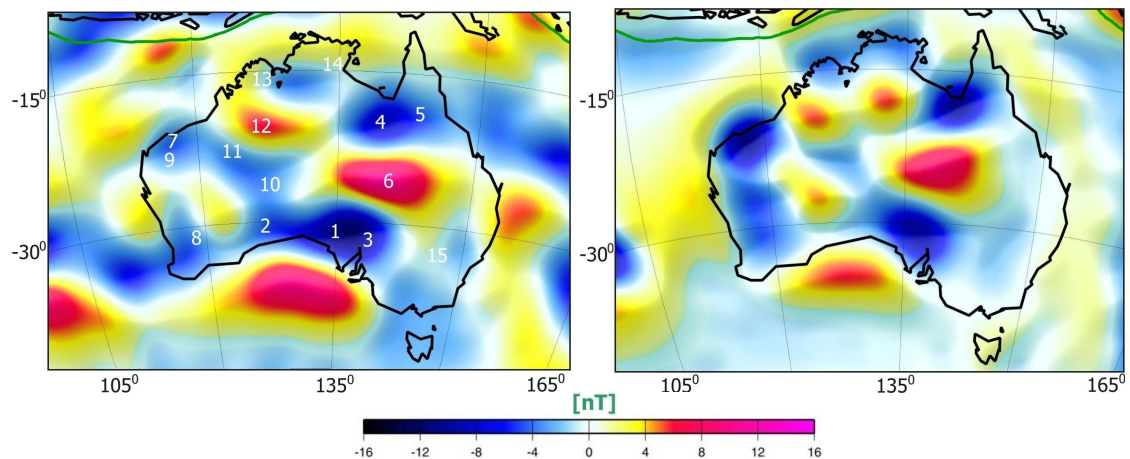
Fig. 4.9a. Observed vertical field anomaly map for spherical harmonic degrees 16-80 at an altitude of 400 km for the Australian craton.

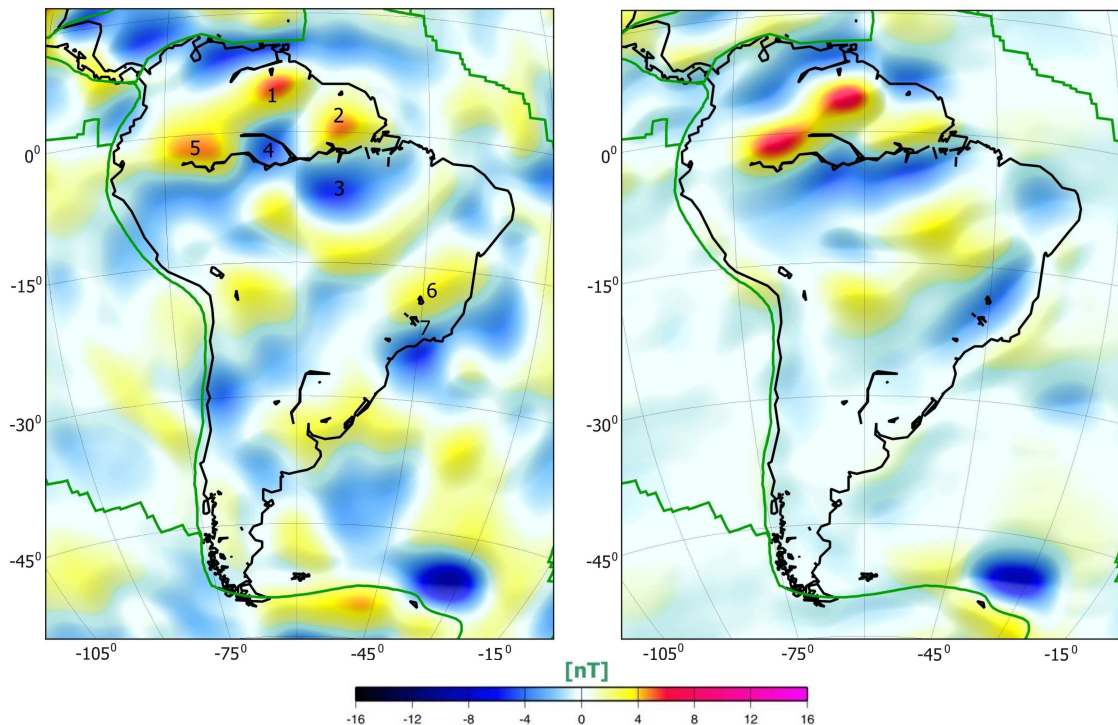Fig. 4.9b. *Initial model* vertical field anomaly map for spherical harmonic degrees 16-80 at an altitude of 400 km for the Australian craton.

The CHAMP observed vertical field magnetic anomaly map of the Australian continent is shown in Figure (4.9a). A large negative anomaly is observed over the Gawler craton (1), over the western segment of largely buried Nullarbor block, (2), and over the Adeladean

syneclise, (3), located east of the Gawler craton. An intense negative anomaly is observed over the region of Mount Isa Inlier, (4), and Georgetown Inlier, (5), located in the northeast region of the continent. Between Mount Isa Inlier in the north and the Gawler craton in the south lies a high positive anomaly, (6), a region covered by thick Phanerozoic sediments. Interestingly, the negative anomalies over the Archean blocks of Pilbara, (7), in the north and Yilgarn, (8), in the south are of low intensity. A negative anomaly pattern is associated with the banded iron formations of Hamersley basin, (9). An anomaly pattern is also observed extending from the Pibara craton to the central Musgrave ranges, (10), which overlie the sedimentary basin of Paterson province, (11). In central Australia, north of Arunta Ranges, lies an extended positive anomaly, (12). A weak anomaly pattern can be observed in the northern region of the Australian continent, over the Kimberley, (13), and McAurthur, (14), basin. The east Australian region, (15), mostly covered by the Phanerozoic cover appears almost non-magnetic at satellite altitude.

Magnetic anomaly map for the vertical component is computed for the susceptibility distribution (Appendix IX) for various geological units of Australian continent (Fig. 4.9b). The tectonic map for the Australian craton is shown in Figure (2.9). The anomaly observed over Gawler craton, Nullarbor block and over the eastern adjoining Proterozoic belts agrees well with the observed anomaly map. This modelling result confirms the Archean basement below the Adeladean syneclise. Largely buried Nullarbor block is also present west of Gawler craton and the anomaly pattern over it confirms its existence. Though, a part of anomaly over the Nullarbor block is not predicted well over the region. The region over the Mount Isa Inlier and Georgetown Inlier shows an anomaly of low intensity that is in agreement with the observations. A large positive anomaly located over the region between Mount Isa in the north and Gawler craton in the south is reproduced well. The positive anomaly north of Arunta range is only partially predicted in the *initial model* map. Anomalies computed over the Pilbara craton and Yilgarn craton agree well though the predicted anomaly over the Pilbara craton is more intense. A very strong negative anomaly is also observed over the Hamersley Basin whose amplitude is in surplus when compared with the observations. The anomaly observed over the Paterson province, however, is not reproduced in the predicted map. Anomaly computed over Kimberley and McArthur basin agrees only partially with the observations. In east Australia, the anomaly patterns between the observed and computed map is in good agreement.

4.2.8 Greenland

This country, which is covered by 90% with ice, has rarely been investigated in detail using magnetic satellite data. The geological information for Greenland has only been inferred on the basis of exposure of rock types at the periphery. However, in its central region, geological units have always been a mystery. Lately, more seismic results have thrown some light onto possible tectonic units of Greenland (Dahl-Jensen et.al, 2003) in its interior. Langel and Thorning (1982) used POGO satellite data to estimate a magnetisation map for Greenland, but no effort was made to interpret the anomalies.

The vertical field anomaly map of Greenland is shown in Figure (4.10a). A high positive anomaly is observed over the Archean block of southern Greenland, (1). Over the northern region of Greenland there is an anomaly, (2), that extends from East to West. The central Greenland, (3), show negative anomaly pattern of moderate intensity.

The vertical component map is computed using the susceptibility distribution of rock types exposed at the periphery of the country (Appendix X). The tectonic map of Greenland is shown in Figure (2.4). The predicted anomaly over the southern Archean block shows a good agreement with observations (Fig. 4.10b). The anomaly pattern over the northern region shows a broad anomaly that extends from northern Greenland to the central region of the country. The predicted anomaly, though it partly agrees with the observed anomaly, is significantly more extended in south direction. This extension of predicted anomaly in southward direction is caused by the crustal thickness variation within Greenland. The extent of this anomaly is investigated further in chapter 5.
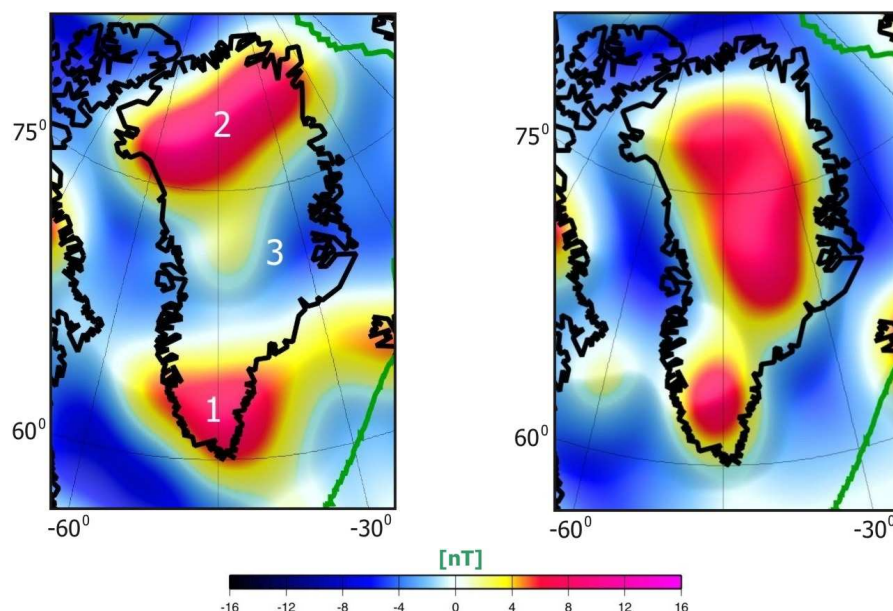
Fig. 4.10a. Observed vertical field anomaly map for spherical harmonic degrees 16-80 at an altitude of 400 km for the Greenland.

Fig. 4.10b. *Initial model* vertical field anomaly map for spherical harmonic degrees 16-80 at an altitude of 400 km for the Greenland.

4.2.9 Antarctic craton

Not much is known about this continent as far as regions covered with ice are concerned. Though intense exploration work is carried out in Antarctica, it is mostly restricted to the exposed geological regions. Using satellite data, efforts were made to estimate a crustal field model over the south pole (Langel and Thorning, 1982; Ritzwoller and Bentley; 1982; Alsdorf et al., 1994; von Frese et al., 1997). von Frese et al. (1997, 1999) made an effort to model these anomalies based on satellite gravity and magnetic data. Recently, Kim et al. (2002) mapped the regional anomalies over Antarctica using Ørsted satellite data.
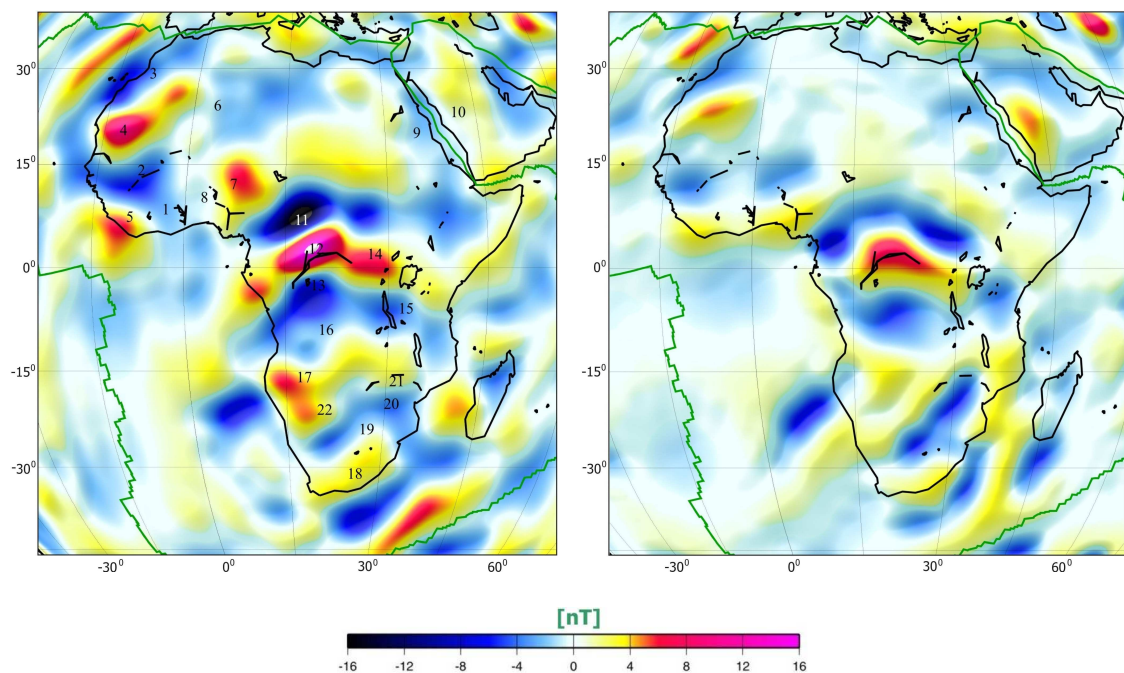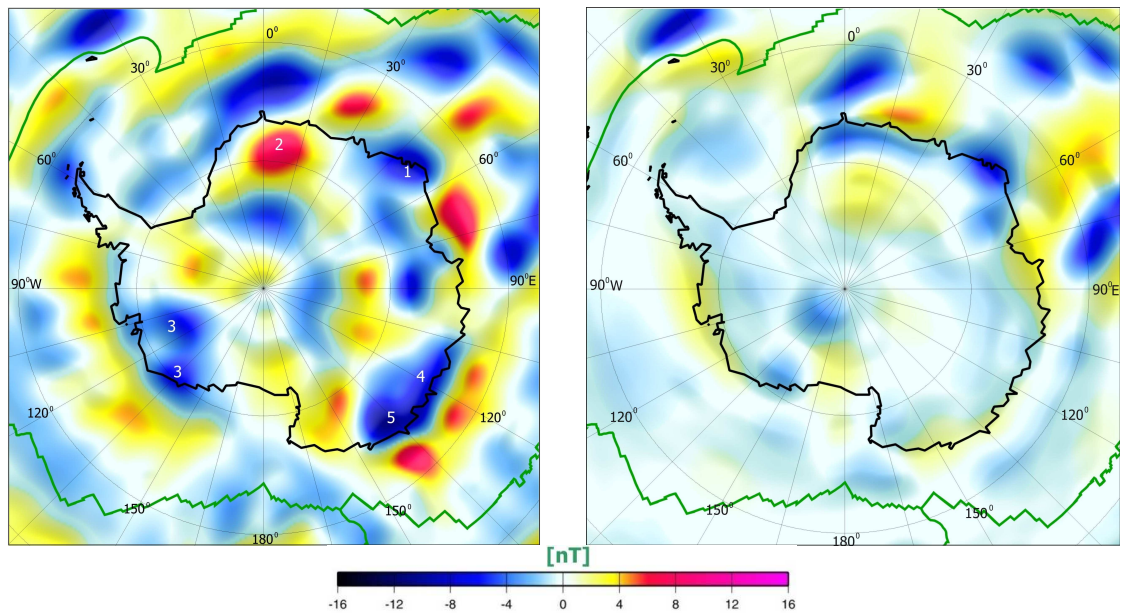
Fig. 4.11a. Observed vertical field anomaly map for spherical harmonic degrees 16-80 at an altitude of 400 km for the Antarctica.

Fig. 4.11b. *Initial model* vertical field anomaly map for spherical harmonic degrees 16-80 at an altitude of 400 km for the Antarctica.

The observed vertical field anomaly map over the continent of Antarctica is shown in Figure (4.11a). The map shows some of anomalies, not only over the geological regions exposed, but also over the regions covered with ice. The most prominent regions that are exposed and an anomaly associated with it are Napier and Rayner Complex, (1), located south of Kerguelen plateau and lying between longitude 45^0-60^0 East. An elongated large positive anomaly is observed over the Dronning Maud Land, (2). There are two other anomalies located over the region between 90^0-150^0 West, (3), centered on 80^0 South. The other anomalies that lie along the coast of Antarctica is located over Wilkes Land, between 105^0 E and 145^0 E, (4), and one centered on 135^0 W, (5). There are some anomalies in the interior of the continent, but they are over the ice-covered region and their geological association cannot be ascertained at this moment.

Precambrian units of the exposed Antarctica regions are modeled and their susceptibility distributions are shown in Appendix XI. The tectonic map for the Antarctica craton is shown in Figure (2.10). The predicted anomaly pattern over Rayner and Napier complex is reproduced well (Fig. 4.11b). An anomaly of low intensity observed east of it is, however, not reproduced. The anomaly over Dronning Maud Land is not reproduced in the *initial model* anomaly map. A significant portion of anomaly over the region lying between 90^0-150^0 is not produced. An anomaly observed over the region centered on 135^0 W, between 105^0-145^0 E, is completely missing from the *initial model* map. The anomaly observed at other regions is not at all reproduced in the predicted map due to the lack of geological information for these ice covered regions.

4.2.10 Oceanic crust

The oceanic crust is of uniform thickness across the globe. The oceanic plateaus occupy 10% of the oceanic region. Remanent magnetisation dominates in the oceanic crust, as evidenced from the seafloor spreading anomalies. Harrison (1987) and Tivey (1996) reproduced these spreading anomalies by assuming the magnetisation restricted to layer 2. However, at the satellite altitude these spreading anomalies cancel each other. It was argued by Arkani-Hamed and Strangway (1986c) that upper mantle also contributes to the long wavelength anomalies observed over the oceans. Based on the model study of subduction zones at Kuril-Kamchatka trench, they reported the upper 35 km of oceanic upper mantle to be magnetic with an effective magnetic susceptibility of 0.0085 SI. Thus possible contribution of magnetisation from the upper mantle is not ruled out (Arkani-Hamed, 1988, 1991). However, Thomas (1987) proposed a model in which viscous and induced magnetisations were the main sources of the long-wavelength anomalies seen in satellite data.

The observed vertical field magnetic anomaly map of the world is shown in Figure (4.12). This section deals with the study of anomalies observed over the oceanic region. Anomalies of moderate intensity (2 – 4 nT) are seen over all of the major oceans of the world. The magnetic strips of highs and lows parallel to the mid-oceanic ridges, so prominent in the aeromagnetic surveys, are mostly absent at satellite altitude, except for few lineations parallel to the mid-oceanic ridges observed over the North Atlantic Ocean. This is due to the fact that fields from the alternating remanent magnetisations of the oceanic floor spreading magnetic anomalies are nearly cancelled at satellite altitude. However, Hayling and Harrison (1986), Purucker et al. (1998) modeled anomalies associated with KQZ (Cretaceous Quiet zones) in the Atlantic Ocean. The oceanic crust in these zones, being wide enough to retain magnetic signature of the Cretaceous normal, result in measurable anomalous fields at satellite altitude (LaBrecque and Raymond, 1985). There are anomaly patterns over the oceanic region that do not seem to have a geological source, and could be uncorrected external signals and high degree main field. It is due to the fact that the anomalies over the oceans are generally much weaker that the main field of degrees 16-20 can be seen there. Even then, the comparison of the observed map with the world geological map makes it clear that most of the observed anomalies over the oceanic regions are due to the scattered oceanic rises, mounts and plateaus, where the oceanic crust is generally thicker than the surrounding crust. Some of these plateau-like structures are dismembered part of continents, especially in the Indian Ocean, created as a result of Gondwana breakup.

The modelling of oceanic crust is done using the 3-layered model for oceanic crust of which the top layer of sediments is considered non-magnetic. The susceptibility distribution used for modelling is shown in Appendix XII. The *initial model* magnetic anomaly map for the vertical component over the oceanic region is shown in Figure (4.13). The predicted anomaly over the oceanic crust does not show interesting anomaly patterns, unlike those in observations where weak anomaly patterns are scattered everywhere. Over the oceanic plateaus and rises, the anomaly patterns in the *initial model* map agree well with the corresponding region of the observed map. Since the remanant

magnetisation of magnetic strips of alternate polarity across the mid-oceanic ridges is not included in the model, there are no magnetic signatures in the *initial model* map related to these alternate highs and lows. Considering a uniform layering of the oceanic crust, the predicted anomaly pattern is in good agreement with the observed magnetic anomaly map.
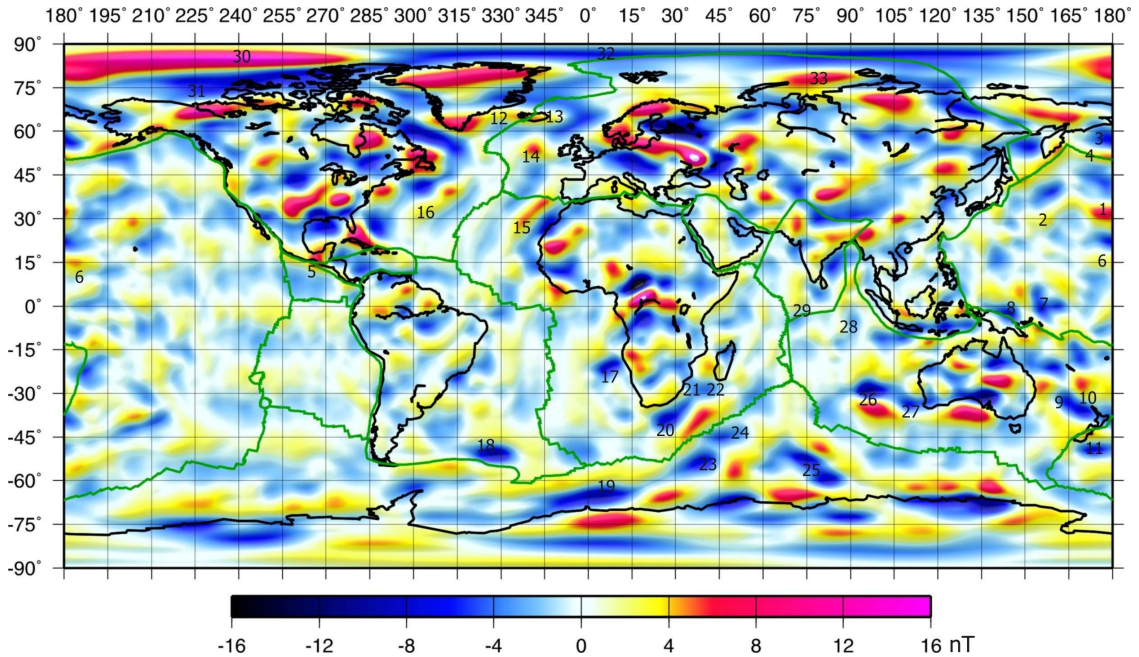
Fig. 4.12. Observed vertical field anomaly map for spherical harmonic degrees 16-80 at an altitude of 400 km shown in cylindrical equidistant projection. The numbers shown in white is marked over the plateaus.
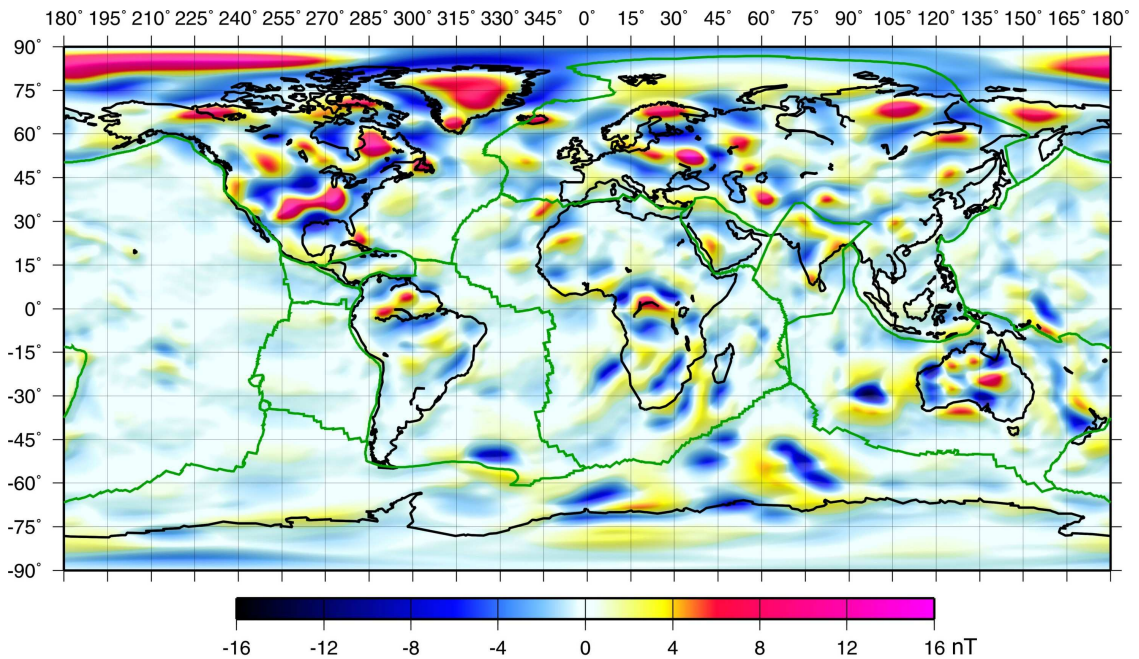
Fig. 4.13. Predicted vertical field anomaly map (*initial model*) for spherical harmonic degrees 16-80 at an altitude of 400 km shown in cylindrical equidistant projection.

63

The following section compares the observed and predicted anomalies associated with the oceanic plateaus, rise and scattered microcontinents for each of the Oceans.

4.2.11 Oceanic plateaus

Apart from interpretation of anomalies over the oceanic crust, the anomalous pattern observed over the plateaus and rises have generated sufficient interest to model these anomalies. One of the most comprehensive studies was conducted by Johnson (1985), who attributed the dipole anomaly over the Broken Ridge, to be due to significantly induced magnetisation and partly remanent. Bradley and Frey (1988) modeled the Kerguelen plateau and Broken ridge similarly. Fullerton et al. (1994) studied all the anomalies over the southwestern Indian Ocean region. Toft and Arkani-Hamed (1992) examined volcanic plateaus and the effects of the KQZ in the Pacific Ocean. Significant studies were conducted by Alsdorf (1991) over the south Atlantic Ocean and by Hayling and Harrison (1986) over the north and central Atlantic Ocean, while, Taylor (1991) studied the eastern Indian Ocean. All the above studies used Magsat satellite data for modelling and interpretation. Using CHAMP satellite data, we conducted similar studies and the following paragraphs describe the modelling results.

The observed anomalies over the Pacific Ocean as shown in Figure (4.12) are largely of moderate intensity. A prominent positive anomaly lies over the Hess rise, (1), northwest of the Hawaiian Islands, and a very low amplitude positive anomaly is observed along the Shatsky rise, (2). North of Hess Rise, in the Bering Sea, (3), lies a positive anomaly of moderate intensity, all along the Aleution arc, (4), that is attributed to the subduction zone of the northern Pacific region (Clark et al., 1985). A strong positive anomaly is observed at the southwest coast of Mexico, (5), also attributed to the presence of subduction zones in the region (Counil and Achache, 1987). Hawaiian ridge, (6), does not show up in the satellite altitude magnetic anomaly map, but weak anomaly patterns are observed in its surrounding. One of the largest negative anomalies, observed across the equator is associated with Ontong-Java plateau, (7), and another along the equator is observed west of it, (8), over the oceanic crust. Further south, due northwest of New Zealand, lies an intense negative anomaly associated with the Lord Howe Rise, (9). The anomaly extends not exactly along the rise, but in between the Lord Howe rise and Norfolk plateau, (10), in the northwest direction and abruptly terminates at the center of the Lord Howe rise. It then reappears as an oval-shaped anomaly over the northern tip of the rise. Another intense negative anomaly is observed over the center of Cambell plateau, (11), south of New Zealand.

Based on the VIS model of oceanic plateaus and rises (Appendix XII) the vertical field magnetic anomaly map is computed and is shown in Figure (4.13). A good correspondence can be seen between the predicted and observed anomaly patterns over the Ontong-Java plateau. Over the Shatsky rise in the north, a strong positive is noticed at the center of long stretch of rise, however, over the Hess rise, a large part of anomaly is yet unaccounted for. In the southern hemisphere, northwest of New Zealand, the predicted anomaly pattern does not follow the observations and appears shifted south over the Lord Howe rise and not in between the rise and Norfolk plateau which features

64

so prominently in the observed map. A negative anomaly is seen at the northern edge of the Lord Howe rise in agreement with observations. The negative anomaly south of New Zealand is also not predicted in the *initial model* map. In short, the anomalies corresponding to all of the plateaus in the Pacific oceanic region are only partly recovered and require further investigation.

Both the North and South Atlantic Ocean is marked by the presence of scattered magnetic anomalies corresponding to oceanic plateaus (Fig. 4.12). In the north, from the southern base of Greenland to the western coast of Iceland, (12), a positive anomaly of moderate intensity is observed that extends beyond the eastern coast of Iceland until the Faeroe-Rockall plateau, (13). Over the Faeroe-Rockall plateau lies an intense negative anomaly and over its southern edge, (14), a strong positive anomaly is observed, not exactly overlying any oceanic plateau region. Further south, along the northwestern banks, (15), of West African craton, an extended positive anomaly is observed that corresponds to Madeira and East Canary plateaus. However, the shorter extent of these plateaus falls short of explaining the much larger extent of the anomaly. An anomaly of similar pattern and of the same length is observed on the western side, (16), of the north Atlantic mid-oceanic ridge axis without actually corresponding to any plateau region. Purucker et al. (1998) attributed these patterns to the Cretaceous Quiet Zones (KQZ). In the south Atlantic, two major anomalies mark their presence, one is over the Walvis ridge, (17), off the western coast of Central-South Africa and the other is over the eastern edge of North Scotia ridge, (18), off the coast of Falkland Islands, South America. Further south, flanking the 0 degree meridian, off the coast of Antarctica, lies a large elongated anomaly that partly overlies the Maud rise, (19), and the rest of it extends beyond the present known subsurface geological boundary of Maud rise.

Following a similar methodology as for the Pacific region, the oceanic plateaus in the Atlantic Ocean are modelled and a vertical field magnetic anomaly map is computed (Fig 4.12). The predicted anomaly between the southeastern region of Greenland and the eastern coast of Iceland does not agree with observations. An intense positive anomaly is predicted over Iceland, not in agreement with observations. The surplus anomaly observed over the Iceland needs further investigation. Further south, over the southern edge of Rockall plateau an anomaly is seen in the *initial model* map but the anomaly appears shifted further south. Positive anomaly corresponding to Madeira and East Canary Islands, off the coast of West African craton, agrees well with the observed map although a part of the southern half of the anomaly is not reproduced. Anomalies corresponding to magnetic highs and lows observed parallel to the North Atlantic mid-oceanic ridges are not reproduced due to the absence of oceanic plateaus in these regions. Hence, they were not modelled. In the south Atlantic Ocean, the anomaly off the coast of mid-south African continent, over the Walvis ridge, is reproduced well, although a part of the amplitude is yet unaccounted for. The same situation holds for the anomaly pattern over the eastern edge of North Scotia ridge, South America. An anomaly over the Maud Rise is also not reproduced in the *initial model* anomaly map.

The Indian ocean (Fig. 4.12) is littered with anomalies of all shapes, mainly overlying the oceanic plateaus and dismembered bodies created as a result of Gondwana breakup.

Prominent negative anomaly is observed over the Agulhas plateau, (20), at the southern coast of Africa, which extends further north along the Mozambique ridge, (21), and continues over the Madagascar plateau, (22). Further south, two small oval-shaped anomalies are seen over the Conrad rise, (23), and Crozet plateau, (24). Southeast of these plateaus lies the great elongated Kerguelen-Gaussberg ridge, (25), which is also associated with a strong negative anomaly. Sharing the same origin as the Kerguelen ridge is the Broken ridge, (26), that now lie on the northern side of the mid-oceanic ridge, off the western coast of Australia. An intense negative anomaly can be observed over it. The anomaly pattern, however, follow the series of plateaus that extend up to the Naturliste plateau, (27), just at the coast of southwest Australia. There is no anomaly observed at satellite altitude corresponding to the 90 East ridge, (28), and the Laccadive ridges, (29), off the south of Indian peninsula.

The *initial model* vertical field anomaly map for the Indian Ocean is shown in Figure (4.13) and the susceptibility distribution is shown in Appendix XII. A large number of significant anomaly patterns are reproduced. The anomaly over the Agulhas and the Mozambique plateau is reproduced well but a strong negative anomaly is observed over the Madagascar rise, moderately higher in amplitude than the observations for the same region. Also noticeable is the anomaly extent, continuing unterminated from the Mozambique plateau to the Madagascar rise in the observed map. This is absent in the predicted map. The anomaly over the Conrad rise and Crozet plateau agrees with the observations and so does the anomaly over the elongated Kerguelen plateau. However, a part of the predicted anomaly over the northern portion of Kerguelen plateau does not agree with observations. The large anomaly over the Broken ridge agrees well with the observed map but much of the positive anomaly south of it is not produced. Furthermore, the meandering anomaly pattern, off the southwest coast of Australia, is not reproduced, nor can an anomaly be seen over the Naturliste plateau.

The Arctic Ocean (Fig. 4.12) is marked by the presence of a very large and strong positive anomaly associated with the Alpha ridge, (30), just north of Greenland. The Alpha ridge (Jackson and Johnson, 1986; Weber, 1986) is generally considered to be of oceanic origin (Forsyth et al., 1986a, 1986b). However, the work of King et al. (1964) and Taylor (1983) suggests it to be a continental fragment and the dispute is yet unresolved. The anomaly located north of Canada, (31), is an intense negative anomaly and corresponds to Canada Basin. The region of Kara Sea, (32), is largely non-magnetic. However, an anomaly, (33), is observed north of Taimyr fold belts, between Novaya Zemlya and Severnaya Zemlya Islands. The anomaly could be due to the submerged Kara massif, which is composed of crystalline Precambrian rocks covered by Paleozoic sediments (Khain, 1985).

The plateaus in the Arctic region are modelled and the corresponding computed vertical field magnetic anomaly map is shown in Figure (4.13). The predicted anomaly map agrees well with the observed map as a whole. The intense positive anomaly over the Alpha ridge is reproduced very well; even the shape of the anomaly is in almost total agreement except for a small bulge at the southern edge of the anomaly. The anomaly over the Canada Basin also matches well with the observed map. The anomaly pattern

over the Kara Sea appears largely non-magnetic in agreement with the observations. A strong high observed over the northern coast of Taimyr fold belt is, however, absent from the predicted map. Hence, further investigations are required in order to identify the source of the anomaly.

I have described the modelling results for the major magnetic anomalies patterns observed over the diverse geology of the continental region, over the more uniform oceanic crust and over the poorly known oceanic plateaus. Definitely, some predicted anomaly patterns agree with the observed anomaly map while at other regions there is disagreement with the observations. Based on these results, our efforts would now be to find the sources for the anomalies that are in disagreement with the observed anomaly map. Over the continents, only 29% of Precambrian rocks are exposed, while the rest of the regions are buried by younger Phanerozoic cover. Thus, using the present flexible modelling procedure that allows us to modify the boundary of a geological unit, our efforts are to trace the possible extension of Precambrian units underlying the young cover and to provide answers to some of the key issues of global crustal field modelling. The following chapter will concentrate on some of such selected regions that have not been explained by our *initial model* but require further investigation to find the sources for the missing anomalies of the predicted map. Over the oceanic region, the presently known subsurface geology and its composition especially for some plateaus, is inadequate to explain some of the anomaly patterns. This would need further investigation to sort out the problems over the oceanic region. However, the present work does not pursue further the anomaly patterns over the oceanic regions but concentrates on modelling the anomalies over the continental region.

Chapter 5

Implications for Geology

The sources of the continental magnetic anomalies primarily consist of rock types formed early in the geological history of the earth. A glance at the observed magnetic anomaly map and the geological map of the world clearly points to the fact that most of the anomalies lie over the geological regions Precambrian in age. However, the exposed Precambrian rocks constitute only 29% of the total Precambrian crust (Goodwin, 1991). This means that a significant portion of the oldest crust on Earth is overlain by Phanerozoic cover. Hence, our aim is to look for the possible extensions of the Precambrian units obscured by younger cover and add to the existing information on geological boundaries of the Precambrian units. For this purpose, it is necessary to first consider the known geology of the region and its boundaries at the surface. Subsequently, using our modelling procedure, the vertical field anomaly map is computed for the region and compared with the corresponding region of the CHAMP magnetic anomaly map. The next step is to modify the boundary of the region and to recompute the anomaly map until a reasonable fit is achieved with the observed anomaly map. The modelling results are presented for some of the provinces of the world that have a distinct magnetic signature but are largely buried under Phanerozoic cover. The provinces (1-6) considered for detailed analysis are shown in the World geological map (CGMW, 2000) (Fig. 5.1a) and in *initial model* vertical field magnetic anomaly map (Fig. 5.1b) as white rectangles.

These six regions are chosen due to the particular tectonic settings, which causes these anomalies. The anomaly at Kentucky-Tennessee region(1), North America, is due to mid Proterozoic anorogenic magmatic activity. The granite and anorthosite massifs so abundant in this province are produced by partial melting of the lower crust. Thus, it would be interesting to map the areal extent of this magmatic activity as the region is largely buried under Phanerozoic cover. The next region of our study is Greenland(2). Largely buried under ice, without much information about its central region, it would be interesting to infer the rock types based on the observed magnetic anomaly map. The next region for our investigation is west and central Africa. The investigation of the thickness of magnetic crust below the West African craton(3) is carried out. In central Africa, over the Bangui region(4), there is disagreement between the predicted and observed magnetic anomaly map. By further study, the composition of lower crust is inferred from the intensity of the observed magnetic anomaly pattern in the region. Geological units in the eastern region of Siberia comprises mostly of accreted regions (Fujita, 1978, Churkin and Trexler, 1980), including the Kolyma and Omolon blocks(5). During the early Jurassic,
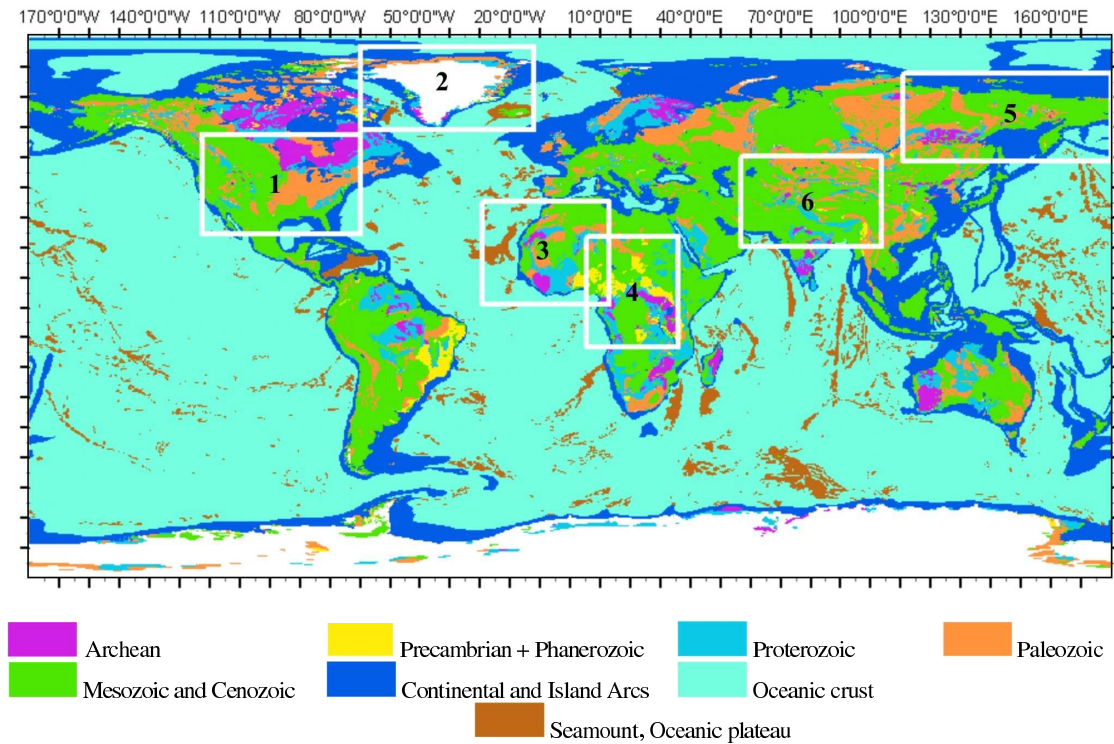
Fig. 5.1a. World geological map (CGMW, 2000). The white rectangles show the areas to be studied in this chapter.
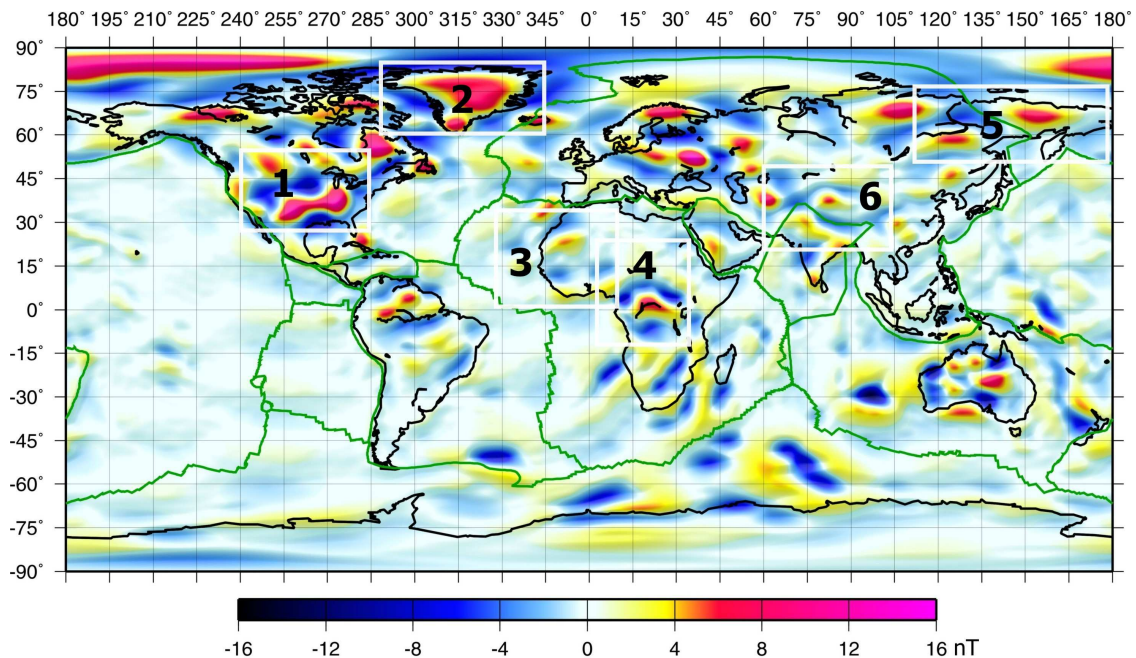
Fig 5.1b. *Initial model* vertical field anomaly map for spherical harmonic degrees 16-80 at an altitude of 400 km shown in cylindrical equidistant projection.

Chukotsk block collided with East Siberia, deforming both these blocks and caused the formation of Cherskiy suture zone. The deformation of the Kolyma block in particular,

during the continent-continent type collision that lasted till early Tertiary is investigated in detail here. Finally, the extension of basement of a rigid block on the Cathaysian plate, the Tarim craton(6), is studied. At the center of the craton lie the Archean rocks, and rocks of early and late Proterozoic ages surround them. Here, I investigate in detail, whether the Archean rocks extend below these Proterozoic rocks or not.

5.1 Kentucky-Tennessee region, North America

Central Province (Belt) is a large structural province, which underlies the south-central USA, occupying the southern portion of the North American craton. The rocks of this province are exposed only in a few places in Colorado and California. Large anorogenic magmatic activity is dominant along the entire stretch of this province (Goodwin, 1991). Figure (5.2) shows the tectonic boundary of this province as envisaged by Anderson (1983), inferred from anorogenic granite intrusions in the upper crust. The granites and associated anorthosites in this province are of two ages, flanking the eastern and the western halves. Major subprovinces of 1.34-1.40 Ga and 1.42-1.50 Ga granites occur in these two halves (Fig. 5.2). Geochemically, these anorogenic granites are A-type granites enriched in K and Fe and depleted in Ca, Mg and Sr. This means A-type granites are more magnetic relative to I- and S-type granitic bodies (Ishihara, 1977; 1987). The composition of granites suggest an origin in the lower crust (25-35 km) and are produced by partial melting of lower crustal rocks of intermediate or mafic composition (Condie, 1978).
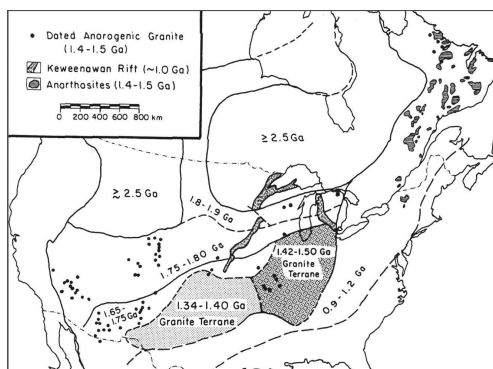
Fig. 5.2. Distribution of major Mid-Proterozoic anorogenic granites and anorthosites in North America. (Anderson, 1983).
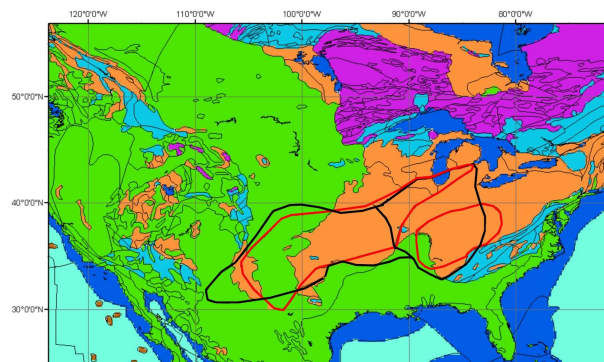
Fig. 5.3. The geological map of the southwest USA region. Thick black line is the previous boundary and the red line marks the new boundary.

The presumed present extent of the boundary (Anderson, 1983) of this buried mid-Proterozoic province is taken as input to the GIS based model. The modelling steps are described in chapter 2, where the initial VIS model is derived. The initial vertical field over the mid-Proterozoic province, southwest USA (Fig. 5.1b), shows an apparent mismatch in the extent of the predicted anomaly as compared to the observed anomaly pattern in Figure (5.4b). The predicted anomaly over the southwestern region of the province extend beyond the boundary defined by the observed map. Over the eastern region of the mid-Proterozoic province, the predicted anomaly extends up to the base of Lake Michigan. This differs significantly from the observed map, which shows an oval-

70

shaped positive anomaly only over the Kentucky-Tennessee region. Obviously, the extension of the mid-Proterozoic anorogenic region needs to be redefined.

Figure (5.4a) shows the predicted vertical field anomaly after the boundary of the granitic intrusion was refined in the location where it is most intense and occupies almost the entire crust. This refined model is called *first iteration* model. The redefined boundary is marked with a red line in the geological map of the southwest USA (Fig 5.3). The observed (Fig. 5.4b) and the *first iteration* model are now in better agreement. The oval at the Kentucky-Tennessee region is reproduced accurately. The anomaly pattern over the southwest of the province agrees well. The extension of the predicted anomaly in the northeast direction following up to the base of the Lake Michigan, however, is only partially reproduced. The *first iteration* model results indicate that the granitic intrusion may not occupy the entire crustal column especially in the western flank of the anomaly pattern. In the region between (-90^0)-(-100^0) of the mid-Proterozoic province, the granitic intrusion does not fill the lower 2.0 km of the crustal section while in the region west of -100^0 longitude unoccupied thickness of the intrusion is 5.0 km. Thus the thickness of intruded granites becomes thinner towards the west of the anomaly pattern. Recent results from Purucker et al. (2002) for the North American craton using the a priori model comprising both induced and remanent magnetisation as the source also showed good agreement with the observed anomaly map derived using the Ørsted satellite data. They concluded that remanence may not be important for modelling the continental anomalies and that induced magnetisation can explain the observed magnetic anomaly patterns.

Fig. 5.4a. *First iteration* (predicted) vertical field anomaly map for spherical harmonic degrees 16-80 at an altitude of 400 km following the boundary of mid-Proterozoic province shown in Fig.5.2.

Fig. 5.4b. Observed vertical field anomaly map for spherical harmonic degrees 16-80 at an altitude of 400 km for the southwest USA region. Line AA' show the profile section.

Figure (5.5) shows the profile along the marked section AA' extracted from the observed map, and from the *initial model* and *first iteration* predictions. The profile allow for a better comparison of the amplitude of the anomalies.
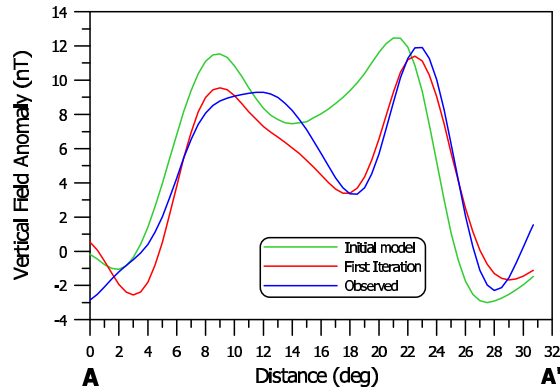
Fig. 5.5. Profile section along AA', shown for *initial model* (green line), *first iteration* (red line), and the observed anomaly (blue line) map.

5.2 North-Greenland, Greenland

The observed vertical field anomaly map of northern Greenland (Fig. 5.8b) clearly shows a disagreement with the *initial model* map for the same region (5.1b). A large anomaly predicted for the central portion of Greenland is not present in the observed map. The observations show a linear trend in the E-W direction across the center of northern Greenland. This discrepancy cannot be resolved easily because more than 90% of Greenland is under a cover of thick ice, obscuring the geology beneath it. Nevertheless, some recent geophysical studies over central Greenland have provided new insights into the nature of the crust below the ice cover. Our efforts here would be to use some of these results to improve our *initial model* and possibly try to explain a possible geological situation that could be a source of the anomaly observed.
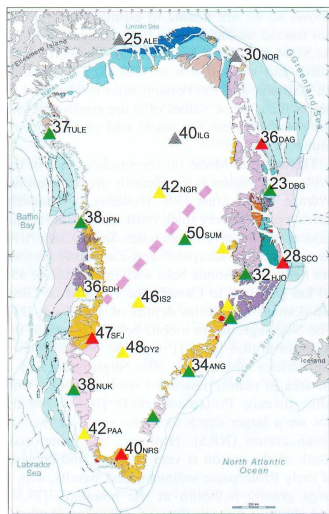
Fig. 5.6. Depths to Moho in km for all the stations in the map of Greenland. The suggested division of the Proterozoic part of Greenland is marked in pink (Dahl-Jensen, 2003).
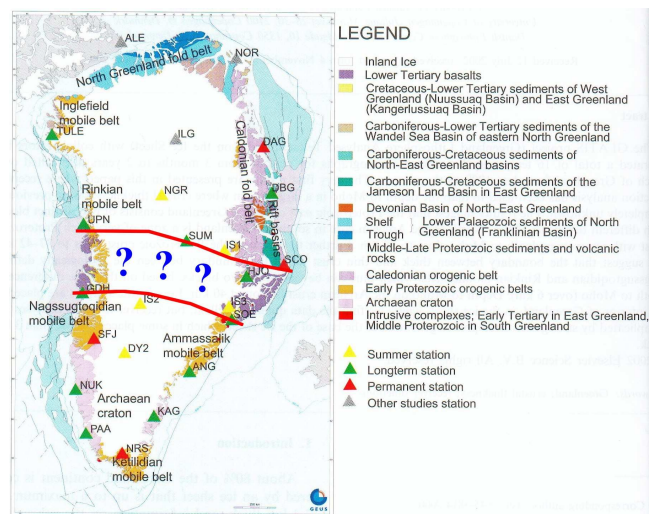
Fig. 5.7. Geological map of Greenland (Henriksen, 2000). The region marked in red line is the possible plume passage and symbol '?' suggests that it has not been proved (Wölbern et al., 2001).

72

The recent seismic results of Dahl-Jensen (2003), show the crustal thickness variations for entire Greenland (Fig. 5.6). However, the more interesting information that came out of their work is the delineation of the boundary that separates the northern and southern Greenland blocks of different Proterozoic ages. This boundary separating these northern and southern blocks runs from the western flank of Naggastoquidian belt in a northeast direction and terminates before reaching the eastern coast of Greenland (Fig. 5.6). The numbers in Figure (5.6) are depths to Moho at various stations across Greenland. The geological map of Greenland (Henriksen, 2000) is shown in Figure (5.7). Taking this new seismic model and assuming the block south of this boundary to have a lower susceptibility (0.0204 SI) than the upper block (0.0404 SI), the *initial model* is modified. The resulting *first iteration* VIS model predicts the vertical field anomaly map shown in Figure (5.8a) and is to be compared with the observed vertical field magnetic map (Fig. 5.8b).

The resulting *first iteration* model shows a better-constrained anomaly pattern over north Greenland. The elongated anomaly feature trending east-west in the observed map, however, is only partially reproduced in the predicted map. The amplitudes of the anomaly for *initial model*, *first iteration* model and the observed map along the profile sections AA' and BB' are shown in the Figure (5.9). The amplitude of the *first iteration* anomaly exceeds the amplitude of the observed anomaly amplitude by 1-2 nT. The *first iteration* model for Greenland shows that there may exist a boundary separating the two blocks having different composition. Due to unavailability of rock samples from the central region of Greenland, the study of rocks exposed at both the eastern and western coast of central Greenland could provide a clue.

Fig. 5.8a. *First iteration* (predicted) vertical field anomaly map for spherical harmonic degrees 16-80 at an altitude of 400 km for Greenland.

Fig. 5.8b. Observed vertical field anomaly map for spherical harmonic degrees 16-80 at an altitude of 400 km for Greenland. Lines AA' and BB' show the profile sections.

Wölbern et al. (2001) conducted such a study to investigate a possible passage of the Iceland plume below central Greenland. It is known that extensive flood basalts occupy both the eastern and western coast of central Greenland. The flood basalts are generally

an outpouring after the passage of a plume beneath a geological region. Wölbern et al. (2001), through receiver function analysis, however, could not find a signature related to a plume in '410 discontinuity' but could see some signatures at '660 discontinuity'. The work did not quite prove the existence of a plume passage in the geological past. However, assuming that such a phenomenon might have happened, the modelling work of Arkani-Hamed and Strangway (1985b) showed that, a heat source like a plume could cause a demagnetisation of the lower crust. This could be a possibility in central Greenland. The consequence being that the Proterozoic block south of the boundary would be less magnetic than the northern block. Indeed, such a geological setup, as has been modeled above, shows a significant improvement in predicting the anomaly over the region.

Fig. 5.9. Profile sections along AA' and BB', shown for *initial model* (green line), *First iteration* (red line), and the observed anomaly (blue line) map.

5.3 West African craton, West Africa

In the African continent, the patterns of the anomalies over the West African craton and the Bangui region are fairly well predicted, but the amplitudes fall short of the observed amplitudes. Detailed investigation is carried out to explain the large observed anomaly over these regions.

Fig. 5.10. The geological map of the West African region. Thick black line is the previous boundary and the red line marks the new boundary.

Fig. 5.11. The geological map of the West African region (Goodwin, 1991).

74

In the West African craton, the Archean rocks of Amsaga belts of the Reguibat shield in the north and the Liberian shield in the south, including the exposed Kasila series, is composed of mafic rock constituents (Goodwin, 1991). The VIS value for these regions is shown in Appendix (VI). The observed anomaly map (Fig. 5.12b) shows a band of negative anomaly that extends over the Liberian shield with a strong positive observed over the Kasila series. A positive anomaly of high amplitude is observed over the western Taoudeni basin south of Amsaga Archean belt. The predicted anomaly map (Fig. 5.1b) does reproduce the anomaly pattern; a high over the Taoudeni basin flanked by low anomaly on either side but fails to reproduce the strong amplitude. Even the extension of anomaly over the Taoudeni Basin is not seen in the predicted map.

Fig. 5.12a. *First iteration* (predicted) vertical field anomaly map for spherical harmonic degrees 16-80 at an altitude of 400 km for West African region.

Fig. 5.12b. Observed vertical field anomaly map for spherical harmonic degrees 16-80 at an altitude of 400 km for West African region. Line AA' show the profile section.

To account for the missing amplitude, the VIS model is reinvestigated to find the source of the strong observed anomaly. The crustal thickness variation defined by 3SMAC model and used in the *initial model* underestimates the thickness of Archean crust in the West African cratonic region. The 3SMAC thickness of Amsaga Archean belt is 32-35 km and for the Liberian shield is 30-33 km, while the crustal thickness for a typical Archean unit is 40-42 km in most of the regions of the world. In South Africa, it is 35-45 km, (Nguuri, 2001). Toft and Haggerty (1988) even claim that the crust in the south of the West African craton is 70 km thick. The temperature distribution at a depth of 50 km, using heat flow data (Artemieva and Mooney, 2001), also shows that the Curie-isotherm is still deeper in this region. Accounting for the above reported results for the thickness of an Archean crust and for the West African craton in general, the crustal thickness of Amsaga belt and Liberian shield is increased by 8.0 km. The geological map for the West African craton region is shown in Figure (5.10), which shows the new extension of Amsaga belt in red line. Geological units of the West African region are shown in Figure

(5.11). The VIS model is recomputed using the above parameters and the vertical field anomaly map is computed. The *first iteration* map is shown in Figure (5.12a) and the corresponding observed anomaly map in Figure (5.12b). The predicted map shows the anomaly pattern over the West African craton to agree well with the observations. The anomaly over the western Taudeni basin also matches well with the observed anomaly map. The profile across the craton (Fig. 5.13) shows a comparison of the observed anomaly with the initial and *first iteration* model. Amplitude amounting to 1.8-2.4 nT is yet unaccounted for, especially over the shield regions. These results may point to magnetisation extending into the upper mantle, in agreement with results of Toft and Haggerty (1988).

Fig. 5.13 Profile section along AA', shown for *initial model* (green line), *First iteration* (red line), and the Observed anomaly (blue line) map.

5.4 Bangui anomaly, Central Africa

In the Central African region (Fig. 5.14), the region north of Congo craton witnessed Pan-African orogeny (800-530 Ma) that resulted in the intrusion of Oubanguides in the region north of Bangui where it is exposed and along the entire stretch north of Congo craton (Pin and Poidevin, 1987). Figure (5.15) shows the distribution of granulites of the northern part of Congo craton. The high content of iron oxides in two of the three samples showed that they could only be derived from a more mafic parental magma (Clark, 1999). However, the bulk susceptibility of the rock types exposed in the region (Appendix VI) falls short of the total susceptibility required to reproduce the Bangui anomaly. To account for the shortfall in susceptibility, the composition of the lower crust needs to be modified in the model, considering it to be of a more mafic composition than inferred on the basis of surface geology. Emplacement of basalts in the lower crust as a result of Pan-African orogeny is a possibility.

Considering basalts in the lower crust and an additional 4 km of basalts in the upper crust, the computation of VIS in the region north of Congo craton is redone. The vertical field anomaly map is predicted (Fig. 5.16a) and compared with the observed anomaly map (Fig. 5.16b). The *first iteration* magnetic anomaly map for the region now is able to account for most of the missing anomaly. The profile BB' across the anomaly (Fig. 5.17) shows a much better agreement in amplitude with the anomaly in the northern half over Bangui. Over the southern lobe of the anomaly pattern some part of anomaly is yet unaccounted for. This suggests a more mafic composition of the lower crust below Bangui and a more felsic lower crust below Congo craton. A deeper Curie-Isotherm

76
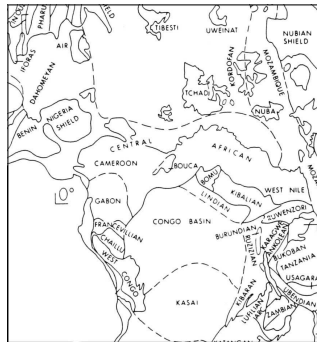
Fig. 5.14. Geological map of the Central African region (Goodwin, 1991).
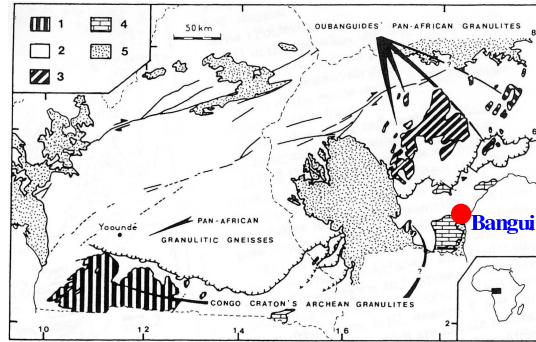
Fig. 5.15. Granulites distribution of the northern part of Congo Craton (Pin and Poidevin, 1987). 1. Archean granulites; 2. Undifferentiated Precambrian formations; 3. Pan-African granulites; 4. Sedimentary upper Precambrian foreland of Oubanguides; 5. Post Pan-African cover.
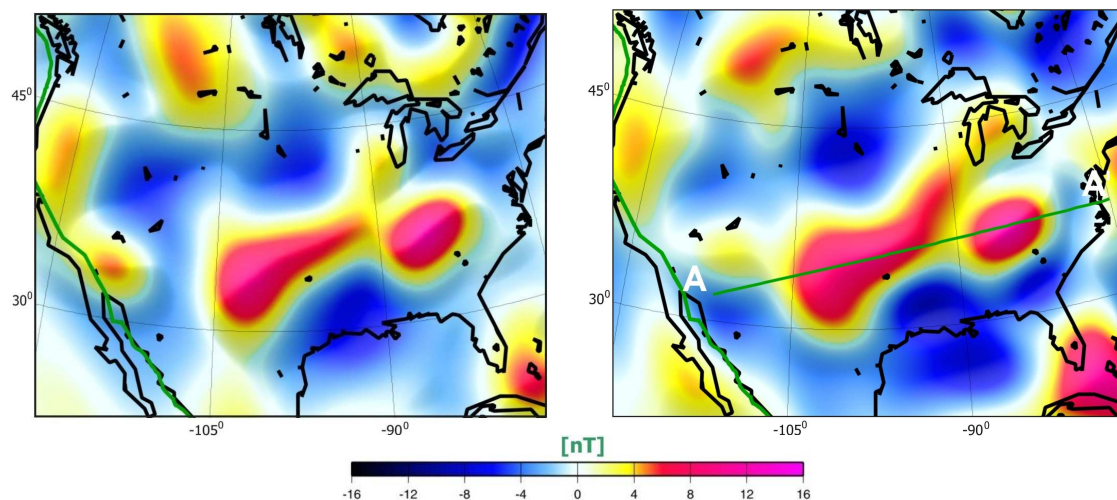

Fig. 5.16a. *First iteration* (predicted) vertical field anomaly map for spherical harmonic degrees 16-80 at an altitude of 400 km for Central African region.

Fig. 5.16b. Observed vertical field anomaly map for spherical harmonic degrees 16-80 at an altitude of 400 km for Central African region. Line BB' show the profile section.
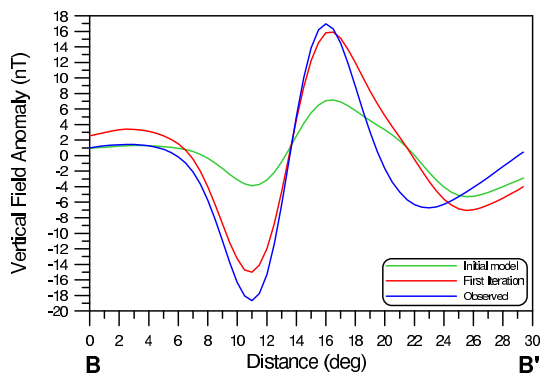
Fig. 5.17 Profile section along BB', shown for *initial model* (green line), *First iteration* (red line), and the observed anomaly (blue line) map.

77

below Bangui in the northern region and an elevated Curie-Isotherm beneath Congo craton could also possibly account for the missing amplitudes. Indeed, the temperature distribution map at the depth of 50 km prepared by Artemieva and Mooney (2001) supports this argument. Our results are in agreement with Regan and Marsh (1982) who considered the source to be geological and modeled the anomaly by assuming the entire crust below Bangui to be of higher susceptibility (0.01 cgs units) than the surrounding. Ravat et al. (1989) modelled the Bangui anomaly by considering a block of 3.0 km thick of susceptibility 1.0 SI which could be unusually high. The upper crust of the surrounding region was considered felsic while the lower crust was considered more mafic. Girdler et al. (1992) proposed an iron meteorite as the source of the Bangui anomaly.

5.5 Kolyma-Omolon block, Siberia

The region of Kolyma-Omolon block is mostly buried, apart from a few outcrops along the Cherskiy suture zone. The tectonic activity of the region before and after the collision of Brooks-Chukotsk block with East Siberia and West Alaska (Sweeney, 1981; Howell and Wiley, 1987) is shown in Figure (5.18a-d). The shape of Kolyma microcontinent during the early Jurassic period is shown in Figure (5.18a), which surprisingly, until early
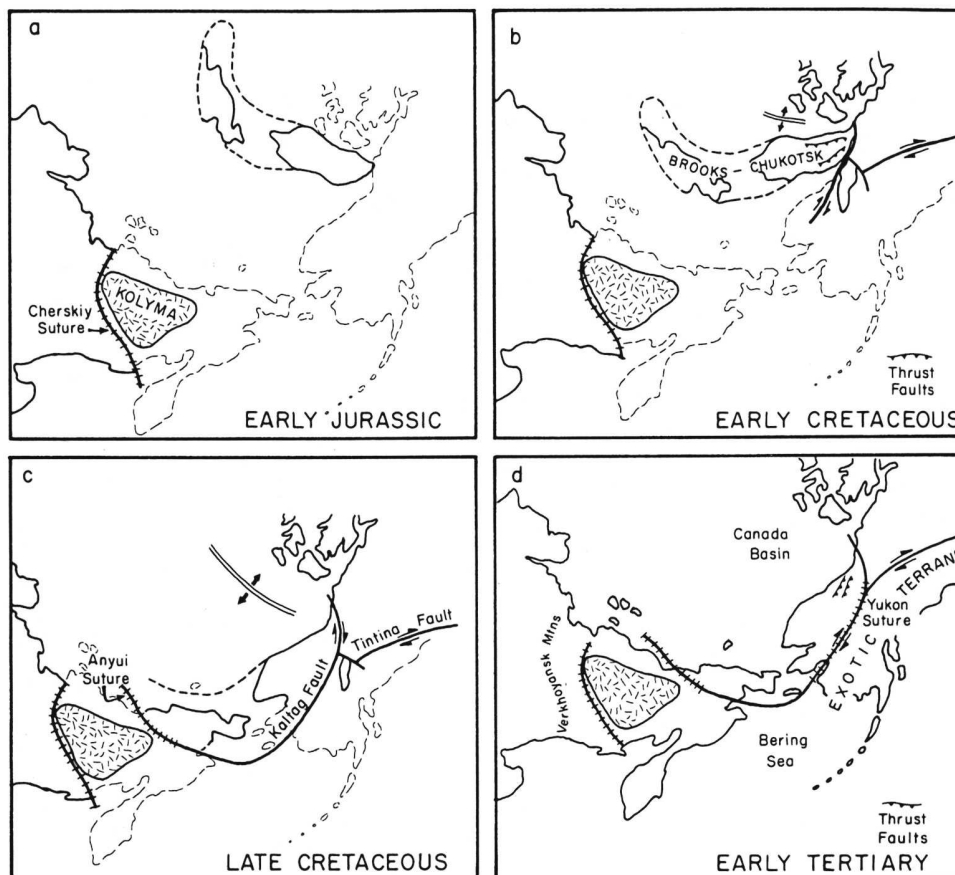
Fig. 5.18. Tectonic reconstruction of the Cordilleran Arctic region since the Early Jurassic (Sweeney, 1981, and Howell and Wiley, 1987. Diagram taken from Condie, (1989).

78

Tertiary (Fig. 5.18d) was assumed by Sweeney (1981) and Howell and Wiley (1987) to have remained the same. The *initial model* used this shape of the Kolyma block and the vertical component anomaly map was computed accordingly. Obviously, the shape of the predicted anomaly (Fig. 5.1b) did not match with the observations (Fig. 5.20b) over the Kolyma block. The observed map clearly showed an anomaly following the Cherskiy zone trending NW-SE in direction and we investigate the cause for such an anomaly pattern.
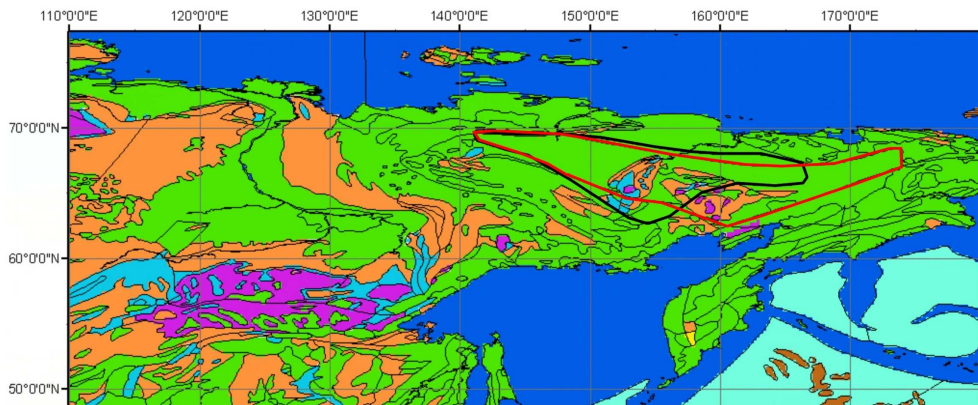
Fig. 5.19. The geological map eastern region of Siberian craton. Thick black line is the previous boundary and the red line marks the new boundary of the Kolyma block.

Keeping in view the intraplate processes that wrenched and internally rotated the Brooks-Chukotsk block on both sides of Bering Sea, it is hard to imagine that the Kolyma block would not have been deformed. Considering that during late-Cretaceous and early Tertiary era, when the Chukotsk block collided with the Kolyma block forming Anyui suture, it compressed the Kolyma block against the Cherskiy Suture zone. This also caused deformation in the Verkhoyansk fold belt located west of Kolyma. The boundary of this deformed Kolyma block, which is hidden under the Phanerozoic cover in the
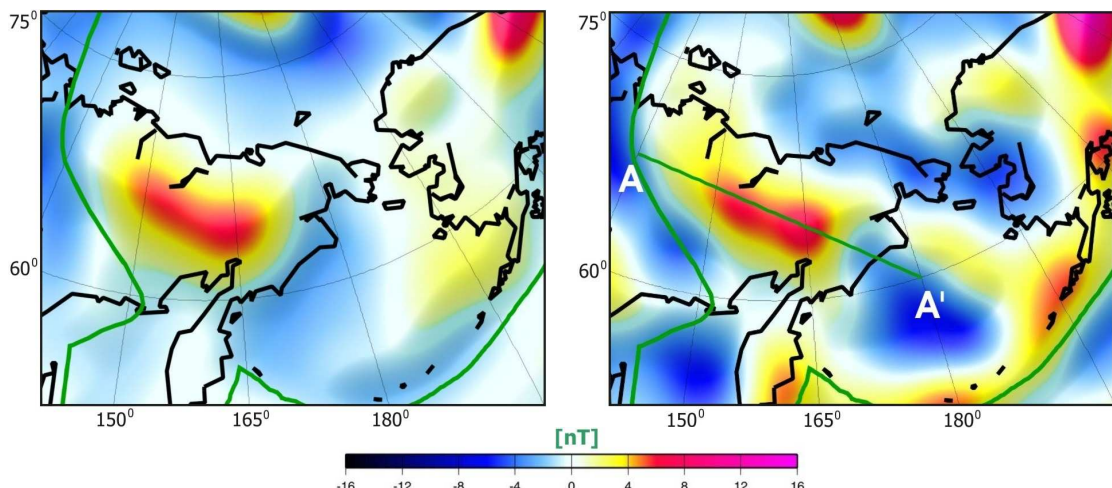
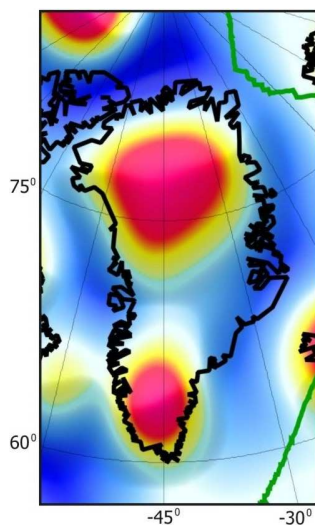Fig. 5.20a. *First iteration* (predicted) vertical field anomaly map for spherical harmonic degrees 16-80 at an altitude of 400 km for Kolyma block.
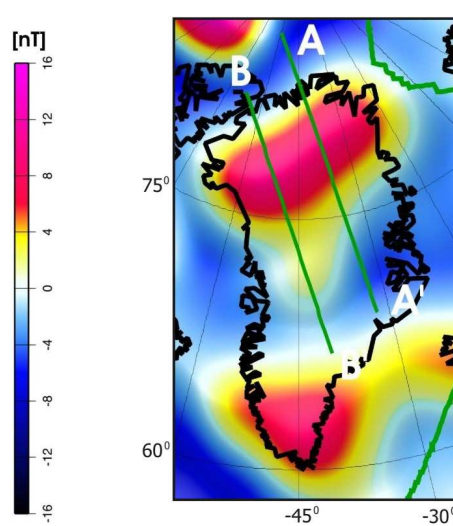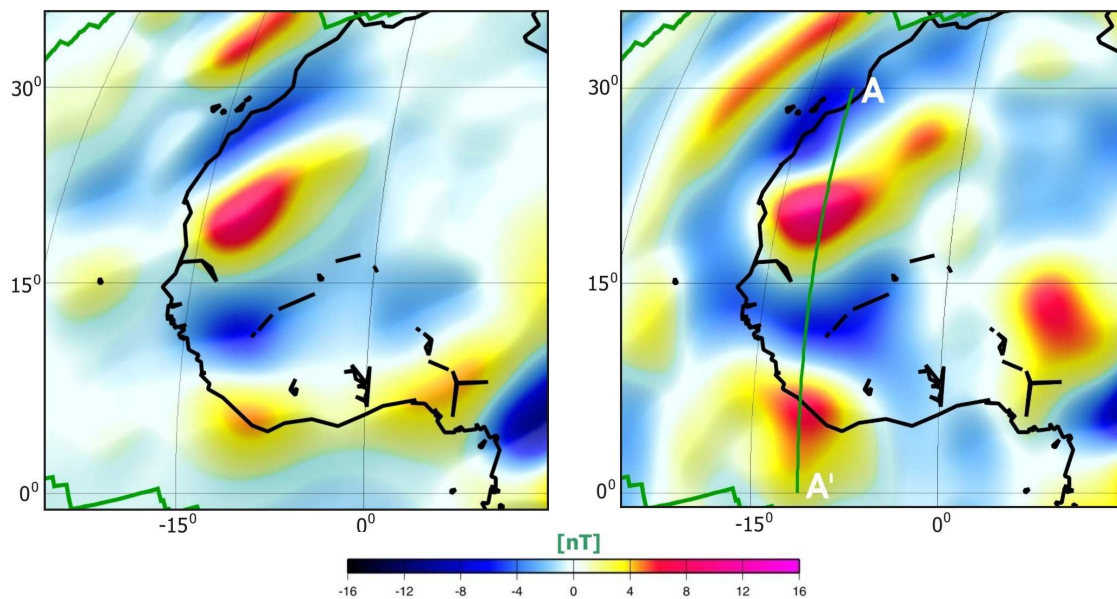
Fig. 5.20b. Observed vertical field anomaly map for spherical harmonic degrees 16-80 at an altitude of 400 km for Kolyma block.

region, is retraced following the observed anomaly pattern over the region. The new boundary is shown in red line in Figure (5.19). The VIS value for the block is recomputed and the vertical field anomaly map for the region is predicted, called the *first iteration* model (Fig. 5.20a). The anomaly associated with the new boundary of the Kolyma block now agree well with the observations (Fig. 5.20b). The profile over the region provides a numerical estimate for the observed and predicted anomaly and is shown in Figure (5.21). Thus, the magnetic anomaly study in this part of the globe demonstrates the ability of the modelling method to trace the subsurface extension of a buried and deformed block.
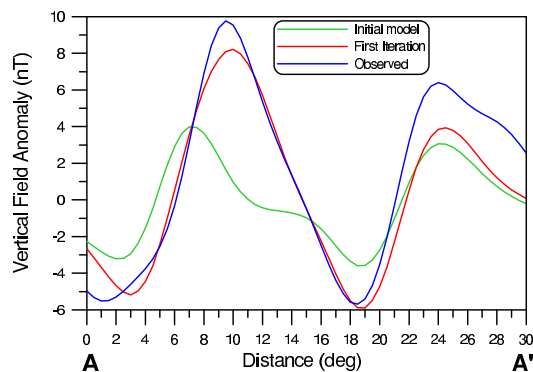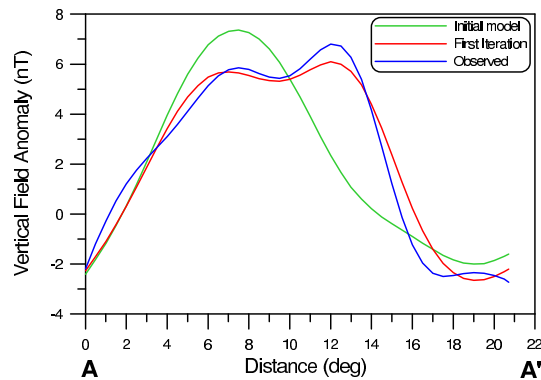

Fig. 5.21. Profile section along AA', shown for *initial model* (green line), *First iteration* (red line), and the observed anomaly (blue line) map.

5.6 Tarim basin, China

Tarim craton or basin is one of the largest rigid blocks, located in the eastern region of the Tibetan plateau. The block is so rigid that it did not get deformed during the Himalayan orogeny. Exhibiting a typical eastward tapered oval shape, and congregation of rock types of different age, a large anomaly over the entire block makes it distinctly different from other blocks of same age. The geology of the region is known only partly, especially with regard to the basement (Zhang et al., 1984) as it is exposed only at the peripheral region of the basin (Fig. 5.22). The exposed Archean rocks occupy the core of the block while a part of the northern region of the block is marked by the presence of early Proterozoic rocks. Mid Proterozoic rocks occupy the rest of the eastern tapered region of the block. Considering all the rock types exposed in the region, including the Phanerozoic sediments covering them, the VIS model is computed for the region. The *initial model* (Fig. 5.1b) predicted for the region is compared with that of the observed magnetic anomaly map (Fig. 4.3a). The anomaly from the predicted map does not match with the observations over the Tarim basin, except only over the core of the block, where the agreement is better.

It is apparent that the susceptibility contrast for the rock types exposed in the surrounding region i.e., of early Proterozoic and mid-Proterozoic is not sufficiently high to produce a strong positive anomaly observable at satellite altitude. The only way this contrast can be generated is to consider the Tarim block entirely comprising of Archean basement. Thus in our derivation of *first iteration* VIS model, the entire basement of Tarim basin is considered to be Archean. The renewed VIS model for the block is computed and the vertical field anomaly map for the Tarim basin is predicted. On comparison of the *first iteration* model (Fig. 5.23a) with the observed anomaly map (Fig. 5.23b), the predicted

anomaly over the Tarim basin is now in better agreement with the observations. The profile sections over the Tarim basin (Fig. 5.24) provide a numerical estimate of the amplitudes of the observed and predicted anomaly maps. Thus, through our modelling studies it can be inferred that the Archean rock exposed only at the core actually occupy the entire basement region of Tarim basin.
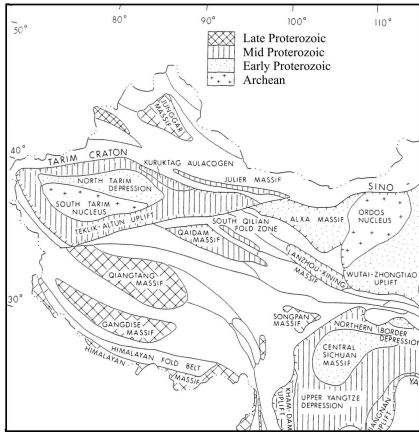
Fig. 5.22. Main outline of Tarim craton within the Cathayian craton. (Goodwin, 1991).
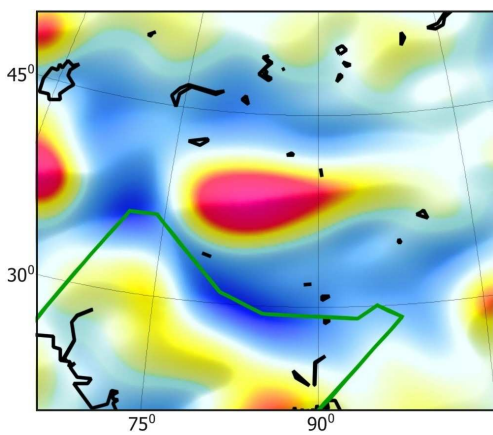
Fig. 5.23a. *First iteration* (predicted) vertical field anomaly map for spherical harmonic degrees 16-80 at an altitude of 400 km for Tarim basin.
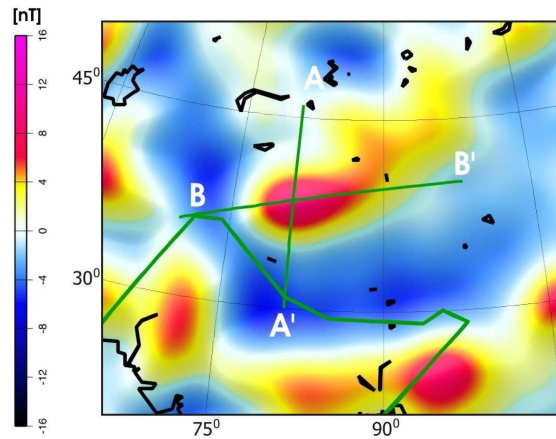
Fig. 5.23b. Observed vertical field anomaly map for spherical harmonic degrees 16-80 at an altitude of 400 km for Tarim basin.
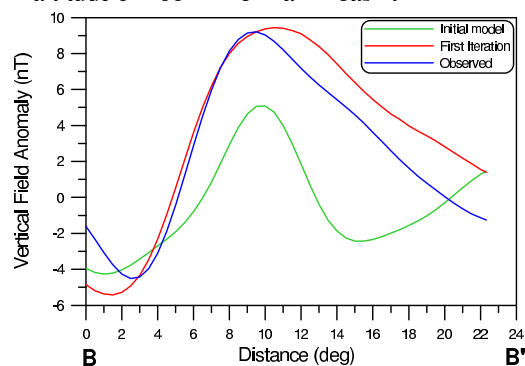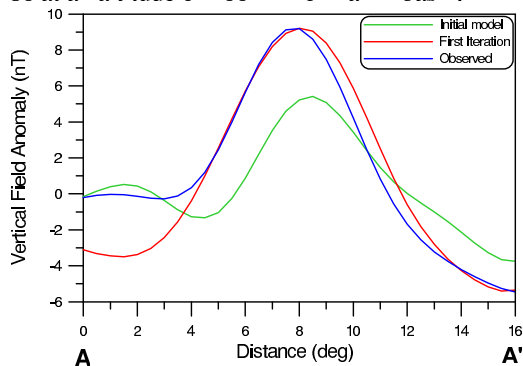
Fig. 5.24. Profile sections along AA' and BB', shown for *initial model* (green line), *first iteration* (red line), and the observed anomaly (blue line) map.

81

5.7 Global *first iteration* model

In the above sections, we studied the anorogenic magmatic activity and its areal extent, in southwest USA, probable rock types below central Greenland, thickness of crust in West Africa, composition of lower crust in Central Africa, deformation induced to Kolyma block in a continent-continent type collision and finally the extension of Archean basement below Tarim craton. The initial VIS model is modified only in these regions as the predicted anomaly did not match well with the observed anomaly map. Thus, six regions of the world are studied in detail and redefined accordingly and a *first iteration* vertically integrated susceptibility model is derived. Using this *first iteration* VIS model, the *first iteration* vertical field anomaly map is computed at an altitude of 400 km for spherical harmonic degrees 16-80. The VIS model for oceanic region has not been changed since the derivation of initial VIS model. The *first iteration* VIS model and the predicted magnetic anomaly are shown in Figure (5.25) and (5.26) respectively. A detailed comparison has already been done in all the sections above where the anomaly features have improved considerably since the derivation of *initial model*. Here the *first iteration* global magnetic anomaly map is shown for completeness and to have a global view of all the modification done in the above sections.
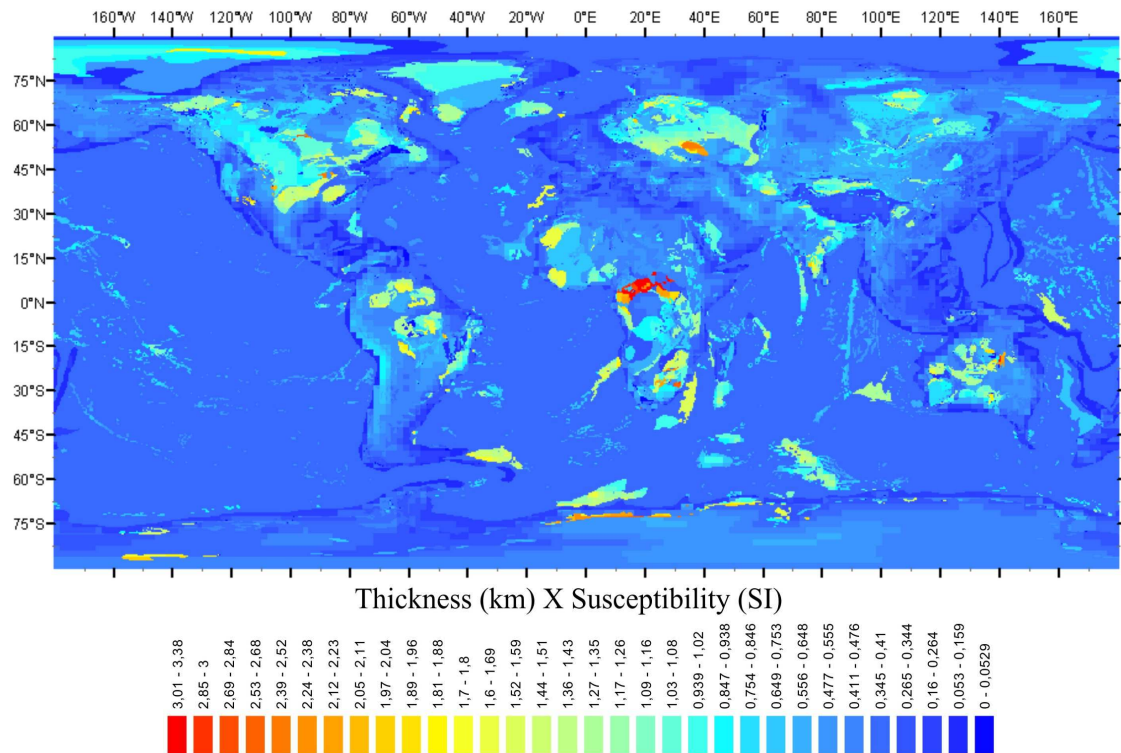
Fig. 5.25. *First iteration* VIS map of the world.

The *first iteration* vertical magnetic anomaly map shown in Figure (5.26) is shown against *initial model* vertical magnetic anomaly map (Fig. 5.27) to compare the improvements achieved after the above exercise.
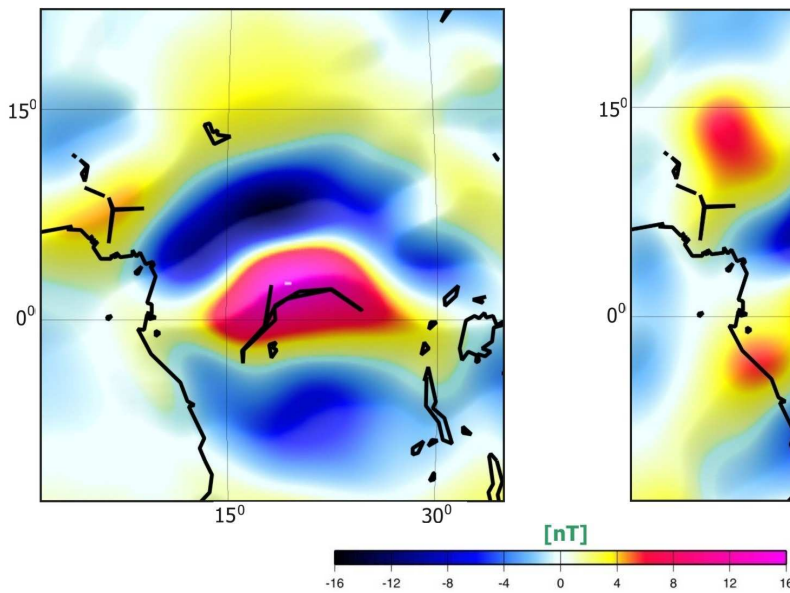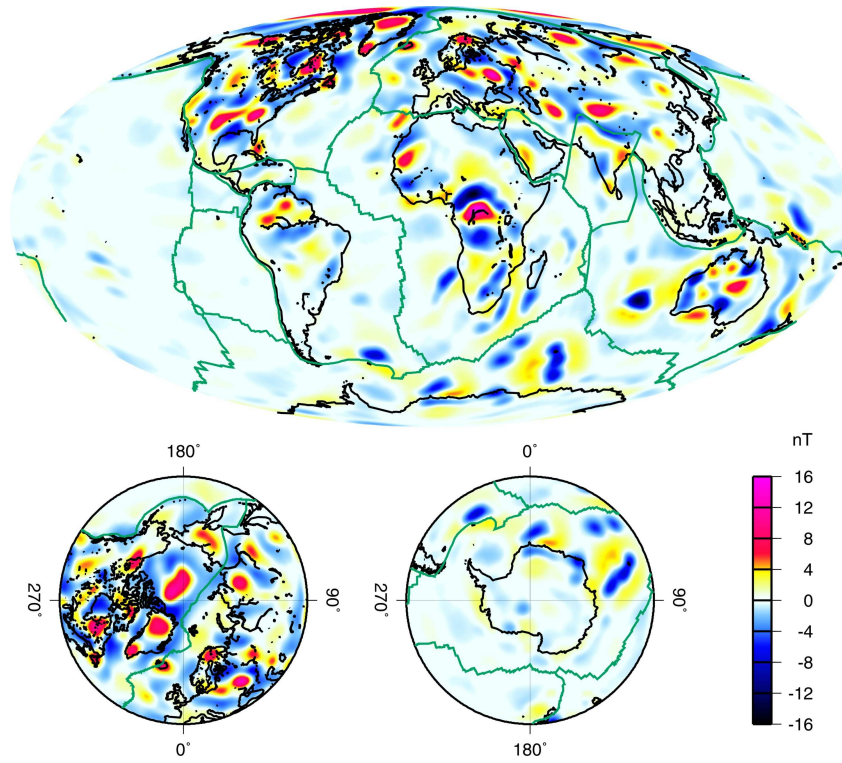
Fig. 5.26. *First iteration* vertical field anomaly map for spherical harmonic degrees 16-80 at an altitude of 400 km.
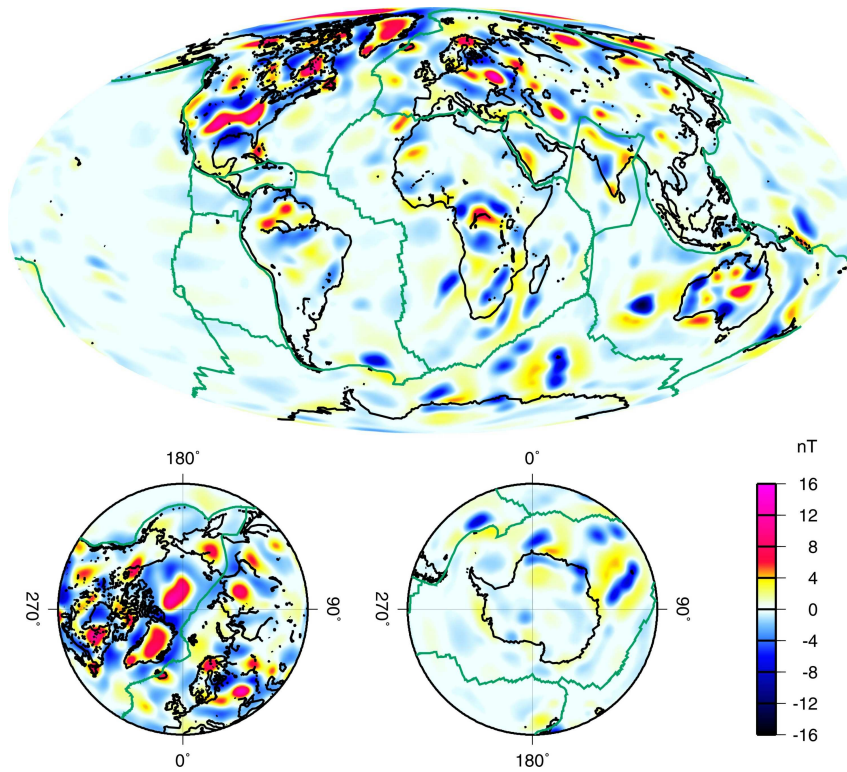
Fig. 5.27. *Initial model* vertical field anomaly map for spherical harmonic degrees 16-80 at an altitude of 400 km.

Chapter 6

Discussion

In the following subsections we would like to discuss certain key aspects related to magnetic modelling of the crust, which were omitted in the previous chapters. Curie-temperature isotherm, remanence and continent-ocean boundary contrast bear special importance while interpreting crustal field anomalies. Each of them is discussed briefly here.

6.1 Curie-temperature isotherm depth

Estimating the depth of the Curie-temperature isotherm (CTD) has been attempted from magnetic maps using either the shape of isolated magnetic anomalies (Bhattacharyya and Leu, 1977) or the patterns of magnetic anomalies (Shuey et al., 1977). Shuey et al. (1977) showed that it was not possible to obtain CTD from individual anomalies in space domain and therefore used a spectral method. Maus et al. (1997) pointed out that large survey areas are required to resolve the power at long wavelengths. They assert that a reliable estimate of the CTD cannot be obtained from an area smaller than 1000 km X 1000 km. Consequently, it could be difficult to estimate the CTD from individual aeromagnetic surveys, typically having dimensions of not more than a few hundred kilometers. A consequence of the large survey areas required is that realistic maps of the CTD will have a very low lateral resolution. It is unlikely that it is possible to resolve lateral CTD variations for distances of less than several hundred kilometers from magnetic data by spectral methods. Such CTD maps would not shed much light on geological features with strong lateral temperature variations, such as subduction zones.

In the present work, the derivation of VIS model did not include the CTD variation in the lower crust, nor any attempt has been made to estimate CTD from the observed vertical field anomaly map. Frost and Shive (1986) based on measured geothermal gradients, computed 600° C isotherm and concluded that the isotherm is above the lower crust (20 km) e.g. in the basin and range province, eastern Australia, Central Australia while in the cratons and shields the isotherm could be below the lower crust in the upper mantle. In Sierra Nevada he finds the isotherm to be at a depth of about 74 km. The assumption of the lower crust being the magnetic boundary may seem invalid in such regions. However, Wasilewski et al. (1979) found a complete absence of magnetites in mantle peridotites, and therefore concluded that the Moho is the lower magnetic boundary. In summary, we expect that the CTD is above the Moho in hot regions, while it is either identical to or

below the Moho in cold regions. Unfortunately, current temperature models are not sufficiently accurate. Arguably the most accurate model, by Artemieva and Mooney (2001), has a lateral resolution of only 10° X 10°. I therefore decided not to include a temperature model in the present model, relying on the more accurately known Moho as a lower magnetic boundary, instead.

6.2 Remanence

Total magnetisation is the vector sum of induced and remanent magnetisation. Thus, it is important to consider the remanence carried by different rock types. Two types of remanence are discussed here, stable and viscous. Some rocks have stable remanence acquired when the rocks cooled to below the blocking temperature of their minerals. This magnetisation is acquired in a direction parallel to the Earth's magnetic field during cooling, which may be different from the present direction of the field because of geomagnetic field reversals in the geologic past. Single-domain grain bearing rocks, like the rapidly solidified basalts, carry these remanences most effectively. However, in larger multi-domain size grains, dominant in slowly solidified and metamorphosed rocks, the stable remanence undergoes viscous decay with time. Then, the original remanence is replaced by viscous remanent magnetisation (VRM) parallel to the present field direction. For the present modelling, it is therefore not necessary to distinguish between VRM and induced magnetisation.

Stable remanence is likely to be less important in deep crustal conditions than in upper crustal conditions. Stable remanence decreases with increasing temperature and degree of metamorphosis. Stable remanence carried by both single-domain and multi-domain grains decays exponentially with time. According to Shive et al. (1992) stable remanence cannot be responsible for high magnetisation required by magnetic anomaly analyses. Treloar et al. (1986) showed through laboratory and theoretical studies that even VRM in the lower crust cannot be as great as induced magentisation. Moreover, the size of Fe-Ti oxides in lower crust is around 100 microns (Schlinger, 1985), i.e., they are not single-domain grained minerals, and hence cannot carry strong remanence. Shive (1989) and Shive et al. (1992) concluded that the total magnetisation of lower crustal rocks is not significantly greater than their induced magnetisation.

Following the above reported works it is justified not to consider remanence in our present study, which focuses on the continents. The results discussed for various continents in chapter 4 showed some disagreement of the *initial model* anomaly shapes and amplitudes with the observed magnetic anomaly map. However, reinvestigation in some regions of the world (discussed in Chapter 5) showed that assuming induced magnetisation, as the only source for the anomaly is always sufficient to explain the observed anomaly. This holds even in west Africa, though some part of the observed anomaly is yet unaccounted for. Here, either the magnetisation extends in to the upper mantle as suggested by Toft and Haggerty (1988) or the lower crust is more magnetic than has been considered in the present work. In central Africa, basalts in the lower crust and an additional 4 km of basalts in upper crust explain the observed anomaly. Thus, it was not necessary to consider remanence in the present work to explain the observed

magnetic anomaly. In summary, we have found no indication that remanence is required to explain the magnetic anomalies of continental crust. This is likely to be different for the oceanic crust.

6.3 Continent-Ocean boundary

Interpretation of satellite derived magnetic anomaly maps has always generated interest in the study of the exposed anomaly caused by the continent-ocean contrast. It is generally asserted that because continent is thicker than ocean, an anomaly should be expected at the continent-ocean boundary and should have influence on the anomalies observed further inside the continents. Some studies have tested the validity of such an assertion.

The 3D global magnetisation model derived by Arkani-Hamed and Strangway (1986a) showed distinct differences between oceanic and continental areas. Hinze et al. (1991) compiled the mean magnetic anomaly amplitude for crustal anomalies and for oceanic anomalies off the coast of South America and found a statistical increase in continental anomaly amplitude. However, a ubiquitous continent-ocean contrast was absent from magnetic anomaly maps prepared from satellite data. This means that either the vertically integrated magnetisation of oceanic crust is the same as that of continents or it has been eliminated in the process of removing the long wavelength main field. This conclusion was verified in the studies of Cohen (1989) and Counil et al. (1991) who modelled the continent-ocean boundary as a step function in susceptibility contrast. They confirmed that continent-ocean boundary is a long-wavelength feature and it is partly removed in subtracting the long wavelength main field. Forward modelling methods based on global models of Meyer et al. (1983) and Hahn et al. (1984), derived from surface geology, seismic structure, and standard susceptibilities also made an effort to study the effect of continent-ocean boundary. The modelled magnetic field, in general, did not reproduce the effect of continent-ocean boundary and they concluded that this effect might be a long wavelength feature, which has been removed while removing long wavelength part of the main field. Purucker et al. (1998) derived a magnetisation model that included a built-in first-order continent-ocean boundary effect.

In the present study, the global VIS modelling permits us to study systematically the effect of continent-ocean boundary. In chapter (1), it was shown that the observed magnetic anomaly map was derived by removing the long wavelength component from the main field. This means that main field masks the wavelengths from the crust and hence we cannot see them. But, one of the most interesting results of our modelling is that using our VIS model, which predicts the magnetic anomaly map for spherical harmonic degrees 16-80 that matches well with the corresponding degrees of the observed magnetic anomaly map, can also predict the long wavelength features of the real crustal field. As the VIS model does not include the parameters of the mantle but only the crustal part, producing the map of degrees 1-80 should show the long wavelength component of the VIS model. *First iteration* vertical field anomaly map for spherical harmonic degrees 1-80 is shown in Figure (6.1). Interestingly, there is no anomaly over the continent-ocean boundary. This means the continent-ocean boundary is

not a long wavelength feature and the absence of anomaly over the continent-ocean boundary indicates that the bulk susceptibility of the continents and oceans are comparable. Another feature that is interesting in the map is the presence of strong anomaly features at the edges of major cratons of the world. However, our model is not entirely a complete one as the observed magnetic anomaly map has possible long wavelength components from the upper mantle which our model lacks them.

Though the above result suggests the absence of effect of continent-ocean boundary, we study systematically the possible influence of continent-oceanic boundary on the anomalies that lie further inside the continents and also some observed anomalies that run parallel to the mid-oceanic ridges, e.g. north Atlantic ocean. For this, three VIS models are derived with different parameters for the oceanic region. The susceptibility distribution is shown in Table 6.1

Geological region	Model-1	Model-2	Model-3
Continent	*First iteration* VIS model	*First iteration* VIS model	*First iteration* VIS model
Ocean	0.0	*First iteration* VIS model	3 X *First iteration* VIS model

Table 6.1. The susceptibility distribution of continents and oceans to study the continent-ocean boundary effect.
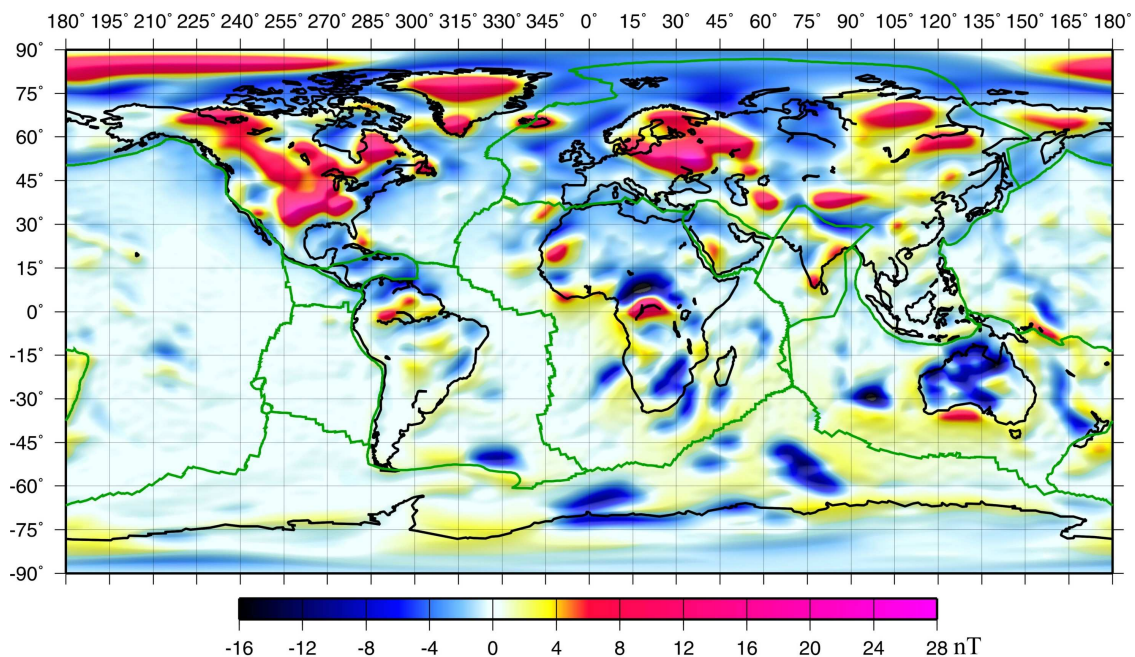
Fig. 6.1. *First iteration* vertical field anomaly map for degrees 1-80 at an altitude of 400 km.

The results for the above three VIS models are shown in Figures (6.2), (6.3) and (6.4) respectively. The predicted anomaly map for the vertical component for degrees 16-80 derived using Model-1 is shown in Figure (6.2). It predicts a few weak anomalies over the eastern boundary of the South American craton. However, largely, the effect of the continent-ocean bulk susceptibility contrast is not apparent in the map. There are some

87

regions of the world, which are influenced by the susceptibility contrast of continents and oceans. Over northern and southern Greenland the positive anomaly is enhanced. The anomaly over the Ungava craton, Canada is also stronger. In Figure (6.3) the effect of continent-ocean boundary is certainly not evident in the predicted vertical field anomaly map for degrees 16-80 derived using Model-2. There are evidently no magnetic anomaly features running parallel to the continents or the oceans, which obviously follow the predictions for the map for degrees 1-80. The predicted anomaly map as shown in Figure (6.4) for model-3 shows enhanced effect at not only the boundary of continent-ocean but also over the continents and oceans. A strong anomaly pattern is seen along the coast of the Pacific ocean. Along the western coast of North America and eastern coast of Russia and Japan, an anomaly pattern is seen. All over the western boundary of north Atlantic ocean a strong anomaly pattern is evident. Surprisingly, over the south Atlantic ocean the effect is not prominent and the same holds true for the Indian ocean. A strong effect is also observed over the coast of Antarctica.

The above results show that the bulk susceptibility contrast for continents and oceanic regions when changed does produce an anomaly at the continent-ocean boundary. There is also modification of anomalies strength and patterns further inside the continents. Absence of anomaly over the continent-ocean boundary, in the *first iteration* magnetic anomaly map both for degrees 1-80 and 16-80, shows that bulk susceptibility contrast of the continents and oceans are comparable. Our modelling result indicates that no long wavelength features related to continent-ocean boundary exist and, hence, there is only minimal effect of the continent-ocean boundary.

6.4 Oceanic plateaus

In chapter 3, the structure of the oceanic plateaus was discussed following the reported work of Carlson et al. (1980) and Nur and Ben-Avraham (1982). A simple 3-layered model was assumed to model the plateaus. The vertical component of the magnetic field was predicted for degrees 16-80 at satellite altitude and compared with the corresponding vertical component of the observed magnetic anomaly map. The results were discussed briefly for all the modelled plateaus in Chapter 4. Generally, for most of the plateaus, the assigned susceptibility values for different layers and the crustal thickness from the 3SMAC seismic model and some results taken from literature, was sufficient to explain the observed anomaly pattern. However, there are anomaly patterns, especially in south Atlantic ocean that are not explained completely on the basis of *initial model* modelling parameters.

The modelling results for the anomalies located northeast of Georgia, South America and over Maud rise, Antarctica, suggests that the crust in these regions is thicker by 10.0 km and 6.0 km respectively, than indicated by 3SMAC seismic model. Over the Walvis ridge, off the western coast of Africa, a part of the observed anomaly is yet unaccounted for, though the crustal thickness in this region has already been increased by 8.0 km over
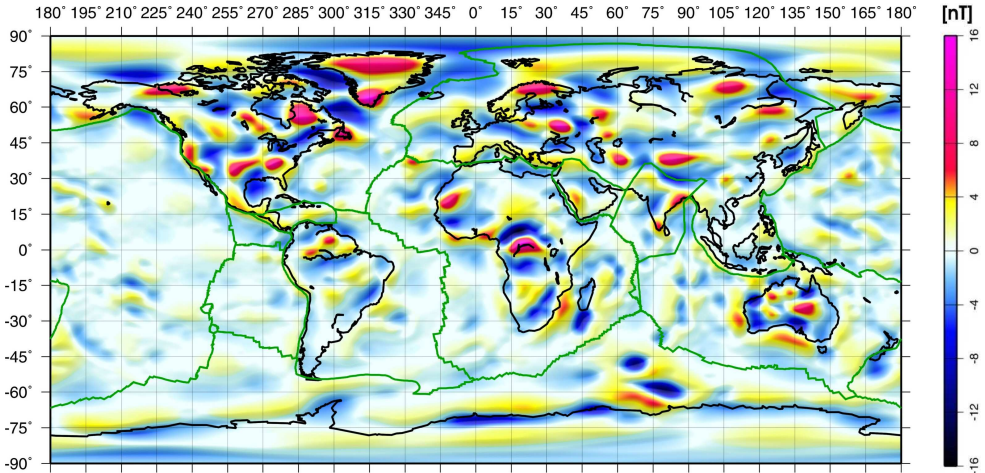
Fig. 6.2. *First iteration* vertical field anomaly map for degrees 16-80 predicted for Model-1, at an altitude of 400 km.
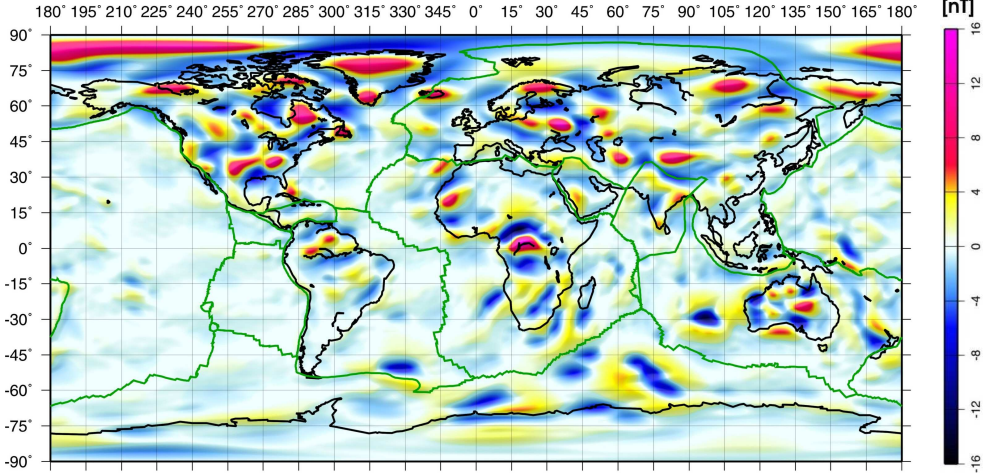
Fig. 6.3. *First iteration* vertical field anomaly map for degrees 16-80 predicted for Model-2, at an altitude of 400 km.
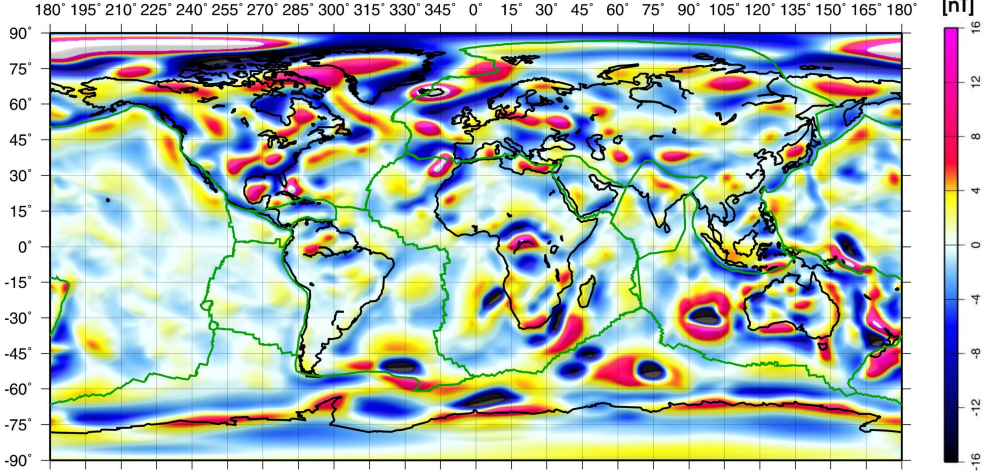
Fig. 6.4. *First iteration* vertical field anomaly map for degrees 16-80 predicted for Model-3, at an altitude of 400 km.

the lower crustal thickness indicated by the 3SMAC model. This increase was allowed following the reported work of Detrick and Watts (1979). The results in south Atlantic ocean indicate that either the crust is thicker in these plateaus or an additional magnetisation in the form of remanence is also contributing to the observed anomaly pattern. Additionally, over the west of Australia, the anomaly trend from the Broken ridge to the Naturliste plateau is completely missing in the *initial model*. This may also be due to the unmodelled remanent magnetisation in our *initial model*. More interesting is the inability of the *initial model* to explain the observed anomaly pattern, between Lord Howe rise and Norfolk plateau, west of Australia. These unexplained anomalies may be caused by the lack of subsurface geological information for these regions and partly due to imprecisely known crustal structure in these regions. However, the possibility of remanent magnetisation also cannot be ruled out as a cause. In summary, some plateau anomalies (Kerguelen ridge, Broken ridge, Crozet and Conrad rise, Agulhas plateau in Indian ocean and Alpha ridge in Arctic ocean) are well explained by induced magnetisation or remanent magnetisation parallel to the present field. Other anomalies (Walvis ridge, Maud bank, South Georgia, anomaly between Lord Howe rise and Norfolk plateau) could possibly be remanently magnetized in direction other than the present main field.

6.5 Key uncertainties

The forgoing discussion concentrated on issues, which had not been taken up in previous chapters. There are, however, some key uncertainities, which may be an important factor in modelling and interpretation of anomalies. According to Haggerty (1978) serpentinization of the upper mantle may produce magnetites. These magnetites can enhance magnetic values locally and can be an added source for anomalies. This may be important in some cratons, like West Africa. Besides, in laboratory experiments, magnetic material shows the 'Hopkinson effect'. The susceptibility of most magnetic minerals increases with temperature near the Curie-temperature. However, Nagata (1961) showed that lower-crustal materials do not show the Hopkinson effect. Nevertheless, this uncertainty in some regions may be very important. A further uncertainty is caused by the presence of magnetic field annihilators. There are susceptibility distributions across the magnetic equator, which, in the presence of a dipole dominated inducing field, produce no observable magnetic field outside of the earth (Maus and Haak, 2003). Another annihilator derived by Runcorn (1975), states that the spherical shell of homogenous magnetisation does not produce a magnetic anomaly outside in any internal inducing field. These annihilators can be important in modelling anomalies across the magnetic equator.

The discussion of the above results can be summarized as follows. There was no effort made to compute the Curie-temperature isotherm using the observed anomaly pattern nor were geothermal models included in the present modelling work. As the Curie-temperature isotherm for basin and range provinces of the world may be shallower than the Moho, it may have a partial effect on our results for some parts of the world. However, if Moho is a lower magnetic boundary as claimed by Wasilewski and Mayhew

(1992) work the effect of Curie-temperature isotherm could be minimal in most parts of the world as has been shown conclusively through our modelling work. Remanence is not significant while modelling the anomalies over the continent but may be important over the ocean. So, our assumption of keeping our models free of remanence holds reasonably well for interpreting continental anomalies. Continent-ocean boundary effect is absent from the *first iteration* map computed for degrees 1-80. This map contains even the long wavelength components of the crustal field. With the realistic values of susceptibilities for continents and oceans, the bulk vertical susceptibility of continents and oceans may be comparable. The present modelling result indicates that remanence may be important in modelling some oceanic plateaus, especially in south Atlantic ocean. However, as remanence had not been a part of our modelling and the present work emphasizes on interpreting the anomalies observed over the continents, the modelling of oceanic plateaus is not investigated further.

Chapter 7

Conclusions

7.1 Summary

The aim of this thesis was to interpret the crustal magnetic anomalies observed at satellite altitude. Obviously, the target was to associate the magnetic anomalies with the geological sources in the crust. Eventually, the efforts were extended not only to interpret these anomalies but also to infer geological information from these maps. For this, a new simple way to model the geological units and their crustal structure on a GIS platform was derived. The magnetic potential was computed at satellite altitude and the Gauss coefficients were computed using two forward modelling methods, the Nolte-Siebert method and the equivalent dipole method. Equivalent dipole method was preferred over the Nolte-Siebert method because the former method proved to be more accurate than the latter, though, the former method requires more computation time. Only final maps were prepared using the equivalent dipole method and initial computations were done using faster Nolte-Siebert method. Subsequently, *initial model* vertical field anomaly map was predicted based on the derived global vertically integrated susceptibility model. This predicted map was then compared with the corresponding observed vertical field anomaly. Interesting results churned out after the comparison for all the continents and oceanic plateaus. Exploiting the flexibility offered by the GIS based modelling method, to change the shape of a geological unit, as it is represented as a polygon on GIS platform, detailed analysis was carried out on 6 selected regions of the world. The *initial model* anomaly map disagreed with the observed magnetic anomaly map over these 6 continental regions of the world. Each of these regions had a distinct tectonic setup and hence, a different aspect of their unit was modelled to derive a new, *first iteration* model. The modelling results described in chapter 4 and chapter 5 illustrate the relationships between satellite magnetic anomalies and the surface geology. This indicates the power of the satellite magnetic method in understanding the nature and evolution of the crust. Later, the relevance and effect of continent-ocean boundary effect was discussed in chapter 6. It is concluded that this effect is negligible as the anomaly feature over the continent ocean boundary is absent even in the long wavelength dominated map of the crustal anomalies. Key issues relating to remanence and Curie-temperature isotherm which has not been a part of modelling in the present work, is also discussed.

The following conclusions are drawn on the basis of results discussed in previous chapters of this thesis:

- The geological extension below the Phanerozoic cover can be traced following the observed anomaly pattern of the region. The results for anorogenic granites of the mid-Proterozoic province of southwest USA and the deformed Kolyma block in east Siberia prove the usefulness of the modelling technique. Basement of the Phanerozoic covered Tarim basin is also confirmed following the same approach. It would be interesting to delineate more of such regions for further detailed analysis.

- In our VIS model, the composition of the lower crust was kept consistently at the same ratio with respect to the upper crust. The factor is within limits of the maximum value permissible for the composition of the lower crust following the work of Taylor and Mclennan (1985) and Clark (1999). The factor 1.2 for the lower crust below Archean units and 1.6 times below post-Archean rocks means that lower crust is 1.2 and 1.6 times more magnetic than the corresponding upper crust.

  The strong magnetic anomalies of Central Africa, however, require a more magnetic lower crust (basalts) unless one is willing to assume remanent magnetisation for this anomaly.

- The derivation of VIS model required a seismic model as one of the inputs. For most of the world, 3SMAC turned out to be best. This has been explained in detail in Chapter 4. However, the predicted anomaly over the eastern region of North America craton, especially over the Cordilleran region, did not match well with the observed anomaly pattern. In turn, the global crustal model CRUST2.1 showed a much better agreement with the observed pattern. Hence, CRUST2.1 model was preferred for modelling geological units of North American craton. Similarly, for Guyana shield regions, in South America, the seismic model of Schmitz et al. (2002) was included in place of 3SMAC model. For the rest of the world, VIS model derived using the 3SMAC seismic model showed a better agreement with observations. Thus, new seismic models do provide better results than the previous old seismic crustal models. A new seismic crustal model was also incorporated for Greenland.

- Although gaps in the seismic information for African craton was filled in by nonseismic information while deriving 3SMAC seismic model, the crustal structure is not well constrained yet. The results of our modelling in West Africa and Central Africa indicate that the crust could be still thicker than estimated by the 3SMAC model. As in these regions some part of the observed anomaly is yet unaccounted for.

- Remanence does not appear to be important in modelling continental anomalies. This result is in agreement with the recent work by Purucker et al. (2002). It is

also not possible to distinguish whether the observed anomaly pattern is really due to induced or remanent magnetisation. On the other hand, our modelling results suggest that remanence may be required to model a few oceanic plateaus especially in south Atlantic ocean and around Australia. Magnetic stripes of oceanic crust are known to be magnetised in alternately normal and reversed direction. However, these strips are thin and the alternate polarization cancels at satellite altitude. In the present work, these strips of alternate magnetisation are not considered in the modelling.

- The modelling results provide no indication of magnetisation in the upper mantle, except for West Africa, where the magnetisation may extend below the Moho discontinuity, in to the upper mantle. Generally, the magnetisation of the upper mantle could be of long wavelength and thus be masked by the main magnetic field.

- The oceanic region has a more generalized and simple crust but the lower crustal composition of the oceanic plateaus is largely inferred on the basis of seismic studies. The plateaus were represented here by a 3-layered model. The thickness of some of the plateaus in south Atlantic ocean may need to be redefined. The modelling results suggest that the thickness of the crust of the Maud rise, in Antarctica region and South Georgia, east of Falkland islands, South America is thicker by 6.0 km and 10.0 km respectively, than indicated by the 3SMAC model.

Considering the inherent uncertainties in the interpretation of magnetic anomalies, the *initial model* derived above shows a very good correspondence with the observed magnetic anomaly map. It is encouraging to note that the predicted anomaly of most of the tectonic features and their trends have correspondence to the observed anomaly pattern. Large scale anomaly pattern observed at the satellite altitude does not mean a corresponding large scale source in the crust, but often, most of the small-scale anomaly features coalesce together to form a large anomaly, indicating several small sources in the crust. Nevertheless, the results of the interpretations are useful in limiting the range of permissible geological models and in isolating regions for more intense geophysical investigations.

One of the most important conclusions of this thesis is confirmation of the anomalies observed by CHAMP satellite to be real. Each anomaly, positive or negative amplitude reflects ancient or present-day processes that have altered the magnetisation of the crust. The challenge inherent in the interpretation is to deconvolve the multiple sources of anomalies of the crust. The modelling results discussed in previous chapters have demonstrated that most of these anomalies do have a corresponding geological source and can be reproduced following a suitable modelling methodology as presented here in this thesis. Having established that the observed anomalies can be modelled and can be predicted following a simple geological model, this should provide a new basis for interpreting increasingly accurate satellite data measured by the CHAMP satellite from decreasing orbital altitudes. Another important outcome of this modelling work is that using the *first iteration* VIS model, long wavelength component of the crustal anomalies

can be predicted which is difficult to see in the observed magnetic anomaly maps as it is masked by the main magnetic field. Such long wavelength dominated map helps us to study the long wavelength features like continent-ocean boundary. However, the modelling result suggests that continent-ocean boundary is not a long wavelength feature (Fig. 6.1). Forgoing discussions of the interpretation of individual observed anomalies using the present modelling method shows the way for increasing use of satellite magnetic anomalies for the study of the crust and lithosphere.

7.2 Outlook

In future work, the modelling method should include heat flow models though at present, their inaccuracy limits their usefulness. Remanence has not been a part of our present modelling and may not be important for continents. But for modelling the oceanic anomalies, it should be included. Aeromagnetic and gravity surveys have always provided detailed information of a region. The modelling results of such surveys can be used to improve our *initial model* by improving geological and tectonic boundaries and susceptibility of the region. This may help to predict the anomalies at satellite altitude much more accurately. New seismic crustal model needs to be consistently included in our *initial model*. Inclusion of new crustal models for North America, Guyana shield in South America and Greenland led to improved predicted anomaly maps. Incorporating heat flow, improved seismic models, aeromagnetic and gravity data and further information on the lower crust should improve our *initial model* significantly and help in producing an improved initial crustal magnetic field.

With the availability of new data from decreasing measurement altitude of the CHAMP satellite, coupled with a better understanding of the various contributions to the measured field, we will see further significant improvements in the accuracy and resolution of the observed magnetic anomaly maps.

Appendix I

Magnetic Susceptibilities of Rocks and Minerals

The following table is prepared using the maximum volume susceptibility values from the standard charts compiled by Clark and Emerson (1991) and Hunt et al. (1995).

Rock types	Maximum Volume Susceptibility (SI Units)
Igneous Rocks	
Andesite	0.17
Basalt	0.18
Dolerite	0.062
Diabase	0.16
Diorite	0.13
Gabbro	0.09
Norite	0.09
Dacite	0.05
Granite	0.05
Granodiorite/Tonalite	0.062
Peridotite	0.2
Quartz porphyries/Quartz-feldspar porphyries	0.00063
Pyroxenite/Hornblendite (Alaskan Type)	0.25
Rhyolite	0.038
Dunite	0.125
Trachyte/Syenite	0.051
Monzonite	0.1
Phonolite	0.0005
Spilites	0.0013
Avg. Igneous Rock	0.27
Avg. Acidic igneous rock (pegmatites)	0.082
Avg. Basic igneous rock (komatiites, tholeiite)	0.12

Sedimentary Rocks	
Clay	0.00025

Coal			0.000025
Silt/Carbonates			0.0012
Dolomite			0.00094
Limestone			0.025
Red sediments			0.0001
Sandstone			0.0209
Shale			0.0186
Tuffs			0.0012
Conglomerate/arkose/pelites			0.0012
Arenites/Breccia			0.0012
Avg. Sedimentary rock			0.05

Metamorphic Rocks			
Amphibolite			0.00075
Gneiss			0.025
Granulite			0.03
Acid granulite			0.03
Basic granulite			0.1
Phyllite			0.0016
Quartzite			0.0044
Schist			0.003
Serpentine			0.018
Slate			0.038
Marble			0.025
Metasediments			0.024
Migmatites			0.025
Charnockite (pyroxene granulite)			0.03
BIF (anisotropic) hematite rich (~7% magnetite)			0.25
Magnetite rich (>20% magnetite)			1.8
Magnetite Skarn			1.2
Avg. Metamorphic Rock			0.073
Magnetite	~	0.1 %	0.0034
	~	0.5 %	0.018
	~	1 %	0.034
	~	5 %	0.175
	~	10 %	0.34
	~	20 %	0.72

Minerals			
Biotite			0.0029
Garnet			0.0027
Orthopyroxene			0.0018

Graphite	0.0002
Fayalite	0.0055
Olivine	0.0016
Magnetite	5.7

Appendix II

Continental crustal composition

The continental crustal composition is shown in the Table (II.A) and the Archean crustal composition in the Table (II.B) (Taylor and McLennan, 1985).

Table II.A

	Upper crust	Lower crust	Total crust
SiO_2	66.0 %	54.4 %	57.3 %
TiO_2	0.5 %	1.0 %	0.9 %
Al_2O_3	15.2 %	16.1 %	15.9 %
FeO	**4.5 %**	**10.6 %**	**9.1 %**
MgO	2.2 %	6.3 %	5.3 %
CaO	4.2 %	8.5 %	7.4 %
Na_2O	3.9 %	2.8 %	3.1 %
K_2O	3.4 %	0.34 %	1.1 %

Table II.B

	Upper crust	Total crust
SiO_2	60.1 %	57.0 %
TiO_2	0.8 %	1.0 %
Al_2O_3	15.3 %	15.2 %
FeO	**8.0 %**	**9.6 %**
MgO	4.7 %	5.9 %
CaO	6.2 %	7.3 %
Na_2O	3.3 %	3.0 %
K_2O	1.8 %	0.9 %

Appendix III

Susceptibility distribution for Cathaysian-Indian craton

The parameters used for deriving vertically integrated susceptibility model for the Cathaysian-Indian craton is shown in the following table. Tectonic map is shown in Figure (2.1) for the Cathaysian craton and in Figure (2.8) for the Indian craton.

Cathaysian craton

Geological Region	GIS (name)	Maximum Susceptibility (SI units)	Stratigraphy known to depth of (km)	Reference
Archean				
East Qinling range	Qinlg	0.047		
Wutai district	Wutai	0.034	4.0	
Yinshan district	Yinsa	0.044		
Yanshan district	Yansa	0.037		
Dabie uplift	Dabia	0.065	15.0	Goodwin (1991)
Shandong district	Shndg	0.023		
Liaoning and Jilin	Li-ji	0.023		
Tarim basin	Tarpa	0.045		
Early Proterozoic				
Wutai-Taihang district	Wutae	0.020	16.3	
Yinshan district	Yinse	0.050	6.0	Goodwin (1991)
Yanshan district	Yanse	0.034	4.65	
Tarim basin	Tarpe	0.010		
Songliao Massif	Smasf	0.045		Zhang et al. (1984)
Mid Proterozoic				
Yanshan mountains	Yansm	0.006	9.8	
Western Henan	Henan	0.051	7.0	
Eastern border	Ebrdr	0.010	4.2	
Quruktagh	Quktg	0.004	6.0	Goodwin (1991)
Western Hubei	Whubi	0.021	6.6	
Kham-Yunan	Yunan	0.019	2.5	
Jiangnan	Jiang	0.064	20.0	
Tarim basin	Tarpm	0.001		
Lower Proterozoic				
Gorge	Gorge	0.006	1.095	Goodwin (1991)
Eastern Yunan	Eyunn	0.006	1.095	

Northern Sichuan	Schun	0.006		
Southern China	Schna	0.003	4.0	
Southeast Maritime	Smepr	0.016	10.0	
Tarim mountains	Tarim	0.028	5.0	
Kunlun-Qilian-Qinling	Kunln	0.021	6.0	Goodwin (1991)
Greater Khingan	Khign	0.013		
Changan	Chage	0.029	1.0	
Nantuo	Nan12	0.023	2.285	
Luoquan	Luoqe	0.001	0.35	
Songliao Massif	Songl	0.040		Zhang et al. (1984)
Greater Balkan	Gtbal	0.050 0.085	20.0 sediment cover	Khain (1994)
West Turkmenistan	Wturk	"	15.0 sediment cover	

Indian craton

Geological Region	GIS (name)	Susceptibility (SI units)	Stratigraphy known to depth of (km)	Reference
Archean				
E-trending Gneiss-Granulite zone	Egntz	0.066		
Eastern Dharwar	Esdwr	0.055		
Closepet granite	Clspt	0.025		
Granulite domain	Grnul	0.047		
Western Dharwar	Wsdwr	0.063		
Eastern Ghat belts	Esgha	0.014		Goodwin (1991)
Singhbhum craton	Srhgh	0.045		
Rajasthan and Budelkhand blocks	Rajas	0.041		
Sri Lanka highland	Srlka	0.030		
Sri Lanka southwest	Srlkb	0.033		
Sri Lanka Vijayan complex	Srlkc	0.077		
Early Proterozoic				
Chotanagpur plateau	Chota	0.041	20.0	
Aravalli belt	Aravl	0.017		
Delhi belt	Delhs	0.014	10.0	
South Delhi belt	Sdels	0.037		Goodwin (1991)
Dongargarh	Dngar	0.039		
Sakoli	Sakol	0.067		
Sausar	Sausr	0.008		
Mid Proterozoic				
Cuddapah basin	Cudph	0.014	7.00	
Nalamalli basin	Nalla	0.027	1.20	
Kurnool basin	Kurnl	0.013	0.60	
Kaladgi basin	Kaldg	0.041	2.00	
Bhima basin	Bhima	0.002		Goodwin (1991)
Godavari basin	Godvr	0.010	7.01	
Chattisgarh basin	Chats	0.022	2.00	
Eastern Ghats belt	Esghm	0.021		

Lower Proterozoic				
Vindhyan basin	Vndhy	0.016	7.80	
Indo-Gangetic plains (Phanerozoic)	Ganga	0.005 0.045	7.00	
Deccan Traps (Phanerozoic)	Decal	0.050 0.016	4.00	Goodwin (1991)
Aravalli	Arvll	0.017 0.045		
Himalaya fold belts	Himla	0.006	20.0	
Tibetan plateau	Tibep	0.006	20.0	

Appendix IV

Susceptibility distribution for Siberian craton

The parameters used for deriving vertically integrated susceptibility model for the Siberian craton is shown in the following table. Tectonic map for the Siberian craton is shown in Figure (2.2).

Geological Region	GIS (name)	Maximum Susceptibility (SI units)	Stratigraphy known to depth of (km)	Reference
Archean				
Basement	Sbptt	0.035		
Aldan shield	Aldna	0.065 0.014 0.036	12.0	
Stanovoy fold belt	Stanv	0.020		
Siberian Trap	Sbtrp	0.035		
Anbar shield	Anbar	0.057	15.0	Goodwin (1991)
Baikal fold belt	Bakln	0.029		
Sayan fold belt	Sayan	0.027 0.035 (base)		
Yenisei fold belt	Ynsia	0.020		
Okhotsk block	Okhsk	0.031		
Kolyma block	Kolym	0.031		Goodwin (1991) (Sweeney, 1981; Howell and Wiley, 1987;Condie, 1989)
Omolon block	Omlon	0.031		
Taigonos block	Taign	0.031		
Early Proterozoic				
Baikal fold belt	Baike	0.022	13.5	
Muya group	Muyae	0.073	13.5	
Ulkan Trough	Ulkan	0.032	4.45	Goodwin (1991)
East Sayan fold belt	Sayae	0.001		
Yenisei fold belt	Yense	0.030	5.00	
Taymyr fold belt	Taymr	0.028	12.0	
Mid Proterozoic				
Patom highlands	Patom	0.033	1.80	Goodwin (1991)
Baikalian highlands	Nbaik	0.029	6.00	
South Baikal range	Sbaik	0.046	6.00	
Ulkan trough	Ulkam	0.038	5.50	
Yudoma-Maya trough	Yudma	0.011		
Uchur-Maya region	Umaya	0.006		
Olenek uplift	Olnek	0.006		
Lower Proterozoic				

Uchur-Maya	Umayl	0.031 0.001	3.00 0.40	Goodwin (1991)
Yenisei ridge	Yensl	0.018	4.50	
Patom highlands	Patol	0.031 0.013	3.00 1.70	Goodwin (1991)
Olenek uplift	Olnel	0.001	0.65	
Anbar shield	Anbal	0.001	0.65	
Tienshan	Tnshl	0.001	4.20	
Kazakhstan	Kazak	0.001	2.70	
Yudoma	Yudml	0.001	1.00	
East Sayan fold belt	Sayal	0.010	1.50	
Western Baikal	baikn	0.001	1.30	

Appendix V

Susceptibility distribution for East European craton

The parameters used for deriving vertically integrated susceptibility model for the East European craton is shown in the following table. Tectonic map for the East European craton is shown in Figure (2.3).

Geological Region	GIS (name)	Maximum Susceptibility (SI units)	Stratigraphy known to depth of (km)	Reference
Archean				
Dnieper complex	Dnepr	0.047		
Kola peninsula	Kolap	0.037		
Belomorian province	Belmr	0.058		
Kamennozero belt	Kamnz	0.045		
Koikary belt	Kokry	0.010	3.50	
Hautavaara belt	Hutvr	0.028	5.50	
Himola-Kostomuksa belt	Hm-kt	0.085	4.50	
Suomussalmi-Ilomantsi-Kuhmo-Tipasjarvi	Sukit	0.033	5.00	Goodwin, (1991) Khain, (1985)
Basement	Pltfa	0.045		
Belorussian anteclise	Pltfm	0.045	1.00 sediment cover	
Moscow syneclise	Mosms	0.045	6.00 sed. cover	
Pelchma trough	Pelch	0.045	8.00 sed. cover	
Volga-Uralian anteclise	Vl-ur	0.045	1.50 sed. cover	
North Caspian syneclise	nrcsp	0.045	30.0 sed. cover	
Glasov syneclise	Glasv	0.045	3.00 sed. cover	
Early Proterozoic				
Lapponian (Karelian)	lapon	0.032	1.40	
Sumian (Tunguda-Nadvoitsa)	Smian	0.047		
Sariolian (Sariolan)	Sarln	0.032	1.70	
Jatulian (Segozero-Onega)	Jatul	0.031		
Karelia-Kola peninsula	Kr-kl	0.062		
Suisaarian	Susrn	0.015	4.00	Goodwin, (1991)
Ladoga (Soviet Karelia)	Ladgo	0.017	4.00	
Kalevian	Kalvn	0.083		
Bergslagen (southern Sweden)	Brgle	0.032	10.0	
Southern Norrland (central Sweden)	Snrld	0.074	10.0	
Vasterbotten (central Sweden)	Vstbn	0.002		

Norrbotten (northern Sweden) East and north of Kiruna	Norbn	0.103		
Tampere (Western Finland)	Wfnld	0.038	11.5	Goodwin, (1991)
Lapland granulite belt	Lapln	0.044		
Krivoy Rog	Krvoy	0.028	8.50	
Voronezh Massif	Vornz	0.059	5.50	
Mid Proterozoic				
Rapakivi granites	Rapkv	0.056		
Bergslagen	Brgl1	0.037		
Metasediments	Msedi	0.024		
Central Norrland	Cnrld	0.050		
Norbotten	Nrbtn	0.044		
Smaland-Varmland belt	Sm-vl	0.058		
West coast (Sweden)	Wswdn	0.015		Goodwin, (1991)
Lake Vanern (Sweden)	Lvarn	0.046		
South western domain	Swdmn	0.044		
Volyn block	Volyn	0.079		
Voronezh Massif	vormz	0.067		
Bashkir Anticlinorium	Bashr	0.016	14.0	
Lower Proterozoic				
Bashkir (south urals)	Bashl	0.012	3.58	
South Urals	Sural	0.001	0.60	
Middle Urals	Mural	0.001	4.00	
Northern Norway	Nnrwy	0.008	1.20	
West of MTP (British Isles)	wsmtp	0.012	9.00	
Northern highland	Nohld	0.022		
Dalradian	Daldn	0.010	17.0	
Midland craton	Midld	0.032		
Charnwood forest-Cardington hill	Cf-ch	0.041	3.00	
Lizard peninsula	Lpnin	0.101		
SE Ireland	Irlnd	0.034		Goodwin, (1991)
Pentevrian (Armorican Massif)	Pntvr	0.011		
Brioverian	Brvrn	0.022	12.0	
Auvergne core (Central Massif)	Avgne	0.028	15.0	
Limousin-Rouergue zone	Lrgue	0.032		
Montagne Noire-Cevennes zone	Mn-cz	0.014		
Moldanubicum (Bohemian Massif)	Moldb	0.007		
Krusne Hory	Kruhy	0.037		
Ossa-Morena (Iberian Massif)	Os-mr	0.001		
Central Iberian zone	Cibrn	0.020		
West Asturian-Leonese	As-le	0.017		

Appendix VI

Susceptibility distribution for North American craton

The parameters used for deriving vertically integrated susceptibility model for the North American craton is shown in the following table. The tectonic map for the North American craton is shown in Figure (2.5).

Geological Region	GIS (name)	Maximum Susceptibility (SI units)	Stratigraphy known to depth of (km)	Reference
Archean				
Minto subprovince (Ungava craton)	Minto	0.038 0.062		
Ashuanipi complex	Ashnp	0.042		
Massive plutons (South western Superior province)	Mplut	0.051 0.062		
Meta supracrustal region	Msupr	0.019 0.062		
Abitibi belt	Abiti	0.052	11.0	
Wabigoon region	Wabgn	0.052	16.0	
Sachigo subprovince	Sachg	0.052		
Plutonic suites (central superior province)	Plutn	0.049		
Metasedimentary (English river belt)	Metas	0.044		
Point Lake (Slave craton)	Point	0.042		Goodwin, (1991)
Yellowknife	Yelow	0.046	13.0	
Hackett river	Hackt	0.021		
High Lake belt	Hghlk	0.032		
Back river	Bckrv	0.069	13.0	
Saglek Fjord (Nain province)	Saglk	0.004		
Hopedale block	Hopdl	0.072		
Committee Bay and Armit Lake (Churchill province)	Cm-ar	0.015 0.042		
Ennadai-Tulemalu blocks	En-tl	0.026		
Minnesota river valley	Mortn	0.037		
Wisconsin-Michigan gneiss	Ws-mh	0.017 0.062		
Wyoming uplift	Wyomg	0.060		
Still water complex	Still	0.070	6.00	

Newfoundland	Nwfnd (base Egren)	0.017 0.012 0.090	0.50 1.50 3.00	Colmann-Sadd, (1980)
Golcond-Roberts (bimodal volcanics, west USA)	Gl-rb	0.025		Condie, (1989)
Columbia river basalt	Colmb	0.022		
Brooks range	Chuks	0.032		Sweeney, (1981)
Alaska-Yukon	Al-yk	0.048		Goodwin, (1991)
Baffin Island	Baffn	0.062		
Mid Proterozoic province	Gra1s	0.050		Anderson, (1983)
Wopmay-extension	Wmyp5	0.028		Condie, (1989)
Basement central US	Cntms	0.029		Goodwin, (1991)
Basement Ungava	Ungav	0.037		
Basement West Sup. Prov.	Westn	0.045		
Early Proterozoic				
Lake Huron	Huron	0.017	16.0	Goodwin, (1991)
Sudbury Structure	Sudby	0.030	7.50	
Aphebian Supracrustal	Laphb	0.050	2.00	
Michigan-Wisconsin	Mh-ws	0.050	7.50	
Marquette range	Marqt	0.050		
North western segment (Animikie basin)	Nwank	0.035	6.00	
South eastern segment	Seank	0.059 0.013	11.0	
Mistassini-Otish basin	Ms-ot	0.115	6.80	
Kaniapiskau supergroup (Labrador trough)	Kanip	0.023	6.50	
Doublet-Laporte	Db-lp	0.028	5.00	
Cape Smith fold belt	Capes	0.044	5.35	
Belcher fold belt	Belch	0.032	8.00	
Sutton lake Inlier	Suton	0.069		
Fox river belt	Foxrv	0.082	5.50	
Thompson belt	Thoms	0.098		
Kapuskasing structural zone	Shawm	0.058 0.028	20.0	
Hudsonian Mobile zone	Hdcmp	0.022	3.00	
Rottenstone-la Ronge belt	Hdrot	0.036	3.00	
Cree lake zone	Crelk	0.049		
Amer lake zone	Amerl	0.043		
Wopmay zone 1	Wpmy1	0.001	0.60	
Wopmay zone 2	Wpmy2	0.010	3.00	
Wopmay zone 3	Wpmy3	0.031	9.00	
Wopmay zone 4	Wpmy4	0.048	8.00	
Kilohigok basin	Kiloh	0.006	7.00	
Athapuscow Aulacogen	Athap	0.036	5.50	
Wyoming uplift	Wyome	0.012	12.8	
Black hills	Black	0.042		
Mid Proterozoic				
Midcontinental belt	Midcn	0.034		Goodwin, (1991)
Anorogenic complexes	Anorg	0.064		
Anorthosite massifs	Anrth	0.010		

Sioux Quartzites	Sioux	0.002	0.50	
Baraboo Quartzite	Baroo	0.062	1.50	
Athabasca basin	Athas	0.003	1.50	
Baker lake	Baker	0.012	7.35	
Coppermine river	Coper	0.057	3.00	
Bathurst Inlet basin	Bathr	0.002	5.00	
Parry Bay formations	Parry	0.001	0.22	
Grenville Front Tectonic	Grenf	0.001		
Central gneiss belt	Cngne	0.001		
Central metasedimentary	Cnmet	0.030	5.00	
Central granulite belt	Cntgr	0.004		
Baie Comeau segment	Baiec	0.001		
Eastern Grenville province	Egren	0.007		Goodwin, (1991)
Fury and Hecla basin	Furyh	0.017	6.00	
Somerset Island area	Somst	0.007	3.00	
Rae Sediments	Raesd	0.011	5.00	
Troy Quartzites (Cordilleran fold belt)	Troyq	0.013	8.00	
Unkar-Chuar	Unkch	0.015	3.70	
Crystal spring	Cryst	0.010	1.50	
Cottonwood-Unita fms.	Co-un	0.007	6.00	
Belt-Purcell	Beltp	0.005	9.40	
Purcell	Purcl	0.008	11.2	
Wernecke	Wernk	0.005	13.0	
Lake Superior rift	Lksup	0.045	20.5	
Bruce river	Bruce	0.028	5.80	
Late Proterozoic				
Amundsen Embayment	Amnds	0.011	4.00	
Mackenzie mountain	Mcknz	0.005	2.00	
Snake river	Snake	0.029	1.56	
Windmere	Winde (base Purcell gr)	0.007	1.20	
Unita mountains	Unita	0.018	4.00	Goodwin, (1991)
Canadian Appalachians	Canad	0.060		
Avalon zone	Avaln (base egren)	0.015		
US Appalachian (western)	Wbgla	0.003	12.6	
US Appalachian (eastern)	Ebgla	0.028	9.00	

Appendix VII

Susceptibility distribution for South American craton

The parameters used for deriving vertically integrated susceptibility model for the South American craton is shown in the following table. The tectonic map for the South American craton is shown in Figure (2.6).

Geological Region	GIS (name)	Maximum Susceptibility (SI units)	Stratigraphy known to depth of (km)	Reference
Archean				
Pakairama	Pakar	0.018		
Imataca complex	Imtca	0.025		
Xingu (southern)	Xingu	0.037		
Serra dos Carajas	Serra	0.022		
Gois median massif	Goism	0.016		
Gois granulite belt	Goisg	0.080		
San Francisco craton	Sanfr	0.015		
Belo Horizonte	Beloh	0.029	7.00	
Rio das Velhas	Riode	0.025		
Luis Alves	Luisa	0.037		Goodwin, (1991)
Metamorphic grade rocks	Metag	0.017		
Rio Negro-Juruena belt (extension)	Riext	0.036		
Xingu belt (extension)	Xnext	0.017		
Ribera belt	Ribra	0.037		
Borborema	Borbn	0.037		
Pakaraima Nuleus	Parnl	0.036		
Greenstone belts	Grenb	0.042		
Granitoids, metamorphic rocks	Grant	0.032		
Early Proterozoic				
Maroni-Itacaiuhas	Ma-it	0.032		
Goias massif	Goise	0.001	0.30	
Quadrilatero	Quadr	0.033	9.63	Goodwin, (1991)
Contendas-Mirante	Co-mi	0.020	5.00	
Serrinha greenstone belt	Serhn	0.041	9.50	
Jacobina belt	Jacbn	0.003		

Mid Proterozoic				
Uatuma volcanics	Uatum	0.046	5.50	
Central Brazil shield	Cbrzl	0.051		
Roraima	Rormi	0.027	8.70	
Goritore	Gorit	0.002		
Rio Negro-Juruena belt	Riong	0.036		
Aguapei belt	Aguap	0.056		Goodwin, (1991)
San Ignacio belt	Sanig	0.027		
Northern Espinhaco	Noesp	0.010	7.00	
Eastern Espinhaco	Esesp	0.002	0.70	
Southern Espinhaco	Soesp	0.031	3.00	
Uruacu	Uruac	0.003	4.09	
Lower Proterozoic				
Paraguay-Araguaia fold belt (northern)	Baixo	0.019	4.00	
Southern segment	Soseg	0.020	5.50	
Brasilia fold belt	Brsil	0.002	7.85	
Sao Francisco craton	Macau	0.002	1.25	
Bambui group	Bambi	0.003	0.82	Goodwin, (1991)
Atlantic shield	Margn	0.003		
Atlantic shield (interior)	Inter	0.019		
Aracuai fold belt	Aracu	0.038		
Don-Feliciano belt	Dn-fe	0.059		
Sao Luis craton	Saolu	0.017		

Appendix VIII

Susceptibility distribution for African craton

The parameters used for deriving vertically integrated susceptibility model for the African craton is shown in the following table. African craton is divided into four units: East Africa, West Africa, Central Africa and South Africa. The tectonic map for Africa is shown in Figure (2.7). The susceptibility value for the Gabon craton, Central Africa is computed in section (2.2.1) and is marked here in greyshade.

East Africa

Geological Region	GIS (name)	Maximum Susceptibility (SI units)	Stratigraphy known to depth of (km)	Reference
Early Proterozoic				
Uweinant block	Umint	0.029		Goodwin, (1991)
Tibesti block	Tibst	0.029		
Arabian shield	Araba	0.032		
Nubian shield	Nubia	0.032		
Mid Proterozoic				
Tchad block	Tchad	0.016		Goodwin, (1991)
Lower Proterozoic				
Nubian shield	Nubil	0.043		Goodwin, (1991)
Arabian shield	Arabl	0.035		

West Africa

Geological Region	GIS (name)	Maximum Susceptibility (SI units)	Stratigraphy known to depth of (km)	Reference
Archean				
Liberian	Libra	0.057	9.50	Goodwin, (1991)
Amsaga belt	Amsga	0.033 0.065		
Ouzzal (western Hoggar)	Ouzal	0.049		
Oumelalen (central Hoggar)	Oumln	0.010		
Early Proterozoic				
Eburnean	Eburn	0.023		Goodwin, (1991)
Yetti (Reguibat shield)	Yetti	0.043		
Western Hoggar	Wshgr	0.016		

Central Hoggar	Cnhgr	0.020		Goodwin, (1991)
Benin-Nigeria shield	Be-ng	0.033		
Anti Atlas	Antas	0.024		
Mid Proterozoic				
Darfur	Drfur	0.022		Goodwin, (1991)
Central Hoggar	Cnhgm	0.010		
Lower Proterozoic				
Taudeni basin	Taupt	0.010	4.00	Goodwin, (1991)
Anti Atlas	Antal	0.013	9.00	
Western Hoggar	Wshgl	0.025	13.5	
		0.035		
Central Hoggar	Cnhgl	0.011		
Eastern Hoggar	Eshgr	0.011	1.50	
Benin-Nigeria	Bn-nl	0.040		
Togo belt	Togob	0.012	2.80	
Volta basin	Voltp	0.016	2.20	
Gourma Aulacogen	Gurmp	0.001	8.00	

Central Africa

Geological Region	GIS (name)	Maximum Susceptibility (SI units)	Stratigraphy known to depth of (km)	Reference
Archean				
Gabon craton	Gabon	0.089		Goodwin, (1991)
Chaillu block	Chail	0.079		
Kasai craton	Kasai	0.036		
Bouca block	Bouca	0.089		
Kibalian	Kibal	0.087		
Bomu block	Bomuc	0.012		
Tanzania	Tanzn	0.048		
Early Proterozoic				
Ubendian	Ubend	0.021		Goodwin, (1991)
Ruwenzori	Ruwnz	0.021		
Francevillian	Frvln	0.021		
Angolan craton	Angol	0.013		
Kunene region	Kunen	0.080	14.0	
Zambian block	Zmbia	0.054		
Usagaran	Usgrn	0.022	7.50	
Mid Proterozoic				
Kibaran	Kibup	0.007	1.70	Goodwin, (1991)
		0.015	3.00	
		0.028	5.50	
		0.027	3.00	
		0.035		
Burundian	Burdu	0.002	1.30	Goodwin, (1991)
		0.003	2.50	
		0.002	8.60	
		0.065		
Irumides	Irmdu	0.001	2.00	
		0.001	4.00	
		0.001	4.00	
		0.035		

		Lower Proterozoic		
Katangan	Katgu	0.001 0.008	5.80 1.50	
West Congo	Wcngz	0.045 0.047 0.011 0.050	3.50 4.90 4.60	
Lindian	Lindn	0.012	2.70	
Bukoban	Bkbnl	0.012 0.067 0.013	2.20 0.70	
Mozambique belt (Kenya-Tanzania)	Mzktz	0.051	3.00	
Malawi belt	Mzmlw	0.041		Goodwin, (1991)
Mozambique	Mzmzm	0.034		
Zambezi	Mzzmb	0.013		
Madagascar central	Mgcnt	0.011		
Madagascar south-central	Mgsnt	0.037		
Madagascar Malagsy	Mgmsy	0.035		
Central African belt South Cameroon	Cscmn	0.039		
North Cameroon	Cncmn	0.021		
Central African Precambrian belt	Cafpm	0.012		
Central African Proterozoic belt	Cafpt	0.039		
Oubanguides	Oubng	0.039		Pin and Poidevin, (1987), Goodwin, (1991)
Congo basin	Cnbsm	0.0001 0.001 0.008 0.020	1.30 9.00	Goodwin, (1991)

Southern Africa

Geological Region	GIS (name)	Maximum Susceptibility (SI units)	Stratigraphy known to depth of (km)	Reference
		Archean		
Swaziland	Swazl	0.029		
Barberton	Bartl	0.024 0.029 0.026 0.071	3.50 2.00 8.00 4.00	Goodwin, (1991)

Murchison	Murhn	0.044		
Pongola	Pngll	0.073 0.069	7.00 1.80	Goodwin, (1991)
Witwatersrand	Watal	0.098 0.024	2.60 0.10	

Ventersdorp	Vntrl	0.056 0.006 0.064	2.00 2.00 1.20	Goodwin, (1991)
Limpopo (northern)	Lmpon	0.062		
Limpopo (central)	Lmpoc	0.068		
Limpopo (southern)	Lmpos	0.049		
Zimbabwe	Zimbl	0.081 0.078 0.040	4.50 20.3	
Early Proterozoic				
Transvaal	Twlbl	0.036 0.092 0.034	2.00 3.50 7.00	Goodwin, (1991)
Cape Botswana	Btswl	0.044 0.077 0.001	1.50 3.50 2.00	
Bushveld	Bvelu	0.151 0.037	7.50 6.80	
Matsap	Mtsap	0.033	3.80	
Magondi	Mgndi	0.027	3.50	
Kheis	Kheis	0.053	3.00	
Mid Proterozoic				
Richersveld	Rchld	0.031		Goodwin, (1991)
Bushmanland	Bsman	0.023		
Gordania	Gdnia	0.018		
Natal Province	Natal	0.033		
Ghanzi	Ghnzi	0.041	11.0	
Lower Proterozoic				
Swakop	Swkop	0.021	10.0	Goodwin, (1991)
Otavi	Otavi	0.010	6.00	
Gariep	Garip	0.001	5.50	
Saldania	Saldn	0.002		
Nama	Namam	0.010	1.50	
Zambezi	Zambz	0.010		

Appendix IX

Susceptibility distribution for Australian craton

The parameters used for deriving vertically integrated susceptibility model for the Australian craton is shown in the following table. The tectonic map for the Australian craton is shown in Figure (2.9).

Geological Region	GIS (name)	Maximum Susceptibility (SI units)	Stratigraphy known to depth of (km)	Reference
Archean				
Pilbara craton	Pilbr	0.074	30.2	
Hamersley basin	Hmsly	0.048	7.20	
Western gneiss Terrain (Yilgarn)	Wsgne	0.044		
Narryer gneiss	Naryr	0.065		
Kalgoorlie area	Kalgr	0.035	15.0	
Murchison	Murch	0.040		
Southern cross	Socro	0.044	10.0	Goodwin, (1991)
Eastern gold fields	Egold	0.044	15.0	
Basement (Yilgarn block)	Yilgl	0.032		
Gawler block	Gawlm	0.047		
Nullarbor block	Nulbr	0.047		
Great Australian bight	Asgcr	0.001		
Mt. Isa Inlier (Extension)	In-bl	0.047		Goodwin, (1996)
Region west of Musgrave block	Wsmgl	0.048		Proposed (This work)
Early Proterozoic				
Gascoyne province	Gscyn	0.019		
Ashburton trough	Ashbn	0.043	10.0	
Nabberu basin	Nabru	0.017	6.00	
Glengarry sub-basin	Gleng	0.043	6.00	
Halls Creek Inlier	Halls	0.048	19.0	
Pine Creek Inlier	Pinec	0.023	13.0	
Murphy Inlier	Murpy	0.001		Goodwin, (1991)
Tenant Creek-Davenport Inlier	Te-da	0.022	10.0	
George Town Inlier	Gorge	0.047		
Gawler domain	Gawlr	0.100 0.047		
Willyama domain	Wilym	0.045	8.00	
Mid Proterozoic				

Mc Arthur basin	Mcarh	0.023	18.0	
Kathleen group	Katln	0.022	3.00	
Mount Isa inlier	Mtisa	0.082	13.5	
South Nicholson	Nchln	0.001	6.00	
Leichardt river	Lchrt	0.001	20.0	
Birrindudu basin	Brndu	0.021	6.00	
Kimberley basin	Kmbly	0.043	16.0	
Gawler range	Gwlrr	0.039		
Musgravian division	Musgv	0.007	3.50	Goodwin, (1991)
Western Bangemall basin	Wbang	0.005	8.00	
Northern facie	Nbang	0.007	4.50	
Eastern facie	Ebang	0.007	1.00	
Western gneiss	Wg-fr	0.044		
Eastern gneiss	Esgne	0.047		
Transition zone	Trans	0.056		
Arunta domain	Arnta	0.048		
Musgrave domain	Musgr	0.048		
Lower Proterozoic				
Adelaide Geosyncline	Adeld	0.011 0.050	15.0	
Amadeus	Amads	0.001	1.20	
Officer	Ofcer	0.022	9.22	Goodwin, (1991)
Kimberley region	Kimly	0.008	2.50	
Rocky cape & Tyenna (Tasmania)	Tyena	0.005	5.00	

Appendix X

Susceptibility distribution for Greenland

The parameters used for deriving vertically integrated susceptibility model for Greenland is shown in the following table. The tectonic map for Greenland is shown in Figure (2.4).

Geological Region	GIS (name)	Maximum Susceptibility (SI units)	Stratigraphy known to depth of (km)	Reference
Archean				
Isua-Akilia region	Isuaa	0.050		
Amîtsoq gneiss	Amtsq	0.001		
Ameralik dikes	Amrlk	0.040		
Fiskenaesset complex	Fiskn	0.075		Goodwin, (1991)
Umivik & Tingmiarmivt	Umivk	0.054		
Southern Archean block	IAAFU	0.053		
Southern Greenland block	Grenr	0.040		
Northern Greenland block	Grenu	0.040		
Early Proterozoic				
Nagssugtoqidian mobile belt	Nagss	0.030		
Rinkian mobile belt	Rinkn	0.079 0.037		
Umanak-Rinks area	Umank	0.019	9.70	Goodwin, (1991)
Upernavik-Kraulshavn area	Uprnk	0.044		
Northern border (Ketilidian belt)	Nobic	0.059	5.60	
Central granite zone	Cngrn	0.036		
Folded Migmatite	Fldic	0.029		
Mid Proterozoic				
Eriksfjord formation	Eriks	0.036	2.00	
Dike swarms	Dikes	0.054		
Central complexes	Ccmpl	0.017		
Charcot land window	Charc	0.031	2.00	Goodwin, (1991)
Central metamorphic complex	Cmetn	0.007	2.50	
Northern complexes	Ncmpl	0.030	6.30	
Lower Proterozoic				
Eleonore bay	Eleon	0.006	14.6	
Hagen Fjord group	Hfjrd	0.010	4.50	Goodwin, (1991)
Thule basin	Thule	0.018	4.50	

Appendix XI

Susceptibility distribution for Antarctic craton

The parameters used for deriving vertically integrated susceptibility model for Antarctic craton is shown in the following table. The tectonic map for Antarctica is shown in Figure (2.10).

Geological Region	GIS (name)	Maximum Susceptibility (SI units)	Stratigraphy known to depth of (km)	Reference
Archean				
Dronning Maud land	Drong	0.040		
Napier complex	Naper	0.052		
Prince Charles mountains	Chrls	0.040		Goodwin, (1991)
Vestfold hills	Vestf	0.040		
Shackelton range	Shack	0.040		
Bunger hills	Bungr	0.040		
Early Proterozoic				
Rayner complex	Rainr	0.072		
Prince Charles mountains	Chrle	0.072		
Vestfold hills	Veste	0.072		
Enderby land	Endry	0.072		Goodwin, (1991)
Western Wilkes land	Wilks	0.072		
Bunger hills	Bnger	0.072		
Dronning Maud land	Dmaud	0.072		
Mid Proterozoic				
Southern Prince Charles mountains	Chrlm	0.068		
Shackleton range	Skltn	0.024		
Coats land	Coats	0.038		Goodwin, (1991)
Windmills Island	Windm	0.066		
Marie Byrd land	Ptz1a	0.068		
Lower Proterozoic				
Denman glacier	Denmn	0.018		
Enderby land	Endrb	0.062		Goodwin, (1991)
Sør Rondane mts.	Rndan	0.062		

Appendix XII

Susceptibility distribution for Oceanic crust and plateaus

The parameters used for deriving vertically integrated susceptibility model for the Oceanic crust and plateaus are shown in the following table.

Geological Region	GIS (name)	Maximum Susceptibility (SI units)	Stratigraphy known from other sources (km)	Reference
Oceanic crust				
Young oceanic crust	Ocn-y	0.120 0.090	2.11 4.97	White et al. (1992)
Old oceanic crust	Ocn-o	0.120 0.090	2.11 5.37	
Oceanic plateaus				
Iceland	iceld	0.120 0.090		3SMAC model
Flemish cap	flmsh	0.012 0.090 0.200		
Cape Verde plateau	Verde	"		
South Georgia rise	Georg	"		
Hess rise	Hessr	"		
Buton-Seron	Bt-sr	"		
Maud bank	Maudb	"		
Walvis ridge	Walvs	"		
Crozet land	Crozt	0.120 0.090 0.200		
Conrad rise	Conrd	"		
Kerguelen ridge	Krgln	"		
Bahamas	Bahma	0.560 0.090		
Porcupine bank	Porpn	0.056 0.090	10.0 18.0	Carlson et al. (1980) Nur and Ben-Avraham (1982)
Madeira plateau	Mader	0.120 0.090 0.200	5.00 4.00 10.0	

Shatsky rise	Stksy	"	2.00 6.00 8.00	Carlson et al. (1980) Nur and Ben-Avraham (1982)
Ontong-Java plateau	On-jv	"	2.00 9.00 21.0	
Broken ridge	Brokn	0.120 0.090 0.200	5.00 7.00 6.00	
Naturliste plateau	Natul	0.056 0.065	8.00 10.0	
Lord Howe rise	Hower	"	10.0 12.0	
Norfolk plateau	Norfk	"	8.00 6.00	
Agulhas plateau	Aglhs	0.120 0.056 0.200	3.00 9.00 10.0	
Mozambique	Mzmbq	0.120 0.056 0.200	3.00 5.00 11.0	
Alpha-Mendeleev ridge	Alpha	"	4.00 6.00 4.00	Jackson and Johnson (1986)
Alpha-Canada basin	Al-cn	"	3.00 6.00 4.00	
Alpha-Markov basin	Al-ma	"	3.00 5.00 4.00	
Markov basin	Markv	"	3.00 4.00 3.00	
Canada basin	Cndbs	0.120 0.090	5.00 3.00	

References

Achache, J., Abtout, A., and LeMouel, J.L., 1987. The downward continuation of Magsat crustal anomaly field over Southeast Asia. *J. Geophys. Res.*, **92**, 11584-96.

Agarwal, P.K., Thakur, N.K., Negi, J.G., 1986. A deep structural ridge beneath central India. *Geophys. Res. Lett.*, **13**, 491-4.

Almeida, F.F.M., Hasui, Y., de Brito Neves, B.B., and Fuck, R.A., 1981. Brazilian structural provinces: an introduction. In: The Geology of Brazil, ed. Mabesoone, J.M., de Brito Neves, B.B., and Sial, A.N., *Earth Sci. Rev.*, **17**, 1-29.

Alsdorf, D., and Nelson, D., 1999. Tibetan satellite magnetic low: evidence for widespread melts in Tibetan crust. *Geology*, **27**, 943-946.

Alsdorf, D.E, 1991. Statistical processing of Magsat data for magnetic anomalies of the lithosphere. M.S. Thesis, Ohio State University.

Alsdorf, D.E., von Frese R.R.B., Arkani-Hamed, J.and Noltmier, H.C., 1994. Separation of lithospheric, external and core components of the south polar geomagnetic field at satellite altitudes. *J. Geophys. Res.*, **99**, 4655-68.

Anderson, J.L., 1983. Proterozoic anorogenic plutonism of North America. *Geol. Soc. America Mem.*, **161**, 133-154.

Antoine, L.A.G., and Moyes, A.B., 1992. The Agulhas Magsat anomaly: implications for continental break-up of Gondwana. *Tectonophysics*, **212**, 33-44.

Arkani-Hamed, J., 1988. Remanent magnetization of the oceanic upper mantle. *Geophys. Res. Lett.*, **15**, 48-51.

Arkani-Hamed, J., 1991. Thermoremanent magnetization of the oceanic lithosphere inferred from a thermal evolution model: implications for the source of marine magnetic anomalies. *Tectonophysics*, **192**, 81-96.

Arkani-Hamed, J., and Dyment, J., 1996. Magnetic potential and magnetization contrasts of earth's lithosphere. *J. Geophys. Res.*, **101**, 11401-25.

Arkani-Hamed, J., and Strangway, D.W., 1985. Lateral variations of apparent magnetic susceptibility of lithosphere deduced from Magsat data. *J. Geophys. Res.*, **90**, 2655-2664.

Arkani-Hamed, J., and Strangway, D.W., 1985b. An interpretation of magnetic signatures of aulacogens and cratons in Africa and South America. *Tectonophysics*, **113**, 257-69.

Arkani-Hamed, J., and Strangway, D.W., 1986a. Band-limited global scalar magnetic anomaly map of the earth derived from Magsat data. *J. Geophys. Res*., **91**, 8193-203.

Arkani-Hamed, J., and Strangway, D.W., 1986b. Magnetic susceptibility anomalies of lithosphere beneath eastern Europe and the Middle East. *Geophysics*, **51**, 1711-24.

Arkani-Hamed, J., and Strangway, D.W., 1986c. Effective magnetic susceptibility anomalies of the oceanic upper mantle derived from Magsat data. *Geophys. Res. Lett*., **13**, 999-1002.

Arkani-Hamed, J., Langel, R. A., and Purucker, M. E., 1994. Magnetic anomaly maps of Earth derived from POGO and Magsat data. *J. Geophys. Res*., **99**, 24075-24090.

Arkani-Hamed, J., Urquhart, W.E.S., and Strangway, D.W., 1984. Delineation of Canadian sedimentary basins from Magsat data. Earth Planet. Sci. Lett., 70, 148-56.

Arkani-Hamed, J., Zhao, S.K., Strangway, D.W., 1988. Geophysical interpretation of the Magnetic anomalies of China derived from Magsat data. Geophys. J., 95, 347-59.

Artemieva, I.M., and Mooney, W.D. 2001. Thermal thickness and evolution of Precambrian lithosphere: A global study, *J. Geophys. Res.*, **106**, 16387-16414

Baum, K., Draxler, J., Hirschmann, G., Zoth, G., Hiron, S., and Kühr, M. 1995. The KTB borehole - Germany's superdeep telescope into the Earth's crust. *Oilfield review*, **7**(1), 4-22.

Bhattacharyya, B.K., and Leu, L.K., 1977. Spectral analysis of gravity and magnetic anomalies due to rectangular prismatic bodies. *Geophysics*, **42**, 41-50.

Black, R., 1980. Precambrain of West Africa. *Episodes*, **4**, 3-8.

Blakely, R.G., 1995. *Potential Theory in Gravity and Magnetic Applications*, Cambridge University Press.

Blakely, R.J., and Griscom, A., 1988. Geologic insights from upward continuation and boundary analysis of North American magnetic and gravity maps. Abstract. *Geol. Soc. Am., Abstr.*, Programs, **20**, A325.

Bradley, L.M., and Frey, H., 1988. Constraints on the crustal nature and tectonic history of the Kerguelen plateau from comparative magnetic modelling suing Magsat data. *Tectonophysics*, **145**, 243-51.

Bridgewater, D., Keto, L., McGregor, V.R., and Meyers, J.S., 1976, Archean gneiss complex of Greenland. In: *Geology of Greenland*, ed. Escher, A., and Watt, W.S., Geol. Surv. Greenland. Copenhagen, pp 18-75.

Cahen, L., Snelling, N.J., Delhal, J., and Vail, J.R., 1984. The geochronology and evaluation of Africa. Clarendon Press, Oxford.

Cain, J. C., Wang, Z., Kluth, C., and Schmitz, D.R., 1989a. Derivation of a geomagnetic model to n = 63. *Geophys. J.*, **97**, 431-441.

Cain, J. C., Wang, Z., Schmitz, D.R., and Meyer, J., 1989b. The geomagnetic spectrum for 1980 and core-crustal separation. *Geophys. J.*, **97**, 443-447.

Carlson, R.L, Christensen, N.I., and Moore, R.P., 1980. Anomalous crustal structure in ocean basins: continental fragments and oceanic plateaus. *Earth Planet. Sci. Lett.*, **51**, 171-180.

Carmichael, R.S., and Black, R.A., 1986, Analysis and use of Magsat satellite magnetic data for interpretation of crustal structure of and character in the U.S. mid-continent. *Phys. Earth. Planet. Int.*, **44**, 333-47.

CGMW, 2000. Geological Map of the World, Commission for the Geological Map of the World (CGMW) / © UNESCO Publishing.

Chapman, D.S, and Furlong, K.P, 1992, Thermal state of the continental lower crust. In: *Continental Lower Crust*, ed. D.M. Founatin, R. Arculus, and Kay R.W., pp. 179-99, Elsevier, Amsterdam.

Chappell, B.W., White, A.J.R, and Hine, R., 1988. Granite provinces and basement terranes in the Lachlan Fold Belt, southeastern Australia. *Australian Jour. Earth Sciences*, **35**, 505-521.

Churkin, M., Jr., and Trexler, J.H., 1980. Circum-Arctic plate accretion-Isolating part of the Pacific plate to form the nucleus of the Arctic basin. *Earth. Planet. Sci. Lett.*, **48**, 356-362.

Clark, D.A., 1999. Magnetic petrology of igneous intrusions: implications for exploration and magnetic interpretation. *Exploration Geophysics*, **30**, 5-26.

Clark, D.A., and Emerson, D.W., 1991. Notes on rock magnetization characteristics in applied geophysical studies. *Exploration Geophysics*, **22**, 547-55.

Clark, S.C., Frey, H., and Thomas, H.H., 1985. Satellite magnetic anomalies over subduction zones: the Aleution arc anomaly. *Geophys. Res. Lett.*, **12**, 41-4.

Cohen, Y., 1989. Traitements et interpretations de données spatiales en géomanétisme: etude des variations laterals d'aimantation de la lithosphere terrestre, Ph.D. thesis, University of ParisVII and Institute de Physique du globe de Paris, June.

Cohen, Y., and Achache, J., 1990. New global vector anomaly maps derived from Magsat data. *J. Gephys. Res*., **95**, 10783-10800.

Colmann-Sadd, S.P., 1980. Geology of south-central Newfoundland and evolution of the eastern margin of Iapetus. *Amer. Jour. Sci*., **280**, 991-1017.

Condie, K.C., 1978. Geochemistry of Proterozoic granitic plutons from New Mexico. U.S.A., *Chem. Geol*., **21**, 131-149.

Condie, K.C., 1989, *Plate tectonics and crustal evolution*. Pergamon press, New York.

Cooper, M.R., 1990, Tectonic cycles in southern Africa. *Earth Science Reviews*, 28, 321-364.

Counil, J., Cohen, Y., and Achache, J., 1991. A global continent-ocean magnetization contrast: spherical harmonic analysis. *Earth Planet.Sci. Lett*., **103**, 354-64.

Counil, J.-L, and Achache, J., 1987. Magnetization gasp associated with tearing in the central America subduction zone. *Geophys. Res. Lett*., **14**, 1115-18.

Dahl-Jensen, T., Larsen, T. B., Woelbern, I., Bach, T., Hanka, W., Kind, R., Gregersen, S., Mosegaard, K., Voss, P., Gudmundsson, O., 2003. Depth to Moho in Greenland: receiver-function analysis suggests two Proterozoic blocks in Greenland. *Earth Planet. Sci. Lett.*, **205**, 379-393

DeSantis, A., Kerridge, D.J., and Barraclough, D.R., 1989. A spherical cap harmonic model of the crustal magnetic anomaly field in Europe observed by Magsat. In: *Geomagnetism and Paleomagnetism*, ed. F.J. Lowes, D.W. Collinson, J.H. Parry, S.K.Runcorn, D.C.Tozer, and A. Soward, pp. 1-17, Kluwer, Dordrecht.

Detrick, R.S., and Watts, A.B., 1979. An analysis of isostasy in the world's oceans, 3, Aseismic ridges. *Jour. Geophys. Res*., **84**, 3637-3653.

Dickinson, W.R., 1981, Plate tectonics and the continental margin of California. In: *The Geotectonics Development of California*, ed. W.G. Ernst, Englewood Cliffs, Prentice-Hall, New Jersey, pp 1-28.

Emmermann, R., Lauterjung, J., 1997. The German Continental Deep Drilling Program KTB: Overview and major results. *Journal of Geophysical Research*, **102**(B8), 18179-18201.

Escher, A.,and Watt, W.S., 1976, Summary of the geology of Greenland. In: *Geology of Greenland*, ed., Escher, A., and Watt, W.S., The Geological survey of Greenland, Copenhagen, pp. 10-16.

Forsyth, D.A., Asudeh, I., Green A.G., and Jackson, H.R., 1986a. Crustal structure of the Northern Alpha ridge. *Nature*, **322**, 349-352.

Forsyth, D.A., Morel a l'Huissier, P., Asudeh, I., Green, A.G., 1986b. Alpha Ridge and Iceland-products of the same plume? *Journ. Of Geodynamics*, **6**, 197-214.

Fountain, D.M., and Salisbury, M.H., 1981. Exposed crustal-sections through the continental crust: implications for crustal structure, petrology and evolution. *Earth Planet. Sci. Lett.*, **56**, 263-277.

Frey, H., 1982a. Magsat scalar anomaly distribution: The global perspective. *Geophys. Res. Lett.*, **9**, 277-80.

Frey, H., 1982b. Magsat scalar anomalies and major tectonic boundaries in Asia. *Geophys. Res. Lett.*, **9**, 299-302.

Frost, B.R., and Shive, P.N., 1986. Magnetic mineralogy of the lower continental crust. *J. Geophys. Res.*, **91**, 6513-6522.

Fujita, K., 1978, Pre-Cenozoic tectonic evolution of northeast Siberia. *J. Geol.*, **86**, 159-172.

Fullerton, L.G., Frey, H.V., Roark, J.H., Thomas, H.H., 1994. Contributions of Cretaceous Quite Zones natural remanent magneitsation to Magsat anomalies in the southwest Indian ocean. *J. Geophys. Res.*, **99**, 11923-36.

Gibbs, A.K., and Barron, C.N., 1983. The Guiana shield reviewed. *Episodes*, 1983, 7-14.

Girdler, R.W., Taylor, P.T., and Frawley, J.J., 1992. A possible impact origin for the Bangui magnetic anomaly (Central Africa). *Tectonophysics*, **212**, 45-58.

Goodwin, A.M., 1991, *Precambrian Geology*, Academic Press, London.

Goodwin, A.M., 1996, *Principles of Precambrian Geology*, Academic Press, London.

Haggerty, S. E., 1978. Mineralogical constraints on Curie isotherms in deep crustal magnetic anomalies. *Geophys. Res. Lett.*, **5**, 105-108.

Haggerty, S. E., 1979. The aeromagnetic mineralogy of igneous rocks. *Can. J. Earth Sci.*, **16**, 1281-93.

Hahn, A., Ahrendt, H., Jeyer, J., and Hufen, J. –H., 1984. A model of magnetic sources within the earth's crust compatible with the field measured by the satellite Magsat. *Geol. Jb.*, **A75**, 125-56.

Hall, D.H., 1974. Long-wavelength aeromagnetic anomalies and deep crustal magnetisation in Manitoba and Northwestern Ontario, Canada. *J. Geophys.*, **40**, 403-430.

Hamoudi, M., Achache, J., and Cohen, Y., 1995. Magsat anomaly maps at ground level. *Earth Planet. Sci. Lett.*, **133**, 533-47.

Harrison, C.G.A., 1987. The crustal field. In: *Geomagnetism*, vol. 1, ed. J. A. Jacobs, pp.513-610. Academic Press London.

Harrison, C.G.A., Carle, S.M. and Hayling, K.L., 1986. Interpretation of satellite elevation magnetic anomalies. *J. Geophys. Res.*, **91**, 3633-3650

Hastings, D.A., 1982. Preliminary correlations of Magsat anomalies with tectonic features of Africa. *Geophys. Res. Lett.*, **9**, 303-6.

Hayling, K.L., and Harrison, C.G.A., 1986. Magnetisation modeling in the north and equatorial Atlantic ocean using using Magsat data. *J. Geophys. Res.*, **91**, 12423-43.

Henriksen, N., Higgins, A.K, Kalsbeek, F., Pulvertaft, T.C.R., 2000. Greenland from Archean to Quaternary. Descriptive text to the Geological map of Greenland 1:2 500 000, *Geology of Greenland Survey Bull.*, 185. p 93.

Hinze, W.J., and Zietz, I., 1985. The composite magnetic anomaly map of the conterminous United States. In: *The Utility of Regional gravity and Magnetic Anomaly Maps*, ed. W.J. Hinze, pp. 1-24, Society of Exploration Geophysicists, Tulsa.

Hinze, W.J., von Frese, R.R.B., Longacre, M.B., Braile, L.W., Lidiak, E.G., and Keller G.R., 1982. Regional magnetic and gravity anomalies of South America. *Geophys. Res. Lett.*, **9**, 314-17.

Hinze, W.J., von Frese, R.R.B., Ravat, D.N., 1991. Mean magnetic contrasts between oceans and continents. *Tectonophysics*, **192**, 117-27.

Hoffman, P.F., 1989. Precambrian geology and tectonic history of North America. In: *The Geology of North America-an Overview*, ed., Bally, A.W.,and Palmer, A.R., Geol. Soc. Am., *The Geology of North America*, A, 447-512.

Howell, D.G., and Wiley, T.J., 1987. Crustal evolution of northern Alaska inferred from sedimentology and structural relations of the Kandik area. *Tectonics*, **6**, 619-631.

Hunt, C. P., Moskowitz, B.M. and Banerjee, S.K., 1995. Magnetic properties of Rocks and Minerals, *In : Rock Physics and Phase Relations -A handbook of Physical constants*, AGU Reference shelf 3, ed. Ahrens, T.J., pp 189-204.

Ishihara, S., 1977. The magnetite-series and ilmenite-series granitic rocks. *Mining Geology*, **27**, 293-305.

Ishihara, S., 1981. The granitoid series and minearlization. Economicmagnetite-series and ilmenite-series granitic rocks. *Economic Geology*, 75th Anniversary Volume, 458-484.

Jackson, H.R., and Johnson, G.L., 1986. Summary of Arctic Geophysics. *Joun of Geodynamics*, **6**, 245-262.

James, P.R. and Tingey, R.J., 1983. The Precambrian geological evolution of the east Antarctic metamorphic shield- a review. In: *Antarctic Earth Science*, ed., Oliver, R.L., James, P.R. Jago, J.B., Cambridge University Press, pp 5-10.

Johnson, B.D., 1985. Viscous remanent magnetisation model for the Broken ridge satellite magnetic anomaly. *J Geophys. Res.*, **90**, 2640-6.

Kearey, P., and Vine, F.J, 1990. *Global tectonics, Blackwell, London.*

Khain, V .E., 1985. *Geology of the USSR. First part. Old cratons and Paleozoic fold belts. Gebruder Born Traeger, Berlin.*

Khain, V .E., 1994. *Geology of northern Eurasia (Ex-USSR). Second part. Phanerozoic fold belts and young platforms. Gebruder Born Traeger, Berlin.*

Kim, H.R, von Frese, R.R.B., Kim, J.W., Taylor, P.T., and Neubert, T., 2002, Ørsted verifies regional magnetic anomalies of the Antarctic lithosphere. *Geophys. Res. Lett.*, **29**, 15, ORS 3, 1-3.

King, E.R., Zietz, I., and Alldredge, R., 1964. Genesis of the Arctic ocean basin. *Science*, **144**, 1551-57.

Kröner, A, Stern R.J., Dawoud, A.S, Compston, W., and Reischmann, T., 1987, The Pan-African continental margin in North eastern Africa: evidence from a geochronological study of granulites at Savaloka, Sudan. *Earth Planet Sci. Letts.*, **85**, 91-104.

LaBrecque, J.L., and Raymond, C.A., 1985. Seafloor spreading anomalies in the Magsat field of the North Atlantic. *J Geophys. Res.*, **90**, 2565-75.

Langel, R. A., and Hinze, W. J., 1998. *The magnetic field of the Earth's Lithosphere – The satellite perspective,* Cambridge University Press.

Langel, R. A., and Thorning, L, 1982. A magnetic anomaly map of Greenland, *Geophys. J. Royal Astron. Soc.*, **71**, 599-612.

Langel, R.A. and Estes, R.H., 1982. A geomagnetic field spectrum. *Geophys. Res. Lett.*, **9**, 250-3.

Langel, R.A., 1990, Study of the crust and mantle using magnetic surveys by Magsat and other satellites. *Proc. Indian Acad. Sci.*, **99**, 581-618.

Langel, R.A., Coles, R.A., and Mayhew, M.A., 1980, Comparison of magnetic anomalies of lithospheric origin measured by satellite and airborne magnetometers over western Canada. *Can. J. Earth Sci.*, **17**, 876-7.

Langel, R.A., Estes, R.H., and Mead, G. D., 1982a. Some new methods in geomagnetic field modelling applied to the 1960-1980 epoch. *J. Geomag. Geoelectr.*, **34**, 327-349.

Litherland, M., Klinck, B.A., O'Connor, E.A., and Pitfield, P.E.J., 1985. Andean-trending mobile belts in the Brazilian shield. *Nature*, **314**, 345-348.

Lowes, F.J., 1966. Mean square values on sphere of spherical harmonic vector fields. *J. Geophys. Res.*, **71**, 2179.

Mauersberger, P., 1956. Das Mittel der Energiedichte des Geomagnetischen Hauptfeldes an der Erdoberfläche und seine säkulare Änderung, *Gerlands Beitr. Geophys.*, **65**, 207-215.

Maus, S., and Haak, V., 2003. Magnetic field annihilator: invisible magnetisation at the magnetic equator. *Geophys. Jour. Int.*, (in print)

Maus, S., Gordon, D., and Fairhead, D., 1997. Curie-temperature depth estimation using a self-similar magnetization model. *Geophys. J. Int.*, **129**, 163-168.

Maus, S., Rother, M., Holme, R., Luhr, H., Olsen, N., Haak, V., 2002. First scalar magnetic anomaly map from CHAMP satellite data indicates weak lithospheric field,.*Geophys. Res. Letts.*, **29**, (14).

Mayhew, M.A., 1979. Inversion of satellite magnetic anomaly data. *J. Geophys.*, **45**, 119-28.

Mayhew, M.A., 1982a. An equivalent layer magnetisation model for the United States derived from satellite altitude magnetic anomalies. *J. Geophys. Res.*, **87**, 4837-45.

Mayhew, M.A., and Johnson, B.D., 1987. An equivalent layer magnetisation model for Australia based on Magsat data. *Earth Planet. Sci. Lett.*, **83**, 167-74.

Mayhew, M.A., Wasilewski, P.J., and Johnson, B.D., 1991. Crustal magnetisation and temperature at depth beneath the Yilgarn block, Western Australia inferred from Magsat data. *Earth Planet. Sci. Lett.*, **107**, 515-22.

Meyer, J., Hufen, J. –H, Siebert, M., and Hahn. A., 1983. Investigations of the internal geomagnetic field by means of a global model of the earth's crust. *J. Geophys.*, **52**, 71-84.

Mishra, D.C., 1984. Magnetic anomalies-India and Antarctica. *Earth Planet. Sci. Lett.*, **71**, 173-80.

Mooney, W.D., Laske, G., and Masters, T.G., 1998. CRUST 5.1: A global crustal model at 5^0 X 5^0. *J. Geophys. Res.*, **103**, 727-747.

Moorbath, S., and Taylor, P.N., 1988. Early Precambrian crustal evolution in eastern India. In: The ages of the Singhbhum granite and included remnants of the older gneiss. *Geol. Soc. India*, **31**, 82-84.

Moorbath, S., O'Nions, R.K. and Pankhurst, R.J., 1973. Early Archean age for the Isua iron-formation, West Greenland. *Nature*, **245**, 138-139.

Myers, J.S., 1984. Archean tectonics in the Fiskenaesset region of south west Greenland. In: *Precambrian tectonics Illustrated*, ed., Kröner, A., and Greiling, R., Schweizerbart'sche Verlags Buchhandlungs, Stuttgart, pp. 95-112.

Nagata, T., 1961. *Rock Magnetism. Maruzen Co. Ltd., Tokyo, pp 355.*

Naqvi, S.M., and Rogers, J.J.W., 1987. *Precambrian geology of India, Clarendon Press, New York.*

Nataf, H-C, Ricard, Y., 1996. 3SMAC: an a priori tomographic model of the upper mantle based on geophysical modeling. *Phys. Earth Planet. Int.*, **95**, 101-122.

Negi, J.G., Thakur, N.K., and Agrawal, P.K., 1986. Crustal magnetization model of the Indian subcontinent through inversion of satellite data. *Tectonophysics*, **122**, 123-33.

Nguuri, T.K., Gore, J., Webb, S.J., Wright, C., Zengeni, T.G., Gwavava, O., Snoke, J.A. and Kaapvaal Seismic Group, 2001. Crustal structure beneath southern Africa and its implications for the formation and evolution of the Kaapvaal and Zimbabwe cratons. *Geophys. Res. Lett.*, **28**, 2501-2504.

Nolte, H. J., 1985. Eine analytische Behandlung des Magnetfeldes der Erdkruste, Diploma thesis, University of Götingen.

Nolte, H. J., and Hahn, A., 1992. A model of the distribution of crustal magnetisation in central Europe compatible with the field of magnetic anomalies deduced from Magsat results. *Geophys. J. Int.*, **111**, 483-96.

Nolte, H. J., and Siebert, M., 1987. An analytical approach to the magnetic field of the Earth's crust. *Jnl. Geophys*, **61**, 69-76.

Nur, A., and Ben-Avraham, Z., 1982. Oceanic plateaus, the fragmentation of continents, and mountain building. *J. Geophys. Res.*, **87**, 3644-61.

Olsen, N., 2002. A model of the Geomagnetic Main Field and its Secular Variation for Epoch 2000. (*Geophys. J. Int.* in press)

Olsen, N., Holme, R., Hulot., G., Sabaka, T., Neubert, T., Toffner-Clausen, L., Primdhal, F., Jorgensen, J., Leger, J. –M., Barraclough, D., Bloxham, J., Cain, J., Constable, C., Golovkov, V., Jackson, A., Kotze, P., Langlais, B., Macmillan, S., Mandea, M., Merayo, J., Newitt, L., Purucker, M., Risbo, T., Stampe, M., Thomson, A., Voorhies, C., 2000. Orsted Initial Field Model. *Geophys. Res. Letts*., **27**, 3607-3610.

Pin, C., and Poidevin, J.L., 1987. U-Pb Zircon evidence for a Pan-African granulite facies metamorphism in the central African Republic. A new interpretation of the high-grade series of the northern border of the Congo craton. *Precambrian Research*, **36**, 303-312.

Purucker, M.E., Langel, R.A, Rajaram, M., and Raymond, C., 1998. Global magnetization models with a priori information. *J. Geophys. Res.,* **103**, 2563-2584.

Purucker, M.E., Langlais, B., Olsen, N., Hulot, G, and Mandea, M, 2002. The southern edge of cratonic North America: Evidence from new satellite magnetometer observations. *Geophys. Res. Lett.,* **29**, (15), ORS 1.

Radhakrishna, B.P., 1983. Archean granite greenstone terrain of the south Indian shield. In: Precambrian of South India, ed. Naqvi S.M., and Rogers, J.J.W., *Geol. Soc. India Mem.*, **4**, 1-46.

Rajaram, M., and Langel, R.A., 1992. Magnetic anomaly modelling at the Indo-Eurasian collision zone. *Tectonophysics*, **212**, 117-27.

Ravat, D., Langel, R.A., Purucker, M., Arkani-Hamed, J., and Alsdorf, D.E., 1995. Global vector and scalar Magsat magnetic anomaly maps. *J. Geophys. Res.*, **100**, B10, 20111-20136.

Ravat, D.N., 1989. Magsat Investigations over the greater African region. Ph.D. Thesis, Purdue University.

Ravat, D.N., Hinze, W.J., and Taylor, P.T., 1993. European tectonic features observed by Magsat. *Tectonophysics*, **220**, 157-73.

Ravat, D.N., Hinze, W.J., and von Frese R.R.B., 1991. Lithospheric magnetic property contrasts within the South American plate derived from damped least-squares inversion of satellite magnetic data. *Tectonophysics*, **192**, 159-68.

Reeves, C.V., and de Wit, M., 2000. Making ends meet in Gondwana: retracing the transforms of the Indian Ocean and reconnecting continental shear zones. *Terra Nova*, 12, 272-280.

Regan, R.D., and Marsh, B.D., 1982. The Bangui magnetic anomaly: its geological origin. *J. Geophys. Res.*, **87**, 1107-20.

Regan, R.D., Cain, J.C., and Davis, W.M., 1975. A global magnetic anomaly map. *J.Geophys. Res.*, **80**, 794-802.

Ridgway, J.R., and Hinze, W.J., 1986. Magsat scalar anomaly map of South America. *Geophysics*, **51**, 1472-9.

Ritzwoller, M.H., and Bentley, C.R., 1982. Magsat magnetic anomalies over Antarctica and the surrounding oceans. *Geophys. Res. Lett.*, **9**, 285-8.

Rochette, P., Jackson, M., and Aubourg, C., 1992. Rock magnetism and the interpretation of anisotropy of the magnetic susceptibility. *Rev. Geophys.*, **30**, 209-226.

Runcorn, S. K., 1975. On the interpretation of lunar magnetism. *Phys. Earth Planet Int.*, **10**, 327-335.

Rutland, R.W.R., 1981, Structural framework of the Australian Precambrian. In: *Precambrian of the Southern Hemisphere*, ed. Hunter, D.R., Elsevier, Amstredam, 1-32.

Sabaka, T. J., Olsen, N., and Langel, R. A., 2000. A comprehensive model of the near-Earth Magnetic Field: Phase 3. NASA/TM-2000-209894, National Aeronautics and Sapce Administration, Goddard Space Flight Center, Greenbelt, Maryland.

Saggerson, E.P. 1978. Metamorphic map of Africa- with explanatory text. CGMW/CCGM, UNESCO, Paris.

Salop, L.J., 1977. *Precambrian of the northern hemisphere. Elsevier, Amsterdam.*

Salop, L.J., 1983. *Geological evolution of the earth during the Precambrian. Springer-Verlag, Berlin.*

Satyabala, S.P., 1998. Subduction in the Indo-Burma region: Is it still active?, *Geophys. Res. Lett.*, **25**, 3189-3192.

Schlinger, C.M., 1985. Magnetization of the lower crust and interpretation of regional magnetic anomalies: example from Lofoten and Vesterålen, Norway. *J Geophys. Res.*, **90**, 11484-11504.

Schmitz, M., Chalbaud, D., Castillo, J., Izarra, C., 2002. The crustal structure of the Guayana Venezuela, from seismic refraction and gravity data. *Tectonophysics*, **345**, 103-118.

Schnetzler, C.C., 1985. An estimation of continental crust magnetization and susceptibility from Magsat data for the conterminous U.S.. *J. Geophys. Res.*, **90**, 2617-20.

Shatzki, N.S., and Bogdnoff, A.A., 1959, Explanatory notes on the tectonic map of the USSR and adjoining countries. *Int. Geol. Rev.* **1**, 1-49.

Shive, P. N., Blakely, R.J., Frost, B.R., Fountain, D.M., 1992. Magnetic properties of the lower continental crust. In: *Continental Lower Crust*, ed. D.M. Founatin, R. Arculus, and Kay R.W., pp. 145-77, Elsevier, Amsterdam.

Shive, P.N., 1989. Can remanent magnetisation in the deep crust contribute to long wavelength magnetic anomalies? *Geophys. Res. Lett.*, **16**, 89-92.

Shuey, R.T., Schellinger, D.K., Johnson, E.H., Tripp, A.C., and Alley, L.B., 1977. Curie-depth determination from aeromagnetic spectra. *Geophys. J. R. Astron. Soc.*, **50**, 75-101.

Singh, B.P., and Rajaram, M., 1990. Magsat studies over the Indian region. *Proc. Indian Acad. Sci. (Earth Planet. Sci.)*, **99**, 619-37.

Sweeney, J.F., 1981. Arctic seafloor structure and tectonic evolution. American Geophys. Union-Geol. Soc. Am., *Geodynam. Series*, **2**, 55-13.

Taylor, P.N. Chadwick, B., Moorbath, S. et al., 1984. Petrography chemistry and isotopic ages of peninsular gneiss Dharwar acid volcanics rocks and the Chitdurga granite with special reference to the late Archean evolution of the Karnataka craton, southern India. *Precambrian Res.*, **23**, 349-375.

Taylor, P.T., 1983. Magnetic data over the Arctic from aircraft and satellites. *Cold Regions Sci. Techn.*, **7**, 35-40.

Taylor, P.T., 1991. Investigation of plate boundaries in the eastern Indian ocean using Magsat data. *Tectonophysics*, **192**, 153-8.

Taylor, P.T., and Frawley, J.J., 1987. Magsat anomaly data over the Kursk region, USSR. *Phys. Earth Planet. Int.*, **45**, 255-65.

Taylor, P.T., and Ravat, D.N., 1995. An interpretation of the Magsat anomalies of central Europe. *J. Appl. Geophys.*, **34**, 83-91.

Taylor, S.R., and McLennan, S.M., 1985. *The Continental Crust: Its composition and Evolution.* Oxford, Blackwell Scientific Publ. 312pp.

Telford, W.M., Geldart, L.P., Sheriff, R.E., 1990. *Applied Geophysics. 2nd edn., Cambridge University Press, Cambridge.*

Thomas, H.H., 1987. A model of ocean basin crustal magnetization appropriate for satellite elevation anomalies. *J. Geophys. Res.*, **92**, 11609-13.

Tivey, M.A., 1996. Vertical magnetic structure of ocean crust determined from near-bottom magnetic field measurements. *J. Geophys. Res.*, **101**, 20275-96.

Toft, P.B., and Arkani-Hamed, J., 1992.Magnetization of the Pacific ocean lithosphere deduced from Magsat data. *J. Geophys. Res.*, **97**, 4387-406.

Toft, P.B., and Haggerty, S.E., 1988. Limiting depth of magnetization in cratonic lithosphere. *Geophys. Res. Lett.*, **15**, 530-3.

Toft, P.B., Taylor, P.T., Arkani-Hamed, J., and Haggerty, S.E., 1992. Interpretation of satellite magnetic anomalies over the West African craton. *Tectonophysics*, **212**, 21-32.

Treloar, N.A., Shive, P.N., and Fountain, D.M., 1986. Viscous remanence acquisition in deep crustal rocks (abstract). EOS, *Trans. Am. Geophys. Union*, **67**, 266.

von Frese, R.R.B., Hinze, W.J., Braile, L.W., 1981. Spherical Earth gravity and magnetic anomaly analysis by equivalent point source inversion. *Earth Planet. Sci. Lett.*, **53**, 69-83.

von Frese, R.R.B., Hinze, W.J., McGue, C.A., and Ravat, D.N., 1989. Use of satellite magnetic anomalies for tectonic lineament studies. *Mem. Geol. Soc. India*, **12**, 171-80.

von Frese, R.R.B., Kim, J.W., Tan, L., Alsdorf, D.E., Raymond, C.A., and Taylor, P.T., 1997. Satellite measured magnetic anomaly fields of the Antractic lithosphere. In: *Terra Antarctica.*

von Frese, R.R.B., Tan, L., Kim, J.W., Bentley, C.R., 1999. Antarctic crustal modelling from the spectral correlation of free-air gravity anomalies with the terrain. *J. Geophys. Res.*, **104**, 25275-25296.

Wasilewski, P.J., and Mayhew, M.A., 1982. Crustal xenoliths magnetic properties and long wavelength source requirements. *Geophys. Res. Lett.*, **9**, 329-332.

Wasilewski, P.J., and Mayhew, M.A., 1992. The Moho as a magnetic boundary revisited. *Geophys. Res. Lett.*, **19**, 2259-62.

Wasilewski, P.J., Thomas, H.H. and Mayhew, M.A., 1979. The Moho as a magnetic boundary. *Geophys. Res. Lett.*, **6**, 541-544.

Weber, J.R., 1986. The Alpha ridge: Gravity, Seismic and Magnetic evidence for a homogeneous, mafic crust. *Jour. of Geodynamics*, **6**, 117-136.

Whaler, K.A., and Langel, R.A., 1996. Minimal crustal magnetizations from satellite data. *Phys. Earth Planet Int.*, **48**, 303-319.

White, R.S., McKenzie, D., and O'Nions, R.K., 1992. Oceanic crustal thickness from seismic measurements and rare earth element inversions. *Jour. Geophys. Res.*, **97**, 19683-19715.

Woelbern, I., Dahl-Jensen, T., Bach, T., Hanka, W., Larsen, T. B., Gregersen, S., Mosegaard, K., Kind, R., Horn, F., 2001. Mantle discontinuities under Greenland: A first glimpse, Poster-Presentation, AGU fall-meeting, San Francisco

Wyborn, L.A., 1988. Petrology, geochemistry and origin of major Australian 1880-1840 Ma, felsic volcanic – plutonic suites: A model for intra-continental felsic magma generation. *Precambrian Res.*, **40-41**, 37-60.

Yanagisawa, M., and Kono, M., 1985. Ionospheric field correlations for Magsat data. *J. Geophys. Res.*, **90**, 2527-36.

Yang, Z., Cheng, Y., and Wang, H., 1986. *The geology of China*. Clarendon Press, Oxford.

Zhang, Zh. M, Liou, J.G, and Colemann, R.G., 1984. An outline of the plate tectonics of China. *Bull. Geol. Soc. Am.*, **95**, 295-312.

Acknowledgements

Curriculum Vitae

Name:	Kumar Hemant
Born:	02.04.1975, Bokaro/India
Citizenship:	Indian

School

1980-1984	St. Joseph Primary school, Patna, India
1984-1990	Don Bosco's Academy, Patna, India
1990-1992	Bhagwan Buddha Mahavidhyalaya, Patna, India

University

1993-1996	HansRaj College, University of Delhi, Delhi, India Degree: Physics (Hons.)
1996-1999	University of Roorkee, (IIT, Roorkee), Roorkee, India M.Tech. (Applied Geophysics)

Career

1999-2001	Research Fellow at National Geophysical Research Institute, Hyderabad, India Topic: Joint Inversion of DC, MT and seismic geophysical data sets.
Since Sept. 2001	GFZ / FU Berlin, Germany